東京大学　大学院新領域創成科学研究科 基盤科学研究系物質系専攻
平成２１年度　修士論文

Strain-Induced Phase Transition in VO_2 Thin Films
（VO_2 薄膜における歪み誘起相転移）

２０１０年１月２６日提出
指導教員：Mikk Lippmaa　准教授　　印

086015：菊月　達也

Contents

Chapter 1

Introduction

1.1 Introduction

Strongly-correlated materials, such as transition metal oxides, have many interesting properties, such as superconductivity,[1,2] quantum Hall effect,[3,4] colossal magnetoresistance,[5,6] and so on. That is why these materials have been at the focus of attention by many researchers. In these materials, electrons can not be described easily by simple one-electron theories such as the local-density approximation (LDA). Electrons experience strong Coulomb repulsion between each other. One of the most interesting properties in strongly-correlated oxides is the appearance of a rich variety of phase transitions. These phase transitions can be controlled by changing electron densities, but it is also possible to induce phase transitions by a variety of external excitations, such as light,[7] magnetic field,[8] electric field,[9] pressure,[10–14] etc. The focus in this thesis is on using strain to induce a metal-to-insulator transition in VO_2 thin films.

Strained materials play important roles in our lives. For example, strain gauges,[15] strained Si,[16] and flexible thin film transistor[17] are all widely used. One interesting application of strained materials is to combine magnetoelastic elements and a piezoelectric materials. An example is a macroscopic composite of a magnetostrictive TERFENOL-D ($Tb_{1-x}Dy_xFe_{2-y}$) alloy and a piezoelectric single crystals, such as $Pb(Zr_{1-x},Ti_x)O_3$.[18–21] Such macroscopic hybrid devices have shown an ability to detect even pico-Tesla level magnetic fields at room temperature. One of the aims of this study was to explore the possibility of using the phase transition in VO_2 instead of piezo material for detecting magnetoelastic changes with higher sensitivity.

1.2 Purpose of this study

In this study, a strain-induced phase transition in VO_2 thin films was studied. There are three important purposes for this study. One is to use dynamic strain to drive a structural phase transition in a VO_2 thin film. The relation between dynamic-strain-induced phase transition behavior and temperature-induced one was also discussed. Another is to explore the possibility of fabricating an epitaxial sensor using transition oxide, VO_2 instead of a linear piezoelectric materials. For measuring these effects, a high-frequency crystal bending stage and a magnet rotation stage were needed. The third purpose was to construct these experimental devices, which were used to study the properties and performance of VO_2 thin films, but will hopefully find wider use in other oxide-related studies as well.

1.3 Outline of the thesis

Chapter 1 is the general introduction.

Chapter 2 explains the basic operating principles of the instruments that were used for fabricating and characterizing oxide thin films. Chapter 3 covers all the thin film and substrate materials that were used in the experiments. Chapter 4 and Chapter 5 cover the results and discussions of results obtained by bending single crystal samples and the measurement of magnetoelastic-resistive response of a heterostructure in a rotating magnetic field, respectively. In Chapter 6, results of collaborative efforts to study a light-induced phase transition in VO_2 are outlined. These experiments rely on VO_2 thin films fabricated within this thesis work. Finally, concluding thoughts have been collected in Chapter 7.

References

[1]M. K. Wu, J. R. Ashburn, C. J. Torng, P. H. Hor, R. L. Meng, L. Gao, Z. J. Huang, Y. Q. Wang, and C. W. Chu, PRL **58**, 908 (1987).

[2]H. Hosoi, K. Igawa, K. Arii, Y. Kamihara, M. Hirano, and H. Hosono, Nature **453**, 376 (2008).

[3]A. Tsukazaki, A. Ohtomo, T. Kita, Y. Ohno, H. Ohno, and M. Kawasaki, Science **315**, 1388 (2007).

[4]Y. Kozuka, M. Kim, C. Bell, B. G. Kim, Y. Hikita, and H. Y. Hwang, Nature **462**, 487 (2009).

[5]W. E. Pickett, and D. J. Singh, PRB **53**, 1146 (1996).

[6]Y. Tokura, and Y. Tomioka, J. Magnetism and Magnetic Materials **200**, 1 (1999).

[7]M. Fiebig, K. Miyano, Y. Tomioka, and Y. Tokura, Science **280**, 1925 (1998).

[8]G. Q. Gong, C. L. Canedy, J. Z. Sun, A. Gupta, W. J. Gallagher, and G. Xiao, J. Appl. Phys. **79**, 8 (1996).

[9]K. S. Takahashi, M. Gabay, D. Jaccard, K. Shibuya, T. Ohnishi, M. Lippmaa, and J. M. Triscone, Nature **441**, 7090 (2006).

[10]Y. Muraoka, Y. Ueda, and Z. Hiroi, J. Phys. Chem. Solids **63**, 965 (2002).

[11]S. L. Bud'ko and J. Guimpel, O. Nakamura, M. B. Maple, and I. K. Schuller, PRB **46**, 1257 (1992).

[12]W. Chang, J. M. Pond, S. W. Kirchoefer, and J. A. Bellotti, APL **87**, 242904 (2005).

[13]A. Herklotz, A. D. Rata, L. Schultz, and K. Dörr, PRB **79**, 092409 (2009).

[14]M. K. Lee, T. K. Nath, C. B. Eom, M. C. Smoak, and F. Tsui, APL **77**, 3547 (2000).

[15]C. D. Butter, and G. B. Hocker, Applied Optics **17**, 2867 (1978).

[16]J. Tersoff, and F. K. Legoues, PRL **72**, 3570 (1994).

[17]H. Yabuta, M. Sano, K. Abe, T. Aiba, T. Den, H. Kumomi, K. Nomura, T. Kamiya, and H. Hosono, APL **89**, 112123 (2006).

[18]S. Dong, J. Li, and D. Viehland, APL **83**, 2265 (2003).

[19]S. Dong, J. Li, and D. Viehland, APL **85**, 2307 (2004).

[20]S. Dong, J. Zhai, F. Bai, J. Li, and D. Viehland, APL **87**, 062502 (2005).

[21]J. Zhai, Z. Xing, S. Dong, J. Li, and D. Viehland, APL **88**, 062510 (2006).

Chapter 2

Fabrication and characterization techniques for VO_2 thin films and substrates

2.1 Introduction

The VO_2 thin films used in this study were fabricated by Pulsed Laser Deposition (PLD), which is often used to evaporate high-quality oxide thin films described in Section 2.2. For comparing typical PLD-grown films with a sample that has a very different microstructure, a thin film sample grown by Excimer laser assisted metal organic deposition (ELAMOD) was also used. This thin film growth technique can be used for fabricating thin films at lower cost than traditional PLD described in Section 2.3. Various characterization techniques were used for observing structural and physical properties of the thin films, as described in Sections 2.4-2.7.

2.2 Pulsed laser deposition (PLD)

Pulsed Laser Deposition (PLD) is widely used for oxide thin film fabrication and one of the best methods for obtaining high-quality oxide thin films of many different types of materials. The main advantages are the ability to evaporate almost any material, the ability to evaporate materials that have very high melting points, and relatively easy control of film cation stoichiometry. A photo of the deposition chamber is shown in Fig. 2.1 with an explanatory diagram of all the main chamber parts shown in Fig. 2.2.

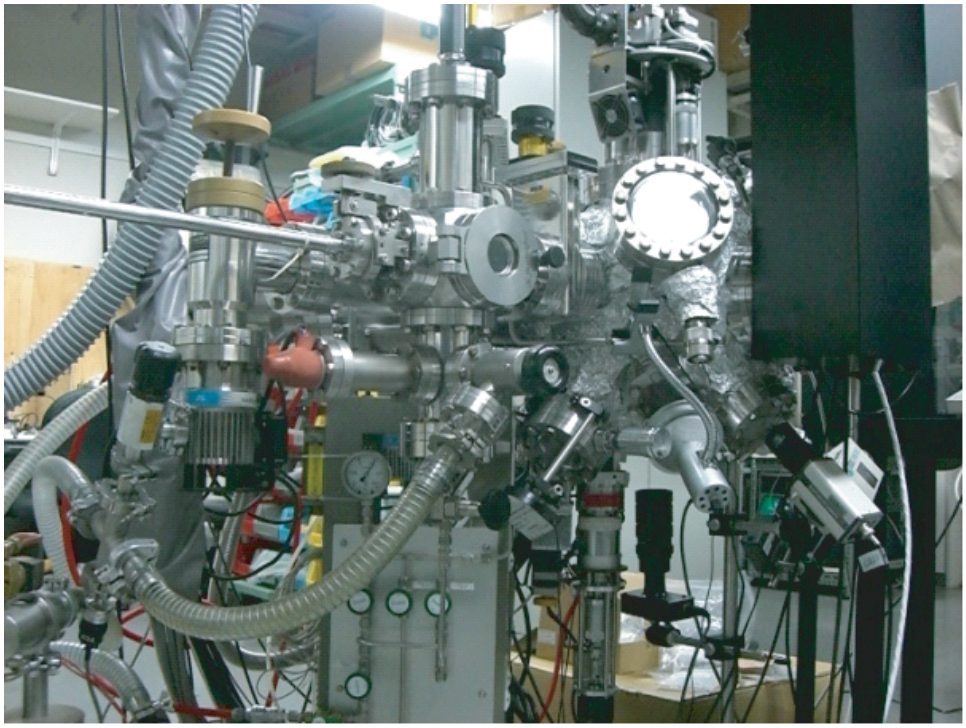

Figure 2.1: Photo of the Pulsed Laser Deposition chamber.

In the present work, a KrF excimer laser (λ = 248 nm, ThinFilmStar, Tuilaser) was used for ablating the target in the PLD chamber. The laser is shown in Fig. 2.3. The laser energy was controlled by an optical variable attenuator to obtain the desired energy density on the ablation target surface. The variable attenuator was used to compensate for laser energy changes and for gradually increasing optical losses due to a slow coating of the chamber laser entry viewport. The very high energy density at the target surface results in the ablation of a small amount of material from the target surface. The vaporized material spreads as a plasma plume in the background gas and condenses on the substrate surface, forming a thin film. The energy of the ablated atoms, molecules, ions or clusters is quite high, which is why the plume emits visible light, as shown in Fig. 2.4. This technique is particularly suitable for oxide film synthesis because generally the melting point of oxides is quite high and it is therefore difficult to evaporate oxides by other means.

This technique is not dependent on high vacuum, as required for example by molecular beam epitaxy. Due to this, oxygen can be fed into the reaction chamber through an O_2 nozzle at pressures of up to several hundred mTorr, allowing relatively straight-

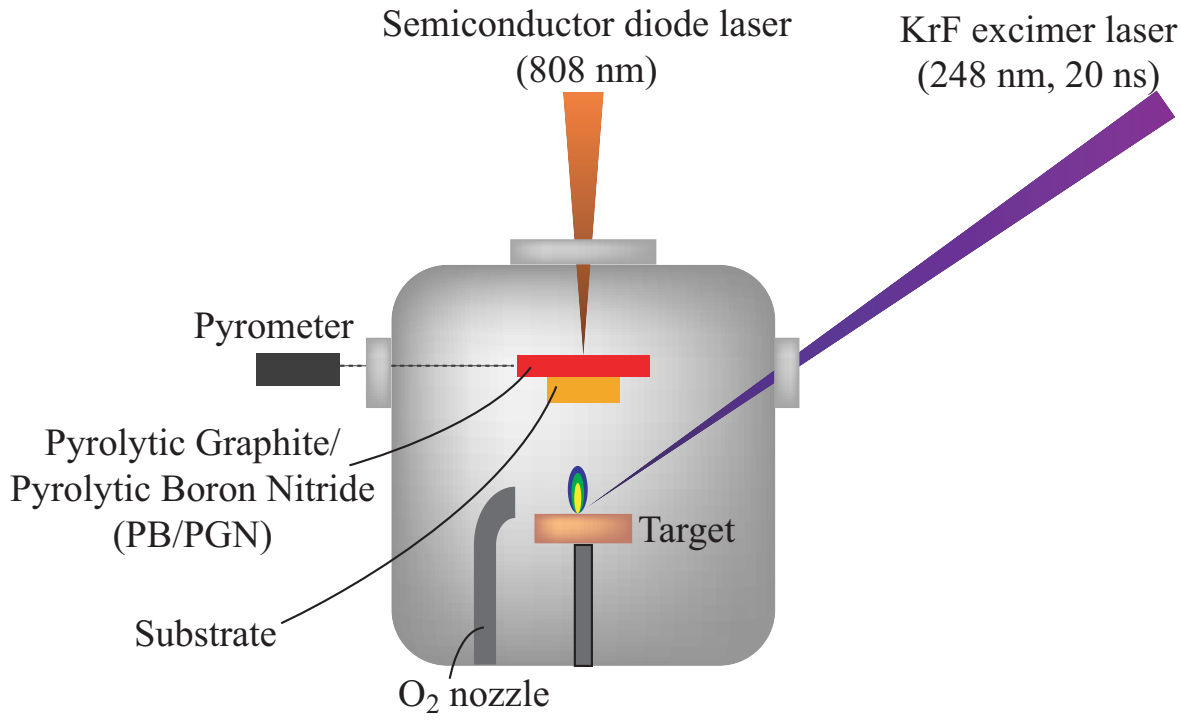

Figure 2.2: Schematic view of the PLD system. Ablated material is condenses on a substrate that is heated with a semiconductor diode laser.

Figure 2.3: KrF excimer laser (λ = 248 nm, ThinFilmStar, Tuilaser) used for ablating an oxide target in a vacuum chamber.

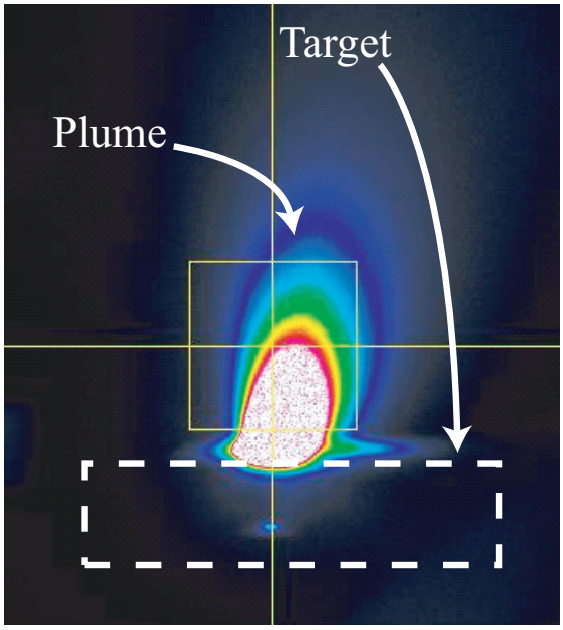

Figure 2.4: False-color image of an ablation plume. The outline of a 20 mm diameter target is also shown for scale.

forward control of oxygen content in the film.

The substrate is clamped on a high-temperature sample holder made of stainless steel, shown in Fig. 2.5. The inner part of the sample holder is thermally insulated from the outer frame by sapphire spacers. The middle part, which holds the substrate crystal and is heated by a semiconductor laser from the back, was in this case made of Pyrolytic Graphite, coated with Pyrolytic Boron Nitride (PG/PBN). The substrate was pressed against the heating block either with metal clamps or with two wires stretched across the substrate. Temperature control was done with an optical pyrometer that measures the temperature of the graphite block, while heating was done with a near-infrared semiconductor laser (λ = 808 nm, JOLD-140-CAXF-6A, Jenoptik), shown in Fig. 2.6. The advantage of using a laser for sample heating is the high maximum temperature that can be reached (maximum: 1300°C) and rapid heating/cooling, which is possible due to the low heat capacitance of the sample holder. The PG/PBN block temperature was monitored with an optical pyrometer at an emissivity setting of 0.6. This temperature is usually shown as the substrate temperature, T_{sub}.

A V_2O_3 target was used for film growth. The target was made by reducing V_2O_5 under a H_2 atmosphere at 900°C for 6 hours. After pressing a 20 mm pellet, the target

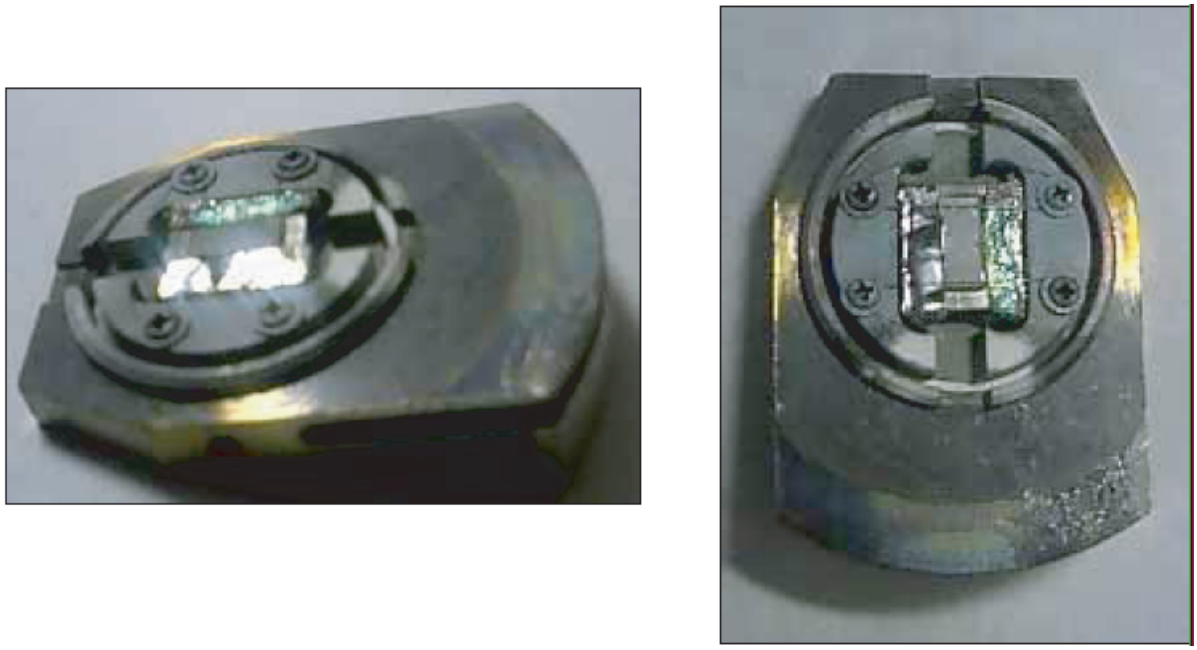

Figure 2.5: Sample holder used in film growth. Only the center part of the sample holder is actually heated.

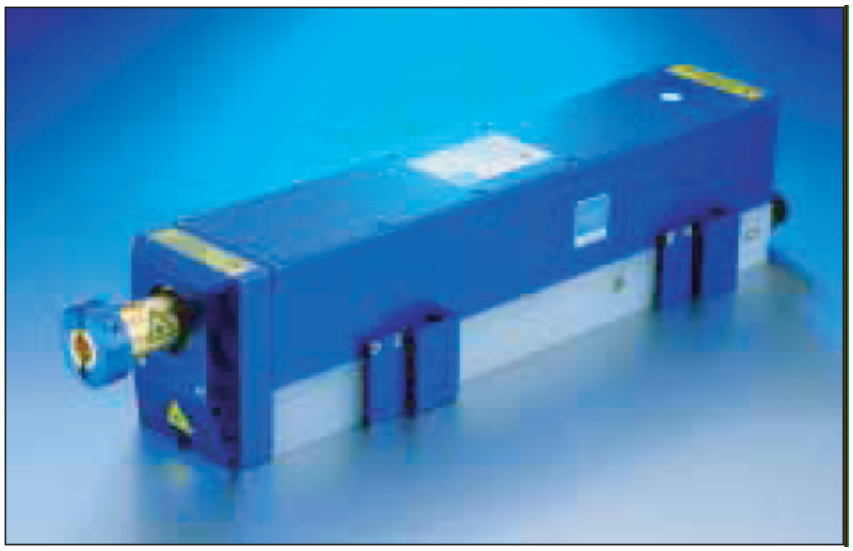

Figure 2.6: Semiconductor diode laser used for heating the substrate during film growth.

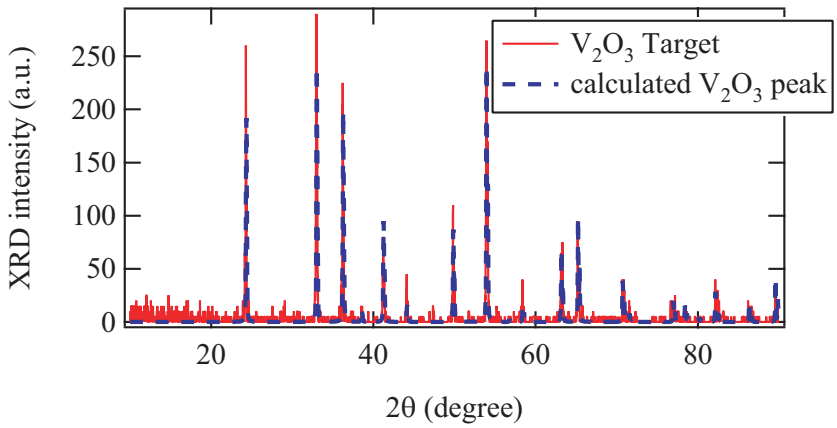

Figure 2.7: Measured and calculated XRD intensity of the V_2O_3 target.

was reduced again under the same condition for 24 hours. The XRD data of the target is shown in Fig. 2.7. As shown by the diffraction pattern, the V_2O_3 target had a nearly phase-pure composition.

2.3 Excimer laser assisted metal organic deposition (ELAMOD)

A chemical solution method, such as metal organic deposition (MOD), and coating pyrolysis are attractive processes for preparing oxide thin films in terms of simplicity and low cost. Excimer laser assisted metal organic deposition (ELAMOD) is one of related technique. The main process steps are illustrated in Fig. 2.8. The solution in which the precursor material has been dissolved, is spin-coated onto a substrate. The spin-coated film is then irradiated with a KrF excimer laser (λ = 248 nm, Lambda Physik Compex110) at room temperature in air.

The film fabricated by this technique has a much higher defects density than films grown by PLD, but the advantage of this technique is that there is no need to put the sample in a vacuum, nor to apply high temperature, and deposition on a large-area substrate is possible.

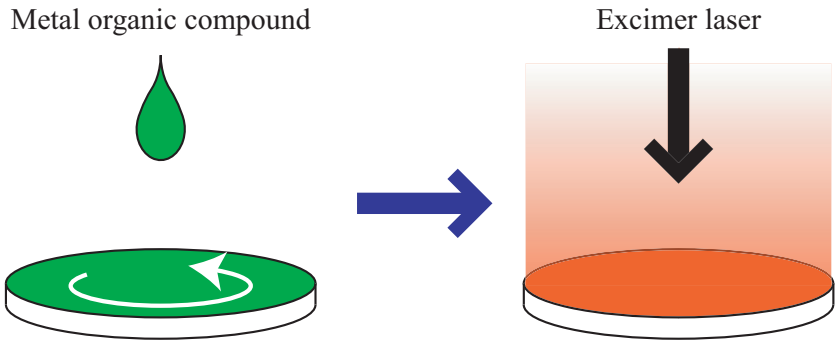

Figure 2.8: Schematic view of the excimer laser-assisted metal organic deposition (ELAMOD). Spin coated metal organic compound (left) is sintered (and oriented) with excimer laser (right).

2.4 Atomic Force Microscopy (AFM)

Atomic Force Microscopy (AFM) is a scanning probe microscopy technique that is used to measure the surface morphology of samples with a nanometer-scale accuracy. In this method, the surface height information is obtained by scanning a probe needle over the sample surface and measuring the needle position at each point on the surface. The basic building blocks of a typical AFM are shown in Fig. 2.9. In a basic AFM setup, the sharp scan needle is attached to a flexible cantilever. A piezoelectric drive is used to scan the sample so that the tip can be placed anywhere within a rectangular scan area. The height of the tip is measured optically, by detecting the deflection of the elastic cantilever as the tip moves up or down. The optical detection is done with a 4-segmented photodiode that can detect both vertical and lateral movement of the reflected light beam. The resolution of the system is determined by the diameter of the tip and it is routinely possible to achieve nm order spatial resolution (Shimadzu specification is 0.2 nm horizontal and 0.01 nm vertical resolution). Real resolution is not limited by the piezo stages, but rather by the diameter of a particular AFM tip, which is usually on the order of 10 nm. Height resolution is limited by the quality of the surface and various noise sources in the measurement. Various different measurement modes can be used in commercial AFM instruments (SPM9600, Shimadzu). In this study, Dynamic Force Mode (DFM), explained in greater detail in Section 2.4.1, and Contact Mode (CM), described in Section 2.4.2, were used for imaging surface topography and measuring conductivity maps.

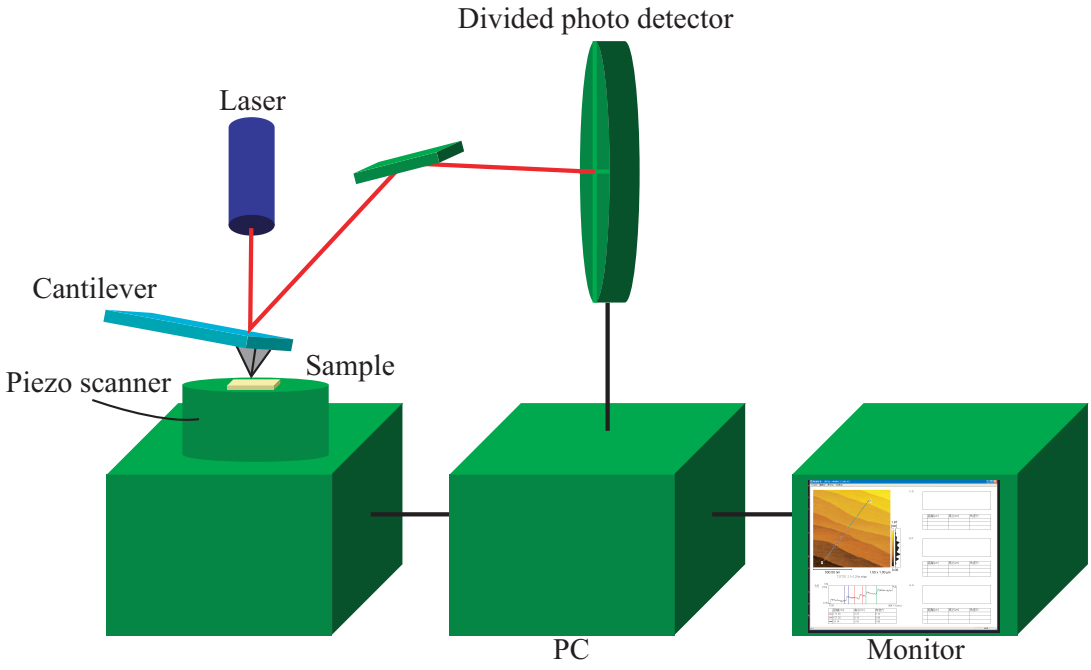

Figure 2.9: Schematic view of an Atomic Force Microscopy (AFM). The flexure of the cantilever is detected by measuring the reflected laser spot shift.

2.4.1 DFM-AFM

Most of the surface morphology measurements shown in this work were obtained by using the Dynamic Force Mode (DFM). This is on type of non-contact AFM measurement that can usually give very high-resolution images. In DFM mode, a needle is placed on a flexible cantilever as usual, but the cantilever is vibrated with an external piezo actuator under the tip. As the AFM needle approaches the sample surface, the amplitude of the cantilever vibration decreases due to the interaction between the needle and the sample. The segmented photodetector detects the vibration amplitude, and a horizontal scan is performed while keeping the amplitude loss constant. Then a topographic image can be obtained from the feedback signal.

The needle used for surface imaging was NCHR-20 (NanoWorld), with a body size of 4 (thickness) ×30 (width) ×125 (length) μm^3, and a tip radius of $\leq$ 15 nm. The back side of the tip is Al coated. The DFM tips are generally rather stiff. In this case the resonant frequency was 320 kHz at a spring constant of 42 N/m. since this mode was used in almost all imaging work, the DFM measurements are referred to as simply "AFM".

2.4.2 CM-AFM

Contact Mode (CM) AFM was used for obtaining the current map in VO_2 thin film. In this technique, an electrically conducting needle touches the sample surface while scanning, and the needle height is controlled by maintaining a constant bending angle on the tip cantilever. This gives a constant contact force ($\leq$ 1 nN) between the needle and the sample. As in DFM, the actual height signal is obtained from the height feedback channel. The AFM computer can actually acquire multiple images in parallel. In this case, a current map was obtained by applying a constant voltage of -1 V to the cantilever and measuring the current flow while scanning the needle.

The needle used in this experiment was SI-DF3-R (SII), with a body size of 4 (thickness) $\times$55 (width) $\times$450 (length) μm^3, and a tip radius of $\sim$ 30 nm. The backside was Al coated and tip-side was Rh coated. The Rh coated gives the tip conductivity, but also increases the tip radius, reducing the achievable spatial resolution. Contact mode tips use very soft cantilevers. in this case, the resonant frequency was 26 kHz at a spring constant of 1.4 N/m. This measurement mode is referred in later text as "conductive AFM".

2.5 X-ray diffraction (XRD)

X-ray diffraction (XRD) is traditionally used to study the crystal structure and crystallinity of materials. This is because the diffraction intensity becomes high if X-ray phase shift reflected from each crystal plane is $2\pi n$, where n is an integer. Thus, the XRD technique gives information about the direction, distance, and quality of the crystal planes. In an X-ray tube, X-rays are generated when a focused high-energy electron beam hits a stationary or rotating solid target. As electrons collide with atoms in the target and slow down, a continuous spectrum of X-rays are emitted. The high-energy electrons also eject inner shell electrons in atoms through the ionization process. When a free electron fills the shell, an X-ray photon with energy characteristic of the target material is emitted. A Cu X-ray source was used in this work. The Cu target emits 8 keV X-rays with a wavelength of 1.54 Å.

In order to calculate the conditions under which the intensity of scattered X-rays from a sample becomes high, it is necessary to consider the wave vector of incident X-rays, $\mathbf{K_0}$ and that of the scattered X-rays, $\mathbf{K}$, which can be written as

$$\begin{cases} \mathbf{K_0} = \dfrac{2\pi}{\lambda}\mathbf{s_0} \\ \\ \mathbf{K} = \dfrac{2\pi}{\lambda}\mathbf{s} \end{cases}, \tag{2.1}$$

where λ is X-ray wavelength, and $\mathbf{s_0}$, $\mathbf{s}$ are unit vector with the direction of the incident and scattered X-rays, respectively. The scattering vector, $\mathbf{Q}$ is

$$\mathbf{Q} = \mathbf{K} - \mathbf{K_0}. \tag{2.2}$$

A reciprocal lattice vector, $\mathbf{G}$ is defined as

$$\mathbf{G} = \frac{2\pi}{d_{hkl}}\mathbf{g}, \tag{2.3}$$

where d_{hkl} is the distance between the (hkl) plane, and $\mathbf{g}$ is a unit vector with the direction normal to the (hkl) plane. In this case, the condition when the diffraction intensity becomes high is

$$\mathbf{Q} = \mathbf{G}. \tag{2.4}$$

Eq. 2.4 is easily expressed using the angle between K_0 and K, 2θ as

$$2d_{hkl}\sin\theta = \lambda. \tag{2.5}$$

This is called Bragg's law. The diffraction patterns of the VO_2 thin films were measured with a powder XRD instrument described in Section 2.5.1, which can observe only the out-of-plane lattice parameters. Additional experiments were done with a 4-axis XRD, described in Section 2.5.2, which can obtain not only out-of-plane but also in-plane structural information.

2.5.1 Powder XRD

An image of the powder XRD (M03-X-HF22, MacScience) is shown in Fig. 2.10. A schematic diagram of the X-ray optics is in Fig. 2.11. This technique can only measure the out-of-plane lattice parameter because $\mathbf{Q}$ direction is always normal to the substrate. As in Fig. 2.11, there are four slits used for collimating the X-rays. Divergence Slit (DS) is used for controlling the X-ray divergence before hitting the sample, while the Scattering Slit (SS) is used for cutting the parasitic scattering from the sample, so the angle value should be the same as DS. The Receiving Slit (RS) is for controlling the balance of the intensity and spacial resolution. Finally, a Counter Slit (CS) is used for controlling the balance of the intensity and wavelength resolution.

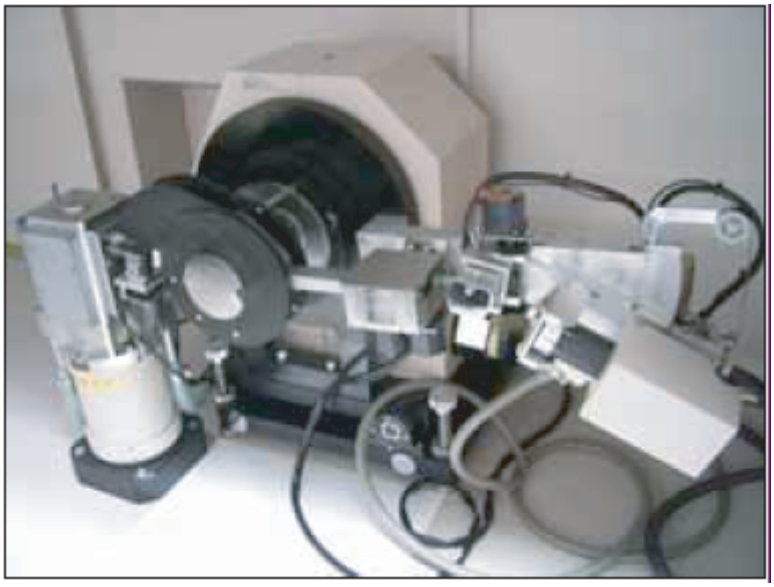

Figure 2.10: Photo of the powder X-ray Diffraction instrument.

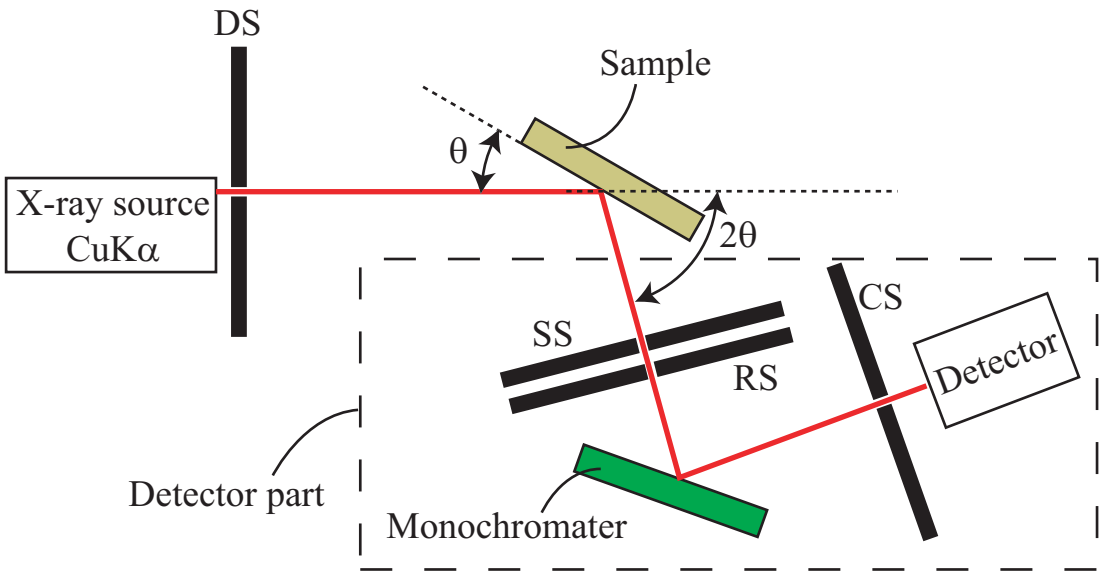

Figure 2.11: Schematic of the powder XRD X-ray optics. θ and 2θ scans are manipulated by sample rotating and detector rotation, respectively. Slit names are DS: Divergence Slit, SS: Scattering Slit, RS: Receiving Slit, and CS: Counter Slit.

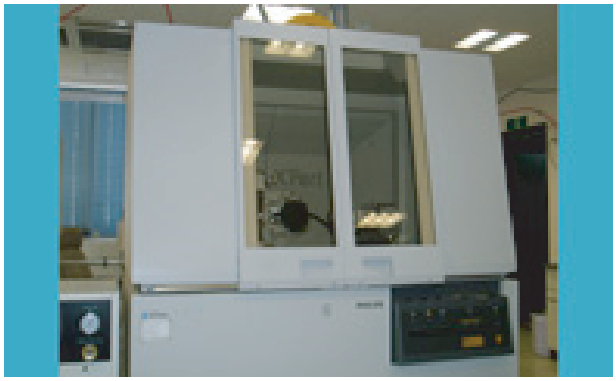

Figure 2.12: Photo of the 4-axis XRD instrument.

2.5.2 4-axis XRD

A photo of the 4-axis XRD (X'Pert MRD, Philips) instrument is shown in Fig. 2.12. The axis definitions are explained in Fig. 2.13. This technique is used for getting information about the out-of-plane and in-plane lattice parameters. This is possible, because in this instrument **Q** direction can be oriented in any direction by rotating the 4-axes (ω, 2θ, ϕ, and ψ), shown in Fig. 2.13.

The theory of the 4-axis XRD is the following.[1] There are two components in the scattering vector **Q**, which are labelled out-of-plane, Q_z, and in-plane, Q_x. By defining the incident angle as ω, shown in Fig. 2.13, these two parameters can be calculated as

$$\begin{cases} Q_x = K\{\cos\omega - \cos(2\theta - \omega)\} = 2K\sin\theta\sin(\theta - \omega) \\ Q_z = K\{\sin\omega - \sin(2\theta - \omega)\} = 2K\sin\theta\cos(\theta - \omega) \end{cases}, \tag{2.6}$$

where $K = |\mathbf{K_0}| = |\mathbf{K}|$. However, $\mathbf{K_0}$ and $\mathbf{K}$ directions have some limitations because these two vectors should not be in back-side of the substrate, i.e. it is not possible to measure in transmission geometry. This is expressed as

$$0 \leq \omega \leq 2\theta \leq \omega + \pi \leq 2\pi. \tag{2.7}$$

Eq. 2.7 determines the detectable reciprocal area as the gray area in Fig. 2.13(b).

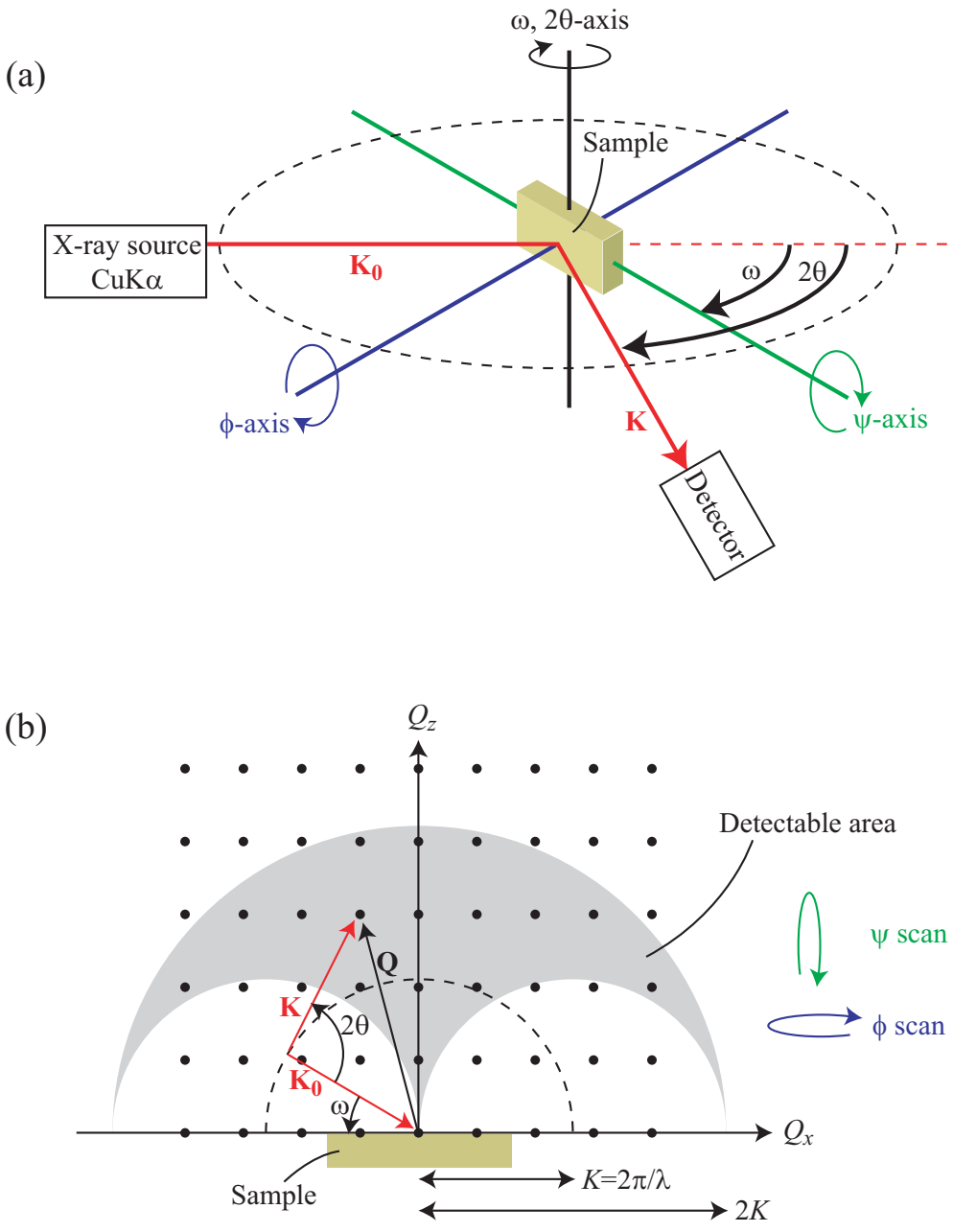

Figure 2.13: (a) Schematic view of the 4-axis XRD. The 4-axes, ω, 2θ, ϕ, and ψ are shown. (b) Combined plot of (Q_x, Q_z) plane and net of positions of Bragg peaks. Detectable area is restricted by the possible value of the vector $\mathbf{Q}=\mathbf{K}-\mathbf{K_0}$.

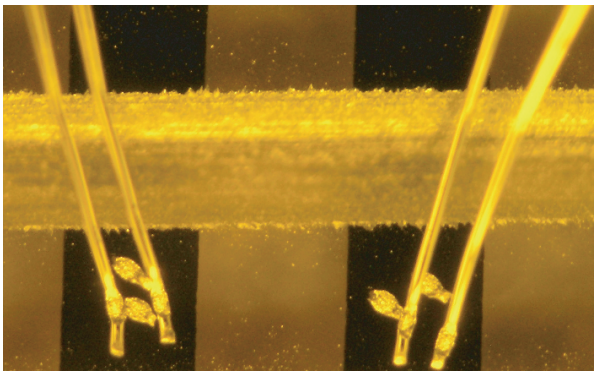

Figure 2.14: A sample showing the electrode area and wires attached by ultrasonic wire bonding.

2.6 Electrical measurement

Resistance measurements were done by attaching probe wires directly to the samples or by evaporating Al electrodes on the surface and then attaching the Al wires by ultrasonic wire bonding (7476D, WESTBOND, Inc.). The ultrasonic bonding results in deep crystal damage. When that type of damage has to be avoided, for example, when attaching wires on the surface of a film for vertical transport measurements, epoxy die bonding (7200CR, WESTBOND, Inc.) was used instead. An example of a sample surface after wires have been attached by ultrasonic wire bonding is shown in Fig. 2.14. Resistivity was measured in the van der Pauw geometry.

2.7 Physical Property Measurement System (PPMS) and Magnetic Property Measurement System (MPMS)

A Physical Property Measurement System (PPMS) (Quantum Design), shown in Fig. 2.15 is a convenient instrument for obtaining electrical transport properties of thin film samples. Both temperature and a magnetic field can be scanned during measurement. A Magnetic Property Measurement System (MPMS) (Quantum Design), shown in Fig. 2.16 was used for measuring magnetic properties of substrates. For both cases, a magnetic field is applied with a superconducting magnet with a maximum field of up to ~ 9 T. Possible temperature range is from 2 to 400 K.

The PPMS was used for measuring the resistance behavior of VO_2 thin films grown

Figure 2.15: Photo of the Physical Property Measurement System (PPMS).

Figure 2.16: Photo of the Magnetic Property Measurement System (MPMS).

on Fe_3O_4 (111) substrate under variable magnetic fields. Details of these measurements are presented in Chapter 5.4.2. The MPMS was used for obtaining the H-M data for Fe_3O_4 (111) substrates used for sensor design, as outlined in Section 5.3.

References

[1]M. Berkholz, *Thin Film Analysis by X-Ray Scattering*, WILEY-VCH Verlag Gmbh and Co. KGaA (2006).

Chapter 3

Materials background

3.1 Introduction

VO_2 thin films were grown on various substrates in this study by ablating a V_2O_3 target. VO_2 was used in this work because it has a metal-insulator transition close to room temperature, at around 340 K. Due to this, it is a potentially useful material for various sensor-type applications that should operate at room temperature. Not surprisingly, vanadates have attracted lots of research attention and the material is generally well studied. A brief overview of the properties of VO_2 are presented in the next Section. Thin films, of course, need to be grown on a substrate. In this work, most of the films were grown on insulating TiO_2 and metallic Nb:TiO_2 substrates obtained from Shinkosha Co., Ltd. Magnetic field sensor development was based on the magnetostrictive properties of magnetite and therefore Fe_3O_4 single crystals (Surface Preparation Laboratory) were used as substrates as well. Moreover, one of the collaborative researchers needed Al_2O_3 substrates. Details can be found in Section 3.3.

3.2 VO_2

At a temperature of 340 K and ambient pressure, stoichiometric VO_2 undergoes a metal-insulator transition. The transition is very sharp, as shown in Fig. 3.1.[1] The dramatic resistance change is accompanied by a structural transition from a high-temperature rutile phase to a low-temperature monoclinic phase. The crystal structures of both phases are shown in Fig. 3.2.[2] Since its discovery more than 40 years ago, this transition has been attracting considerable interest for fundamental reasons, and for possible

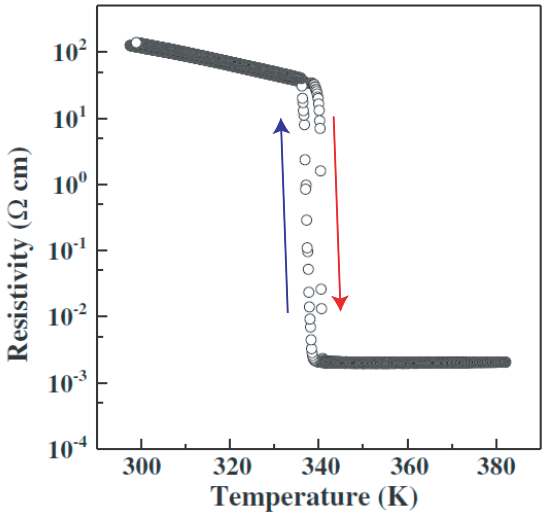

Figure 3.1: Metal-insulator transition in bulk VO_2.[1]

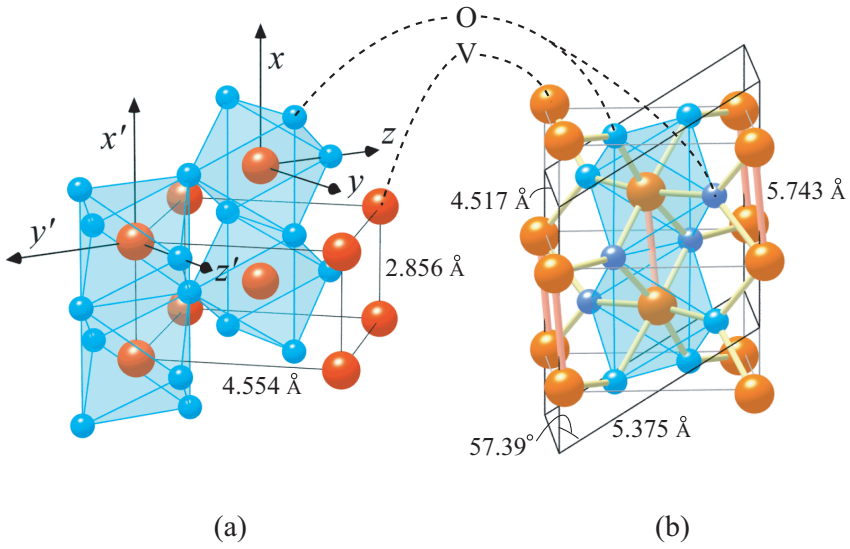

Figure 3.2: the VO_2 crystal structure in the high-temperature rutile phase (a) and low-temperature monoclinic phase (b).[2]

applications such as a infrared bolometer[3] or a hydrogen sensing device.[4] The properties of VO_2 have been studied not only in bulk[1] but also in thin films deposited on MgO,[5] Si,[6–8] SiO_2,[5,8–10] Al_2O_3,[10–15] TiO_2,[16–22] and other materials.

It is known that the VO_2 phase transition can be triggered not only by scanning

temperature,[1,17,21] but also by applying light[5,9,11,13] or an electric-field.[14] The transition temperature of VO_2, T_c, can be shifted by epitaxial strain,[21] hydrostatic stress,[23] or by doping[8] (ex. W, F, Fe etc.). Fig. 3.3 shows some of these examples.

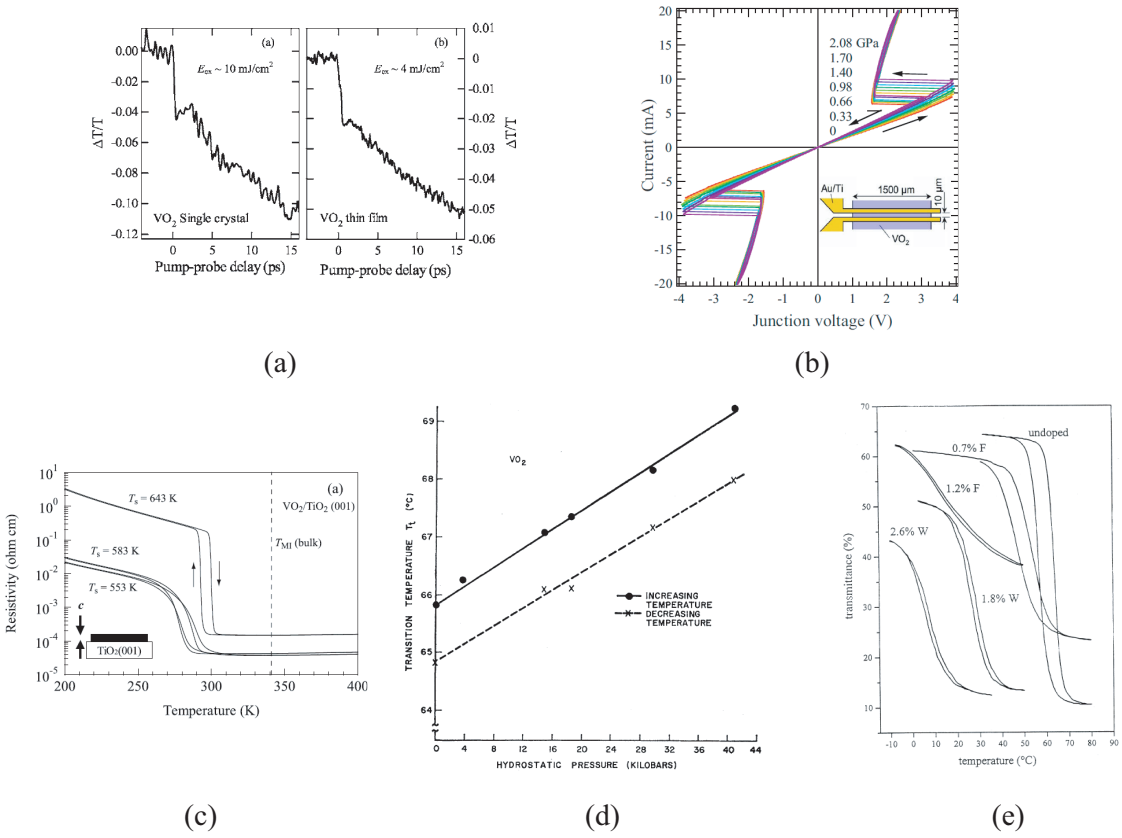

Figure 3.3: (a,b) Examples of phase transitions in VO_2, triggered by various external excitations: (a) light,[13] (b) electric field.[14] Transition temperature shift caused by epitaxial strain[21] (c), hydrostatic stress[23] (d), or doping effect[8] (e).

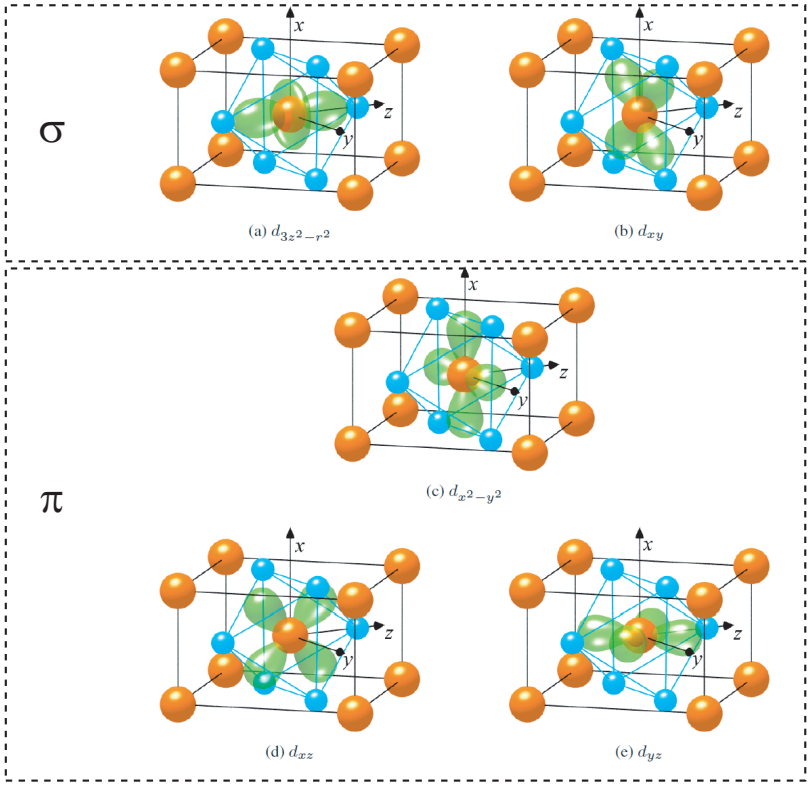

Figure 3.4: Angular parts of the 3*d* orbitals in VO_2.[2] The upper panel, $d_{3z^2-r^2}$ and d_{xy} are called σ orbitals (or e_g states) while the lower part, $d_{x^2-y^2}$, d_{xz} and d_{yz} are called π orbitals (or t_{2g} states).

3.2.1 The mechanism of the metal-insulator transition

The high-temperature rutile VO_2 phase is metallic. This can be explained from band theory as follows.[2] A Vanadium atom has five outer shell electrons, with an electronic configuration $3d^3 4s^2$. In an oxide material like VO_2, the vanadium atoms are in the V^{4+} state and thus have a single $3d^1$ electron. In VO_2 rutile structure, shown in Fig. 3.2(a), the $3d^1$ electron can occupy either a σ orbital (e_g states) or a π orbital (t_{2g} states), as shown in Fig. 3.4 because of the strong interaction with O 2*p* orbitals. For π orbitals, interaction with neighboring oxygens is weaker and thus the energy is lower than for σ orbitals. This can be seen in Fig. 3.4 as the direction of the angular part of the π orbitals does not coincide with the positions of the oxygen atoms. Due to this, the V^{4+} 3*d* electrons may be expected to occupy the π orbitals, which are responsible for three bands. From band theory, VO_2 should thus be metallic.

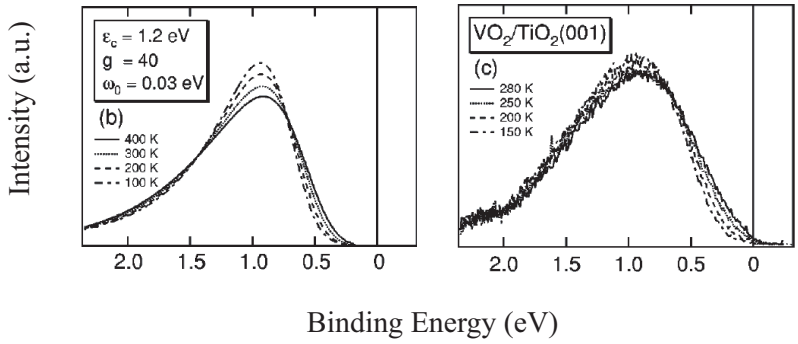

Figure 3.5: Photoemission spectra of VO_2.[20] Calculated line (left) successfully fit the experimental data (right), where the fitting model assumes that the VO_2 insulating phase is caused by both electron-electron and electron-phonon interactions.

However, in the low-temperature insulating phase, this V^{4+} $3d$ electron cannot move band to band. What causes the freezing of the electron was understood from photoemission spectroscopy experiments.[18–20] The conclusion was that the metal-insulator transition is accompanied by both a Mott transition (electron-electron interaction) and a Peierls transition (electron-phonon interaction) as shown in Fig. 3.5. As the Peierls transition occurs by VO_2 c-axis dimerization, VO_2 structure changes from tetragonal (Fig. 3.2(a)) to monoclinic (Fig. 3.2(b)). The band gap in the insulating phase is known to be 0.7 eV.

Vikhnin et al. studied the free energy (δF) of insulating and metallic VO_2 phases at different temperatures by first-principles calculations.[11,24] The calculated δF is shown in Fig. 3.6. As can be seen in the figure, the metallic and insulating phases are separated by an energy barrier. Close to T_c, the two phases can therefore coexist. A change in temperature would shift the balance in favor of one of the phases. Qualitatively similar changes in the free energy landscape can be generated by strain when the temperature is fixed at T_c. Studying this strain effect and the dynamics of the transition are the subjects of this thesis.

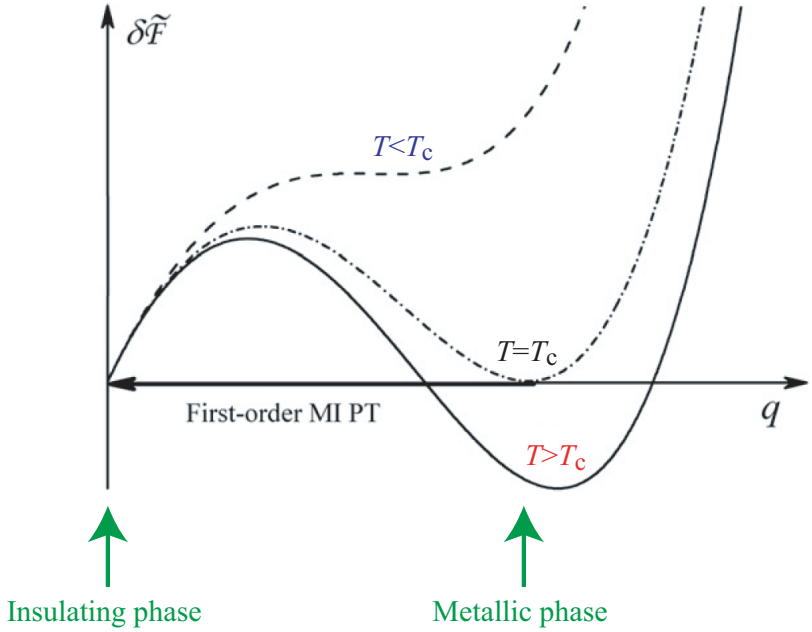

Figure 3.6: Calculated free energy (δF) dependence on the charge transfer (q) as the order parameter at different temperatures close to T_c.[11]

3.2.2 Micro-structure and characteristics

From the view point of fabricating VO_2 thin films, multiple published studies exist and provide useful starting points for choosing how to grow the films.[6,16,24]

The resistance behavior of VO_2 can be characterized by two main parameters, the Temperature Coefficient of Resistance (TCR) and the width of the resistance hysteresis on a temperature scale. Broader TCR is accompanied by a broader range of T_c in VO_2 domains or grains, while the width of the hysteresis loop is an indication of how difficult it is to transition each grain or domain from one phase to another.[16] While scanning temperature, bulk VO_2 tends to show negligible hysteresis (Fig. 3.1) while thin films usually present a 3-15°C window. There are two reasons for wide hysteresis range: difficulty of nucleating a domain and the blocking influence of grain boundaries to domain growth. Bigger grain sizes would affect both aspects of the transition and thus decrease the hysteresis width. Previous studies have concluded that the hysteresis range is linear to $\sqrt{\frac{1}{l}}$, where l is the average grain diameter. However, oxygen vacancies and structural defects are complicated issues. Thin films usually have much higher defect densities than bulk crystals and this can change the ease of nucleation and the

barrier to domain wall movement. Better crystallinity, however, causes larger TCR at T_c. An example of crystallinity dependence of resistance behavior is shown in Fig. 3.7.[6]

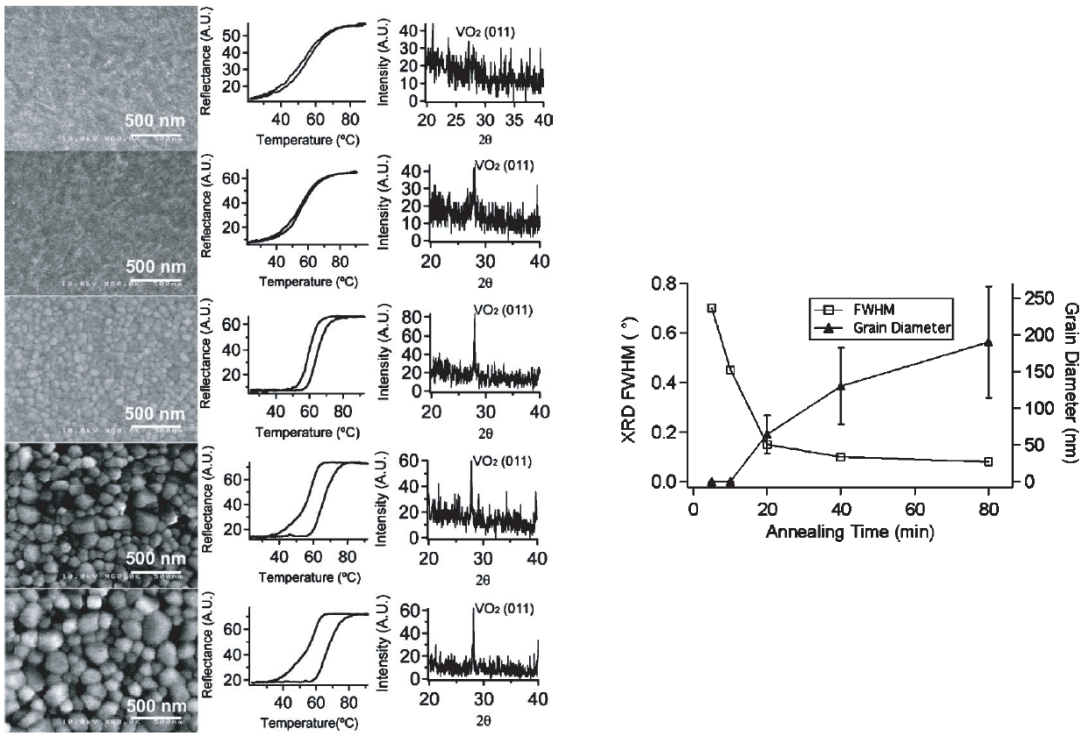

(a) (b)

Figure 3.7: Annealing time dependence of VO_2 thin films properties.[6] (a) From left to right, scanning electron micrographs of nanoparticles and thin film morphology, relative infrared reflectance, and XRD $\theta/2\theta$ scan. From top to bottom 5, 10, 20, 40, and 80 min of annealing time at 450°C. Notice the enhanced hysteresis, sharpness of the transition and grain growth. (b) Annealing time dependence of the grain size and the crystallinity of the samples in (a).

3.3 Substrates: TiO_2, Nb:TiO_2, Fe_3O_4, and Al_2O_3

TiO_2 rutile single crystal is known to be a band insulator with a gap of 3.0 eV. Ti has four outer-shell electrons and thus, Ti^{4+} has no $3d$ electrons. Resistivity is high, $> 10^7$ Ωcm at RT. One possible polymorph of TiO_2 is rutile, which has the same crystal structure as the metallic phase of VO_2, shown in Fig. 3.2. The lattice parameters of rutile phase of TiO_2 and VO_2 are shown in Table 3.1.

Table 3.1: Lattice parameters a and c, and interplanar spacing of (110), d_{110} of VO_2 and TiO_2 in the tetragonal (rutile) form. The lattice mismatch between them is presented.

Lattice parameter/material	a (Å)	c (Å)	d_{110} (Å)
VO_2	4.554	2.856	3.220
TiO_2	4.593	2.959	3.248
Lattice mismatch (%)	0.863	3.62	0.863

TiO_2 is famous for functioning as a photocatalyst, but in this case the main interest was in finding a substrate with a suitable lattice parameter for growing VO_2 thin films. Resistivity can be reduced by Nb doping. For some experiments, where a metallic substrate was needed, Nb:TiO_2 (0.5wt%) crystals were also used. In this case, the bulk resistivity was 0.27 Ωcm. From the view point of making thin films on a TiO_2 substrate, surface preparation is very important. Fortunately, TiO_2 surfaces have been very well studied and recipes for surface treatment, like annealing, can be found in the literature.[25]

Another, much less common substrate that was also used in this work, is magnetite, or Fe_3O_4. It is an inverse spinel with a lattice parameter of 8.394 Å. The structure is shown in Fig. 3.8. This material is metallic at room temperature with a resistivity of $< 10^{-2}$ Ωcm. It is also magnetic, with a high $T_c \sim 580$°C, but it was used here because it is one of the few suitable magnetostrictive substrate crystals that can also be used for VO_2 thin films growth. Lattice matching between the Fe_3O_4 (111) surface and some representative lattices of tetragonal TiO_2 and monoclinic VO_2 are shown in Fig. 3.9. Lattice mismatches are shown in Table 3.2.

Saturated longitudinal magnetostriction values of magnetite are $\lambda_{100} = -16.7$, $\lambda_{110} = 65.4$, and $\lambda_{111} = 90.6$.[27] Magnetization behavior while scanning the magnetic field is not particularly sensitive to temperature[28] or field direction[29] under T_c and there is negligible hysteresis. The magnetostriction value is known to be linear to the field up

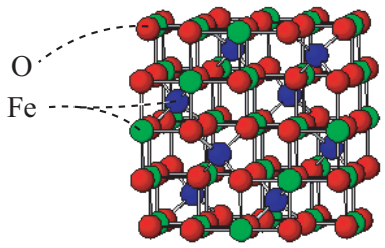

Figure 3.8: Magnetite unit cell.[26] The crystal structure is an inverse spinel.

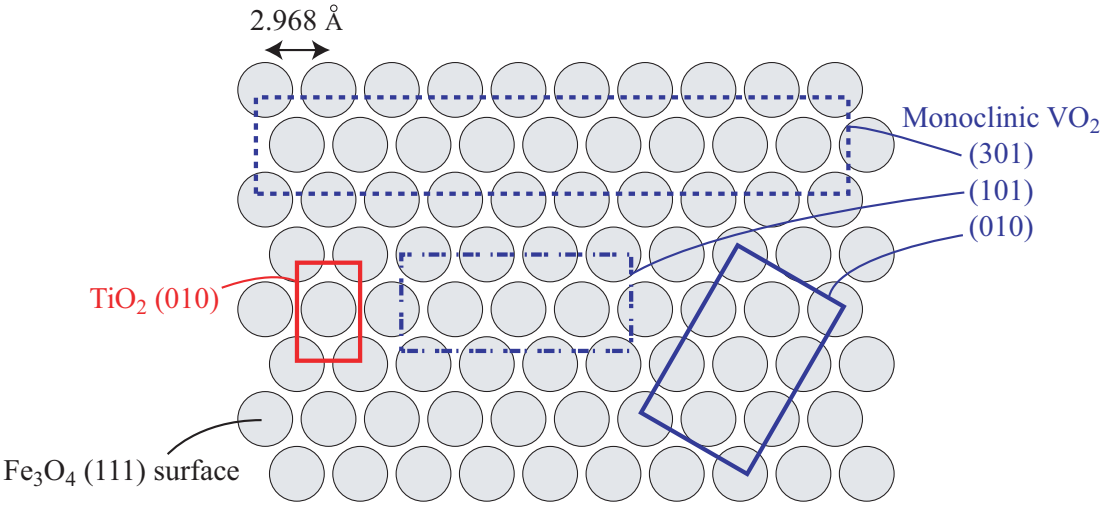

Figure 3.9: Lattice matching between Fe_3O_4 (111) surface and some representative lattices of tetragonal TiO_2 and monoclinic VO_2. Oxygen atoms are shown in gray. Red and blue rectangles show the unit cells of TiO_2 and monoclinic VO_2, respectively.

Table 3.2: Lattice mismatch between the Fe_3O_4 (111) surface and some representative lattices of tetragonal TiO_2 and monoclinic VO_2.

Lattice	Mismatches between Fe_3O_4 (111) surface
Tetragonal TiO_2 (010)	10.6 % × 0.30 %
Monoclinic VO_2 (301)	13.8 % × 3.8 %
Monoclinic VO_2 (101)	13.8 % × 10.8 %
Monoclinic VO_2 (010)	10.5 % × 1.7 %

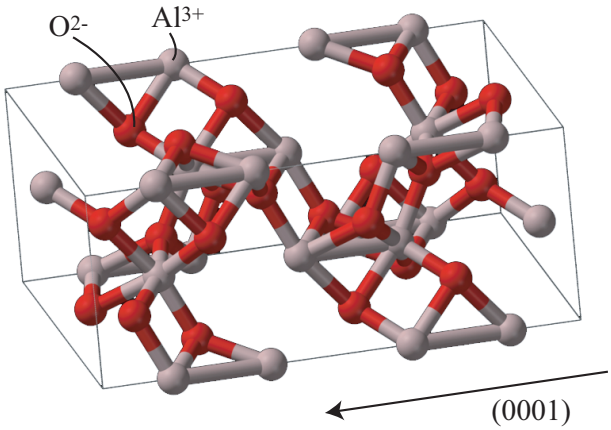

Figure 3.10: Al_2O_3 unit cell.[31] The crystal structure is corundum.

to ~ 0.4 T.[30] From the published data, it is possible to calculate the magnetostriction in arbitrary crystal directions. If the magnetization and observation direction cosines are (α_1 α_2 α_3) and (β_1 β_2 β_3), then the observed magnetostriction, $\lambda_{(\beta_1\beta_2\beta_3)}$ can be expressed as

$$\lambda_{(\beta_1\beta_2\beta_3)} = \frac{3}{2}\lambda'_{100}\left(\alpha_1^2\beta_1^2 + \alpha_2^2\beta_2^2 + \alpha_3^2\beta_3^2 - \frac{1}{3}\right) + 3\lambda'_{111}\left(\alpha_1\alpha_2\beta_1\beta_2 + \alpha_2\alpha_3\beta_2\beta_3 + \alpha_3\alpha_1\beta_3\beta_1\right), \quad (3.1)$$

where λ'_{100} and λ'_{111} are magnetostriction coefficients in the (100) and (111) directions.

Finally, Al_2O_3 substrates were used for preparing films for observing a light-induced phase transition in VO_2. Sapphire has many uses, such as a solid-state laser, abrasive polishing agent, etc. The sapphire crystals used as substrates were α-Al_2O_3 with a corundum structure and lattice parameters of a =4.763 Å and c =13.003 Å. The crystal structure is shown in Fig. 3.10. Resistivity is known to be very high, ~ 10^{15} Ωcm at RT. Films were grown on Al_2O_3 (0001) substrates. Even though this surface is hexagonal-like while VO_2 has a rectangular unit cell, it has been widely used for depositing VO_2 thin films[13–15] because lattice matching is actually rather good, as shown in Fig. 3.11. It is known that monoclinic VO_2 is (010) oriented on a Al_2O_3 (0001) surface at RT, and lattice mismatch is 5.1 % × 4.4 %.

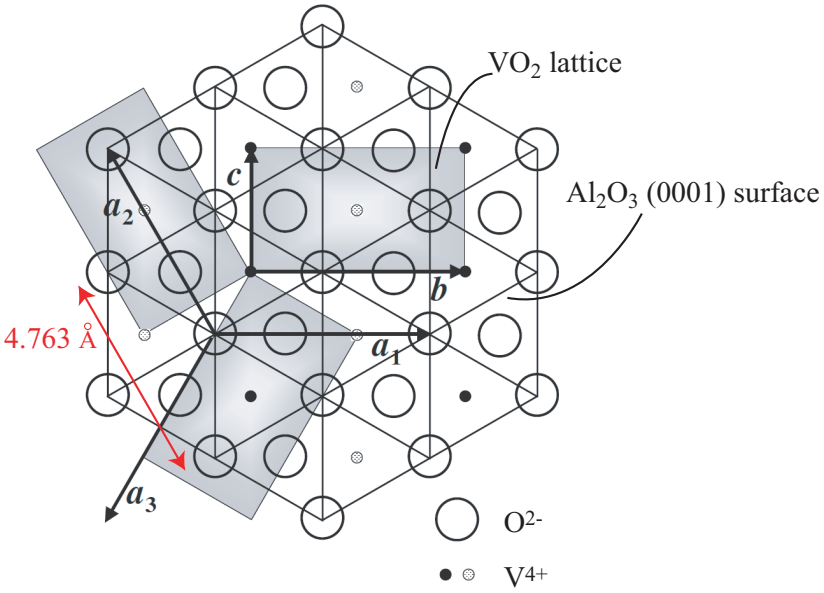

Figure 3.11: Schematic view of Al_2O_3 (0001) surface and tetragonal VO_2 lattice.[15]

References

[1]C. Kim, Y. Oikawa, J. S. Shin, and H. Ozaki, J. Phys. Condens. Matter **18**, 9863 (2006).

[2]V. Eyert, Ann. Phys. (Leipzig) **11**, 650 (2002).

[3]C. Chen, and Z. Zhou, APL **91**, 011107 (2007).

[4]J. M. Baik, M. H. Kim, C. Larson, C. T. Yavuz, G. D. Stucky, A. M. Wodtke, and M. Moskovits, Nano Letters **9**, 3980 (2009).

[5]H. Liu, S. Lysenko, A. Rua, V. Vikhnin, G. Zhang, O. Vasquez, and F. E. Fernandez, J. Luminescence **119-120**, 404 (2006).

[6]J. Y. Suh, R. Lopez, L. C. Feldman, and R. F. Haglund, Jr., JAP **96**, 1209 (2004).

[7]S. B. Wang, S. B. Zhou, and X. J. Yi, Vacuum **75**, 85 (2004).

[8]W. Burkhardt, T. Christmann, B. K. Meyer, W. Niessner, D. Schalch, and A. Scharmann, Thin Solid Films **345**, 229 (1999).

[9]S. Lysenko, A. J. Rua, V. Vikhnin, J. Jimenez, F. Fernandez, and H. Liu, Appl. Sur. Sci. **252**, 5512 (2006).

[10]C. H. Griffiths, and H. K. Eastwood, JAP **45**, 2201 (1974).

[11]V. S. Vikhnin, S. Lysenko, A. Rua, F. Ferandez, and H. Liu, Optical Materials **29**, 1385 (2007).

[12]P. Jin, K. Yoshimura, and S. Tanemura, J. Vac. Sci. Technol. A **15**, 1113 (1997).

[13]M. Nakajima, N. Takubo, Z. Hiroi, Y. Ueda, and T. Suemoto, APL **92**, 011907 (2008).

[14]J. Sakai, and M. Kurisu, PRB **78**, 033106 (2008).

[15]I. Yamaguchi, T. Manabe, T. Tsuchiya, T. Nakajima, M. Sohma, and T. Kumagai, JJAP **47**, 1022 (2008)

[16]V. A. Klimov, I. O. Timofeeva, S. D. Khanin, E. B. Shadrin, A. V. Ilinskii and F. Silva-Andrade, Technical Physics **47**, 1134 (2002).

[17]Y. Muraoka, and Z. Hiroi, APL **80**, 583 (2002).

[18]K. Okazaki, S. Sugai, Y. Muraoka, and Z. Hiroi, PRB **73**, 165116 (2006).

[19]A. Liebsch, H. Ishida, and G. Bihlmayer, PRB **71**, 085109 (2005).

[20]K. Okazaki, H. Wadati, A. Fujimori, M. Onoda, Y. Muraoka, and Z. Hiroi, PRB **69**, 165104 (2004).

[21]Y. Muraoka, Y. Ueda, and Z. Hiroi, J. Phys. Chem. Sol. **63**, 965 (2002).

[22]K. Nagashima, T. Yanagida, H. Tanaka, and T. Kawai, PRB **74**, 172106 (2006).

[23]C. N. Berglund, and A. Jayaraman, Physical Review **185**, 1034 (1969).

[24]V. S. Vikhnin, S. Lysenko, A. Rua, F. Fernandez, and H. Liu, PLA **343**, 446 (2005).

[25]Y. Yamamoto, K. Nakajima, T. Ohsawa, Y. Matsumoto, and H. Koinuma, JJAP **44**, L511 (2005).

[26]http://wikis.lib.ncsu.edu/index.php/Spinel.

[27]L. R. Bickford, Jr., J. Pappis, and J. L. Stull, Physical Review **99**, 1210 (1955).

[28]Ö. Özdemir, Geophys. J. Int. **141**, 351 (2000).

[29]http://www.irm.umn.edu/hg2m/hg2m_c/hg2m_c.html.

[30]C. W. Heaps, Physical Review **24**, 60 (1924).

[31]http://commons.wikimedia.org/wiki/File:Corundum-unit-cell-3D-balls.png.

Chapter 4

VO_2 phase transition and crystal bending

4.1 Introduction

It is known that the metal-to-insulator phase transition in VO_2 is sensitive to lattice strain. The purpose here is to find out if it is possible to control the transition between the insulating and metallic phases by applying a dynamic strain on a VO_2 thin film.

Strain can be applied to materials in many different ways. For thin films, lattice mismatch,[1] hydrostatic pressure,[2] substrate deformation,[3,4] thermally-induced structure transition of a substrate,[5] cantilevers,[6] and strain in nanobeams[7] have been used. The applied strain is generally uni- or bi-axial. Similar studies are, of course possible in bulk materials as well.[8,9] Most strain effect studies focus either on large static stress ($\sim$ 100 GPa) or small stress at very high frequencies, as in piezoelectric bulk materials ($\sim$ 10 kHz, $\sim$ 10 kPa). From the point of view of optimizing the performance of thin film based devices and material properties, a dynamic technique that can cover strains comparable to epitaxial mismatch effects would be desirable. The dynamic aspect is necessary for sensitive lock-in detection while strains should be comparable to levels found in practical heterostructures. Such a technique would make it possible to observe dynamic-strain-induced phase transitions, domain dynamics, and strain-dependent device characteristics.

One possible solution that is described in this work, is to construct a high-frequency crystal bending stage, as described in Section 4.2. This stage can induce large strain at moderate frequencies. Fig. 4.1 shows how the performance of a crystal bending approach compares with other strain experiments. A major advantage is that the

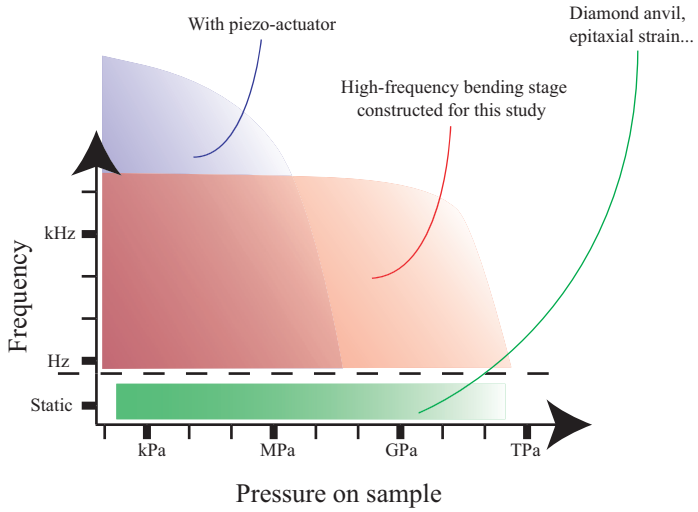

Figure 4.1: Frequency and pressure range of the high-frequency crystal bending stage and comparison with other strain experiments.

achievable strain in a thin film is comparable to what can be reached in bulk materials in quasi-static diamond anvil cell experiments. It is therefore reasonable to expect that by crystal flexing, it should be possible to observe new physical aspects of strain-induced non-equilibrium states in oxides and other materials.

In order to test this idea, VO_2 thin films grown on TiO_2 (001) substrates were used. The thin film fabrication details are presented in Section 4.3. This particular material was chosen because VO_2 has a monoclinic-to-tetragonal structural phase transition close to room temperature, accompanied by a sharp metal-to-insulator transition. Even in thin films, a resistance change by a factor of up to 10^4 can be seen and it is known that either tensile or compressive *c*-axis strain of around 0.8 % can shift the T_c by up to 50 K.[1] Results obtained under compressive *c*-axis dynamic strain are presented in Section 4.4.

4.2 High-frequency crystal bending stage

The design of the high-frequency bending stage is shown in Fig. 4.2. A stainless steel frame is used to hold a sample and a piezoelectric actuator. The sample, in this case a thin film epitaxially grown on a substrate, is attached to a doped Si substrate with a thermally conducting glue. The silicon substrate is used as a flexible heater. The

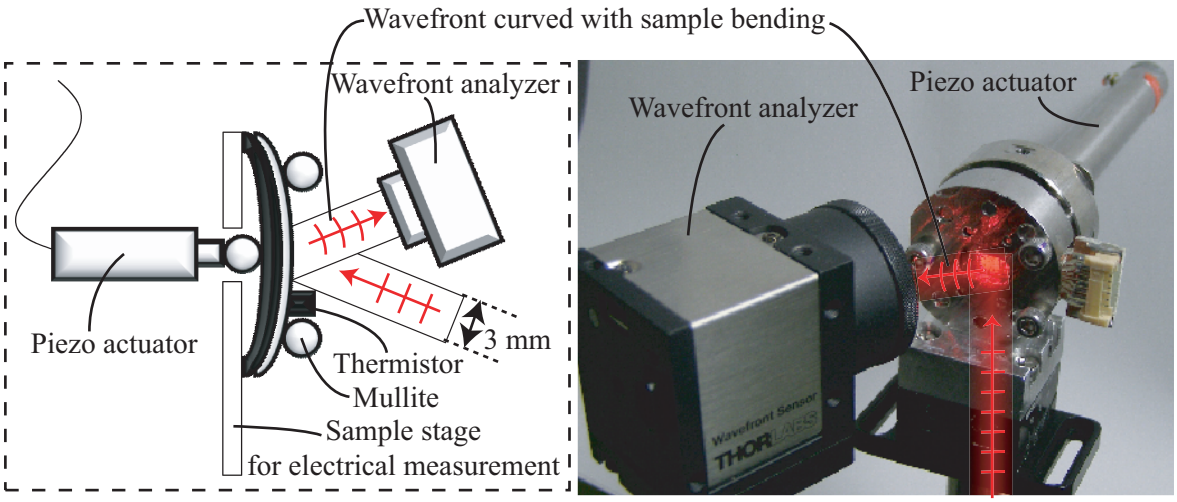

Figure 4.2: A sketch (a) and a photo (b) of the high-frequency bending stage.

whole sandwich structure is pressed against two tube-shaped 2 mm diameter mullite ceramic spacers that run along the edges of the sample. The ceramic spacers are needed for isolating the sample film both electrically and thermally from the stage body. The distance between the ceramic spacers was 8 mm.

Another ceramic tube was pressed against the back of the sample at the center and held in place by the piezo actuator. The maximum displacement of the actuator was about 60 μm although in actual measurements a typical movement range was about 20 μm. A simple counter-screw setup was used for coarse adjustment of the actuator position, allowing for different sample thicknesses to be used and presetting the pressure on the sample crystal.

The reason why the dynamic strain range of this stage can reach pressures that are comparable with static strain experiments, as shown in Fig. 4.1, is the difference in which the pressure is applied, as illustrated in Fig. 4.3. Most of the direct methods, such as a diamond anvil cell or a simple press induce strain by pressing on the sample itself (Fig. 4.3(a)) while the current method induces strain in a very thin film by bending the substrate on which the film was grown (Fig. 4.3(b)). The substrate thus works as a mechanical force amplifier, where actuator movement range is traded for much larger in-plane pressure. This method is therefore a much more efficient way for inducing strain with pressure, but only applicable to thin films that are grown on a thick substrate.

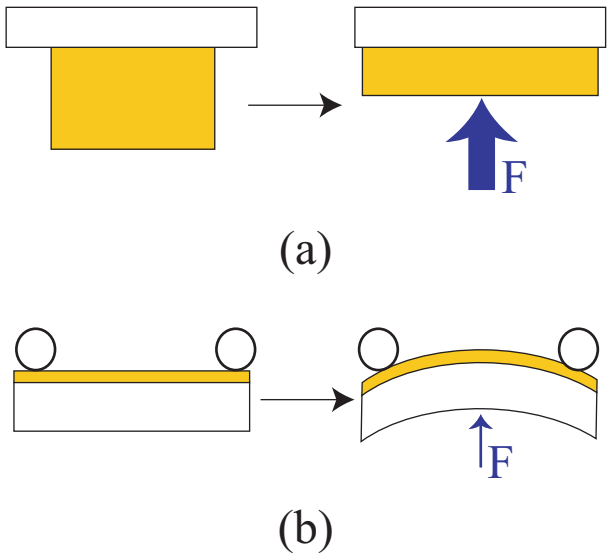

Figure 4.3: Direct methods (a) and the current method (b) for applying pressure to a sample. The left and right figures illustrate deformation states before and after applying pressure, respectively.

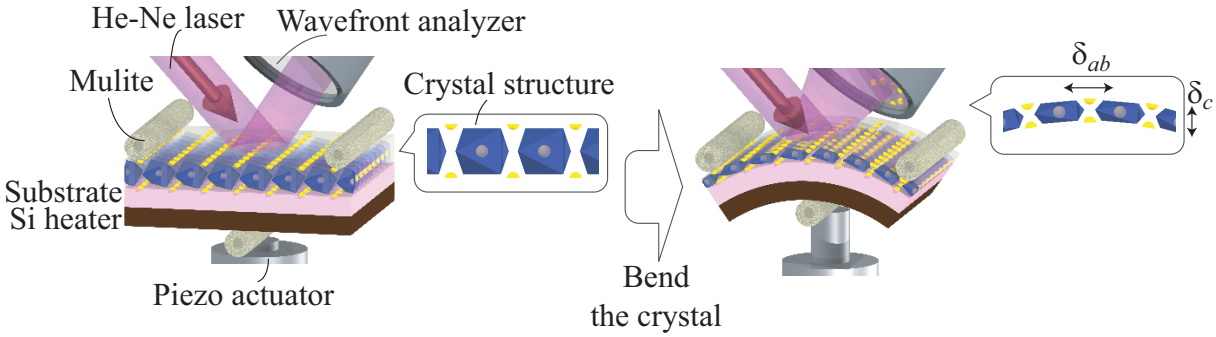

Figure 4.4: Conceptual diagram of the high-frequency bending stage.

The concept of how strain can be induced by bending the substrate is shown in Fig. 4.4. If the substrate is pressed from the opposite side of the thin film, the sample film will develop tensile in-plane strain, δ_{ab} and compressive out-of-plane strain, δ_c. The actual sample surface deformation was measured with a wavefront analyzer. Strain in the film was calculated from the surface shape data as explained in Section 4.4.1. The change of the out-of-plane lattice parameter, δ_c was calculated from the Poisson ratio.[10] It is possible to apply in-plane tensile strain, δ_{ab} of up to 0.05 %, which corresponds

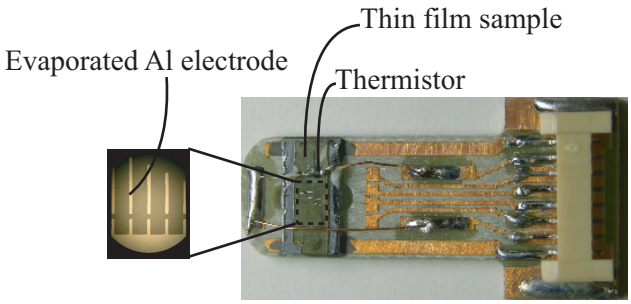

Figure 4.5: The sample holder used for electrical measurement in the high-frequency bending stage.

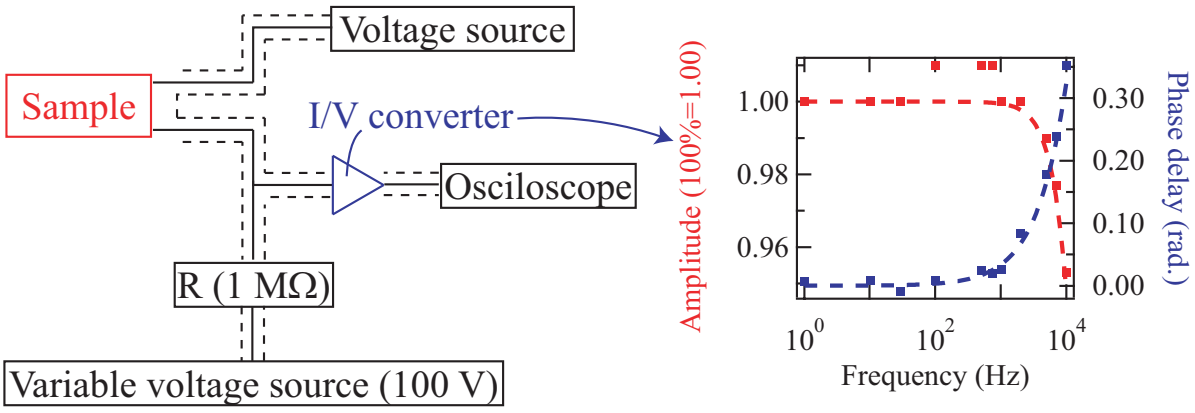

(a) (b)

Figure 4.6: (a) Connection diagram for measuring the electronic resistance of the thin film in the high-frequency bending stage. (b) The frequency response of the I/V converter amplifier used for observing the resistance change in (a).

to a 0.02 % compressive out-of-plane strain δ_c, as shown in Fig. 4.4. In that case, the observed mechanical deformation corresponds to a *c*-axis stress of 20 MPa, calculated from VO_2 Young's modulus.[11]

The sample holder is shown in Fig. 4.5. Transport properties of the film were measured during bending by patterning suitable Al electrodes on the sample surface and attaching flexible wire probes by ultrasonic wire bonding. The sample holder has multiple roles. It is used for fixing the sample during bending but also for controlling the sample temperature. For this purpose, a thermistor was attached to the film surface

and a silicon heater was mounted under the sample crystal. A single connector was used to attach the measurement electronics to the sample holder.

The driving voltage of the piezo actuator and the sample resistance response were monitored on a digital oscilloscope. The resistance change of a VO_2 film can be quite small during bending. Typical relative resistance change in measurements was less than 2 %. It was therefore necessary to construct a suitable electronic setup, as illustrated in the diagram in Fig. 4.6(a). In this diagram, the static offset of the sample resistance could be eliminated by feeding a small compensating current into the input of the I/V converter through a large resistor. The circuit thus functioned as a half bridge. Fig. 4.6(b) shows the frequency response of the I/V converter that was used to analyze the frequency dependence of the sample response to dynamic strain. The I/V converter had an effective bandwidth of 1 kHz, which was sufficient for the purpose of measuring the strain response in VO_2.

The actual sample surface deformation was measured with a Hartmann-type wavefront analyzer.[12] The working principle of the wavefront analyzer is explained in Fig. 4.7(a). The surface-probing He-Ne laser (λ = 633 nm, power 2 mW) beam diameter was 3 mm. The laser light passed through a beam expander which was adjusted with the help of the wavefront analyzer so that the wavefront of the laser light hitting the sample surface was flat. The actual shape of the sample surface determines the wavefront shape of light reflected from the sample surface. The wavefront shape of the reflected laser beam is analyzed with a microlens array, which is placed a few mm above a CCD camera image sensor. Each microlens produces a focal spot on the CCD surface. If the wavefront is locally tilted, the focal spot would shift from the microlens center position. By analyzing the deviations of each microlens focal spot from the center position, it is possible to reconstruct the wavefront of the light entering the camera. The maximum area that can be analyzed is limited by the size of the image sensor, which was 3.2×3.2 mm^2. A laser beam with a diameter of 3 mm was therefore used.

The actual sample strain components, δ_{ab} and δ_c (explained in Section 4.4.1), were calculated from the wavefront shape data shown in Fig. 4.7(b). The advantage of this optical method for observing the sample strain is that it is not necessary to make contact with the sample surface and most of the nonidealities introduced by deformations of the sample stage itself can be ignored, greatly simplifying the mechanical design.

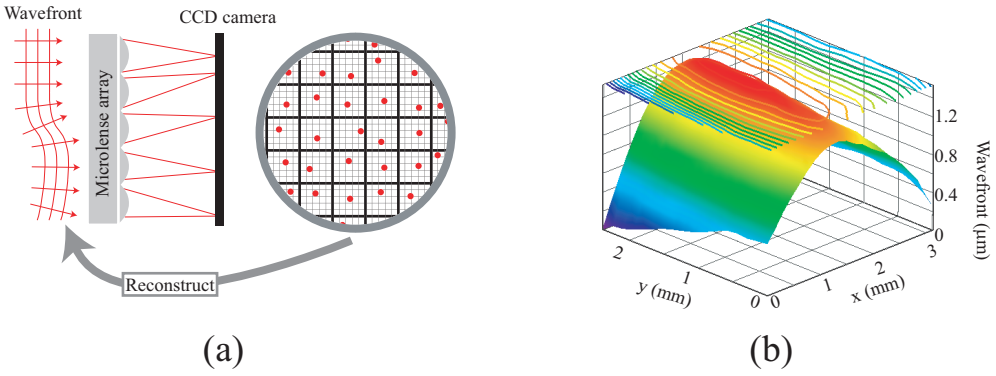

Figure 4.7: (a) The working principle of a Hartmann-type wavefront analyzer. (b) The semi-cylindrical wavefront observed by the Hartmann-type wavefront analyzer for light reflected from a deformed thin film sample.

4.3 Fabrication of VO_2 thin films on TiO_2 substrates

The VO_2 thin films were fabricated on TiO_2 substrates under various conditions. At first, for looking into the grain size dependence of the dynamic strain response, an attempt was made to obtain a TiO_2 (001) surface that would be flat on the nm scale even though the commercial crystals are not as flat. This process is described in Section 4.3.1. After that, VO_2 thin films were deposited on TiO_2 (001) substrates under various conditions as described in Section 4.3.2.

4.3.1 Surface roughness of TiO_2 substrates

Flat TiO_2 (001) substrates were necessary for determining the grain size dependence of the dynamic strain response. Although there are reports of obtaining atomically flat surfaces,[13] the process is not always repeatable and appears to depend on the quality of the original substrate crystal. Due to this, step-and-terrace TiO_2 (001) substrates are generally not offered commercially, e.g. by Shinkosha Co., Ltd. However, NH_4F-HF (BHF) etched substrates are commercially available and were also used in this work (Fig. 4.8). The etched surface was better than that of the polished-only crystal although surface steps were not visible. The main advantage was that an atomically flat surface could only be obtained by annealing an etched substrate.

The annealed TiO_2 (001) surfaces of BHF etched substrates are shown in Fig. 4.9. The substrates were annealed in air for 3 h and at 800 °C, 850 °C, 900 °C, and 1000 °C. As can

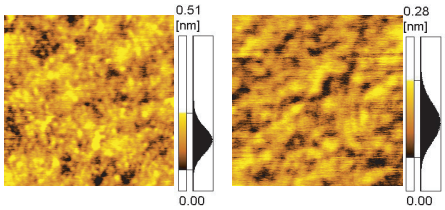

Figure 4.8: AFM images (0.5×0.5 μm^2) of a TiO_2 (001) substrate obtained from Shinkosha Co., Ltd. The substrate in (a) is only polished. The crystal in (b) was also BHF etched.

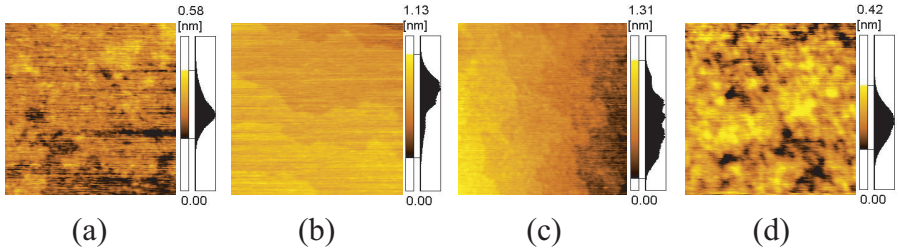

Figure 4.9: AFM images (0.5×0.5 μm^2) of polished and etched TiO_2 (001) substrates after annealing in air for 3 h at (a) 800 °C, (b) 850 °C, (c) 900 °C, (d) 1000 °C.

be seen in Fig. 4.9, the best temperature for getting a flat step-and-terrace surface was 850 °C. In later references the annealed substrates are referred to as "atomically flat TiO_2 substrate" while non-annealed substrates are referred to as "normal TiO_2 substrate".

4.3.2 Deposition of VO_2 thin films on TiO_2

A valuable reference for growing VO_2 films on TiO_2 substrates is a paper by Muraoka et al.[1] The authors have also studied the effect of static strain on VO_2. Obtaining the correct oxygen stoichiometry in VO_2 is critical. the effects of oxygen pressure on VO_2 properties are discussed by Griffiths.[14]

As a first step, the growth temperature, T_{sub} and oxygen background pressure were optimized in terms of the resistance change at the phase transition. Numerically, the relevant value is the temperature coefficient of resistance (TCR), defined as $\frac{\Delta R_{tem}}{\Delta T}\frac{1}{R}$ at the transition point. The purpose of thin film growth parameter optimization was to maximize the TCR value. Empirically, it was observed that as the growth temperature T_{sub} deviated from a critical value, the transition temperature T_c became higher (closer

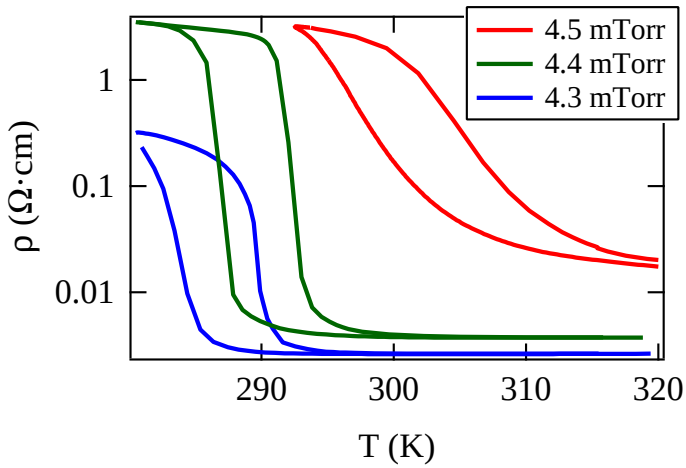

Figure 4.10: O_2 pressure dependence of VO_2 film resistance behavior. Other deposition conditions were: thickness 10 nm, T_{sub} = 440 °C, clamping: metal plate, substrate: normal.

to the bulk value), resistance of both phases increased, and the TCR at the transition point became lower. Moreover, higher T_{sub} generally resulted in films with a smaller hysteresis width observed in temperature vs. resistance scans.

The transition behavior of VO_2 films was found to be very sensitive to the oxygen pressure during growth. As shown in Fig. 4.10, increasing growth pressure resulted in higher resistance and a lower TCR at the transition point. The optimum oxygen pressure value in this case was 4.4 mTorr. These results are similar to what has been observed before,[14] but the growth parameters need to be optimized for each growth chamber. The growth optimization also showed, as can be seen in Fig. 4.10 that increasing O_2 pressure generally resulted in increasing T_c, approaching the unstrained bulk value.

Two types of VO_2 films were characterized, those grown by ELAMOD and PLD techniques.

For ELAMOD, the deposition conditions were the following. Vanadium (V) carboxylate solution (V carboxylate + xylene) with a concentration of 2 % was spin-coated onto a TiO_2 (001) substrate at 3000 rpm for 10 s. The coated films were pre-heated at 300 °C in air for 10 min, and then the films were irradiated by a KrF excimer laser (λ = 248 nm; Lambda Physik Compex110) at room temperature in air. The laser fluence was 100 mJ/cm^2, and the repetition rate was 10 Hz. The irradiation time was 10 min. The film thickness was measured with TEM, and the value was ~ 25 nm.

For PLD, the deposition conditions were the following. A gradient thickness VO_2

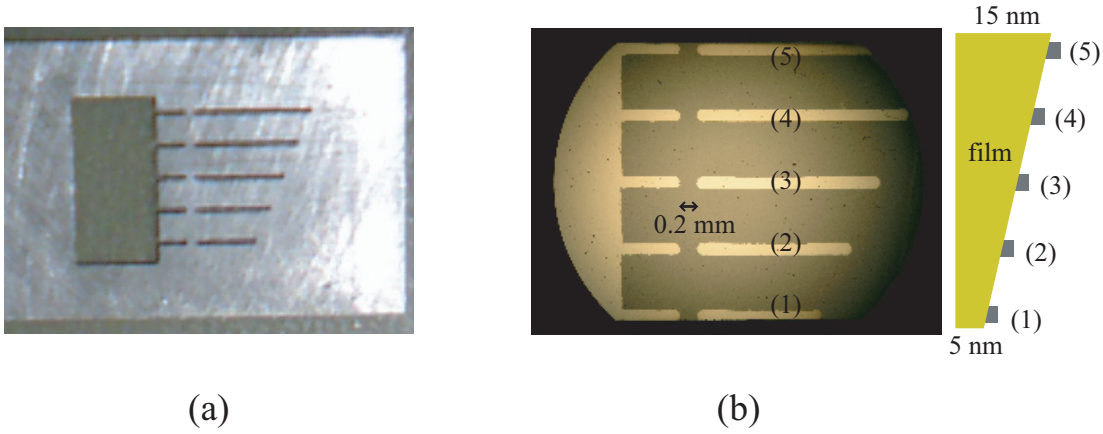

Figure 4.11: (a) Be:Cu mask for fabricating Al electrodes on a thin film. (b) VO_2 film surface after evaporating the Al electrodes. Distance between electrodes is 0.2 mm. Electrode numbers, 1 to 5, are shown in the figure. A cross-section diagram is also shown in the right.

thin film on a single TiO_2 (001) substrate ($9 \times 3 \times 0.2$ mm^3) was used for studying the thickness dependence of dynamic strain response. The thickness gradient was directed along the shorter, 3 mm direction of the substrate. A metal (Be:Cu) mask was milled and used as a stencil for evaporating Al electrodes on the VO_2 thin films surface in order to measure the local electrical resistance. The film and electrode layout are shown in Fig. 4.11. The gradient thickness was 5 nm at the minimum and 15 nm at the maximum. In other words, electrodes 1 to 5 in Fig. 4.11(b) were used for measuring the local resistance at thickness points corresponding to 5 nm, 7.5 nm, 10 nm, 12.5 nm, and 15 nm. Sample clamping with metal side-clamps was used instead of wires in order to fabricate a continuous gradient.

For deposition, the laser fluence was 560 mJ/cm^2 at an ablation spot size of 0.06 cm^2. Laser frequency was 1 Hz, giving a growth rate of ~0.005 nm/pulse. It was found that the V_2O_3 target surface is unstable in UHV conditions. The target surface was therefore prepared by performing a pre-ablation of 10000 pulses at 10 Hz before deposition. Film growth optimizations, illustrated in Fig. 4.10, resulted in a choice of 4.4 mTorr O_2 pressure for deposition. The growth temperature had a broader process window and therefore two growth temperatures were used, with T_{sub} either 440 °C or 480 °C. Two types of substrates were also used, including normal unetched TiO_2 and atomically flat etched and annealed TiO_2 substrates.

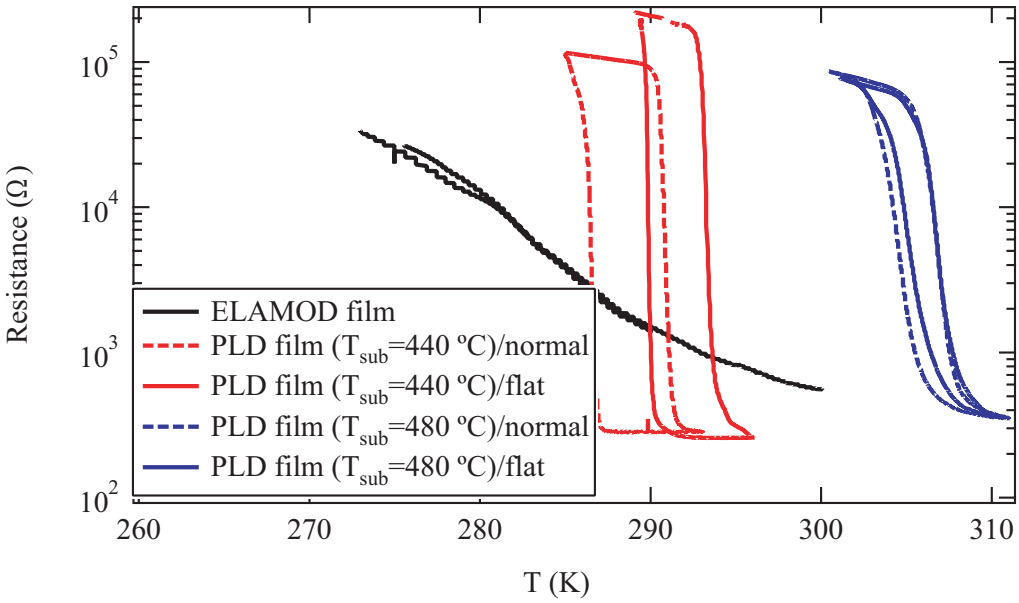

Figure 4.12: Resistance of VO_2 films deposited at various conditions. For the ELAMOD film, deposition conditions are given in the text. For the PLD films, P_{O_2}=4.4 mTorr, thickness 10 nm, clamping: metal plate.

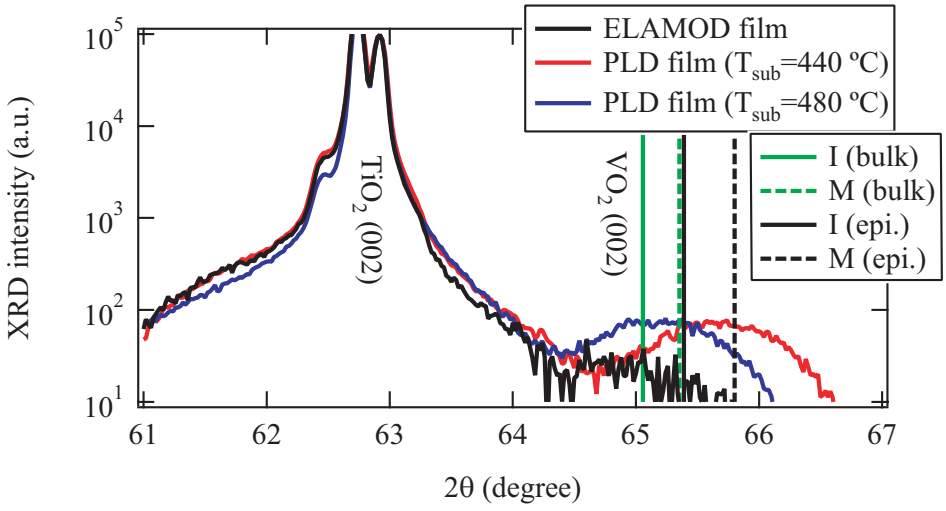

Figure 4.13: XRD data of VO_2 films deposited at various conditions and measured at RT (~300 K). The *c*-axis values of VO_2 bulk material for the metallic and insulating phases are shown with dotted lines. For the ELAMOD film, the deposition procedure is given in the text part. For the PLD films, O_2 pressure was 4.4 mTorr, thickness 10 nm, clamping: metal plate, substrate: normal.

The resistance behavior of various characteristic films are shown in Fig. 4.12, which include an ELAMOD film for comparison as well. For the PLD films, the thickness was 10 nm and for thickness gradient samples, the resistance was measured at electrode position 3, as shown in Fig. 4.11. It is clear that the films grown at T_{sub} =440 °C have a larger TCR and hysteresis width than those grown at T_{sub} =480 °C. The difference between normal and flat substrates is mainly in the hysteresis width with films grown on atomically flat TiO_2 substrate generally having a smaller hysteresis width. The main distinctive property of the ELAMOD film is that there is no hysteresis in a temperature scan. This is due to a complicated microstructure of the film, which was optimized for use as a temperature sensor device. Film structures were measured with XRD as shown in Fig. 4.13. The thickness gradient films could not be used for XRD analysis. For measuring XRD, constant thickness 10 nm sample was used instead. As XRD was measured at room temperature, the ELAMOD film and PLD films grown at T_{sub} =440 °C were in the metallic phase while the PLD films grown at T_{sub} =480 °C were in the insulating phase, as can be seen from the temperature dependence of resistance curves in Fig. 4.12. The *c*-axis length can be calculated from Fig. 4.13 as 2.879 Å, 2.845 Å, and 2.863 Å for the ELAMOD film and PLD films with T_{sub} =440 °C and 480 °C, respectively. As the *c*-axis values of bulk VO_2 are 2.856 Å in the metallic phase and 2.872 Å in the insulating phase, the *c*-axis length ratios (film value/bulk value) are 1.008, 0.996, and 0.997 for the ELAMOD and PLD films with T_{sub} =440 °C, and 480 °C, respectively. The VO_2 films thus have tensile strain in the in-plain direction when grown on TiO_2 (001) substrates by PLD. Due to strain in the film, the *c*-axis becomes smaller than the bulk value, as usual. For the ELAMOD film, the crystal structure appears to have expanded due to the high density of structural defects and a complex grain structure.

The thickness dependence of resistance behavior was also studied. The main question was, how possible grain size changes would affect the resistance behavior and strain response. As the film thickness increases, the grain area tends to become bigger, as shown in Fig. 4.14. The average grain area was calculated from the AFM results. Moreover, the resistance behavior was quite different between different thicknesses, as shown in Fig. 4.15. From Fig. 4.12 and Fig. 4.14, one can conclude that there is a general tendency of bigger grain size leading to a smaller hysteresis width. A similar behavior has also been observed in previous studies.[15,16] Four resistance plots for 10 nm films in Fig. 4.15 are the same as those in Fig. 4.12.

In order to study the domain morphology in VO_2 films, additional VO_2 film samples were grown on conducting Nb:TiO_2 (001) substrates. The purpose was to correlate the

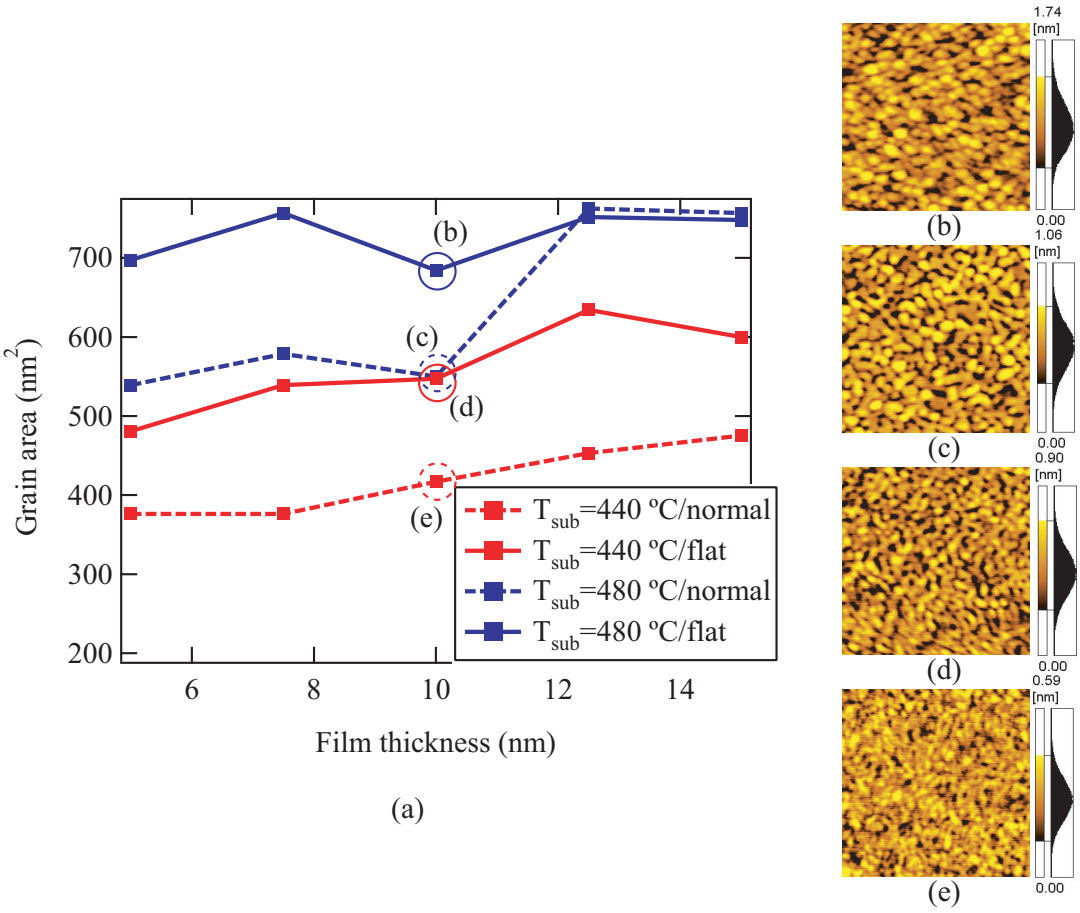

Figure 4.14: (a) Thickness dependence of grain size of VO_2 films deposited at various conditions. (b-e) AFM images (0.5×0.5 μm^2) of VO_2 film samples with thickness 10 nm, and T_{sub} = 480 °C/flat (b), T_{sub} = 480 °C/normal (c), T_{sub} = 440 °C/flat (d), T_{sub} = 440 °C/normal (e). Other deposition conditions were: O_2 pressure 4.4 mTorr, clamping: metal plate.

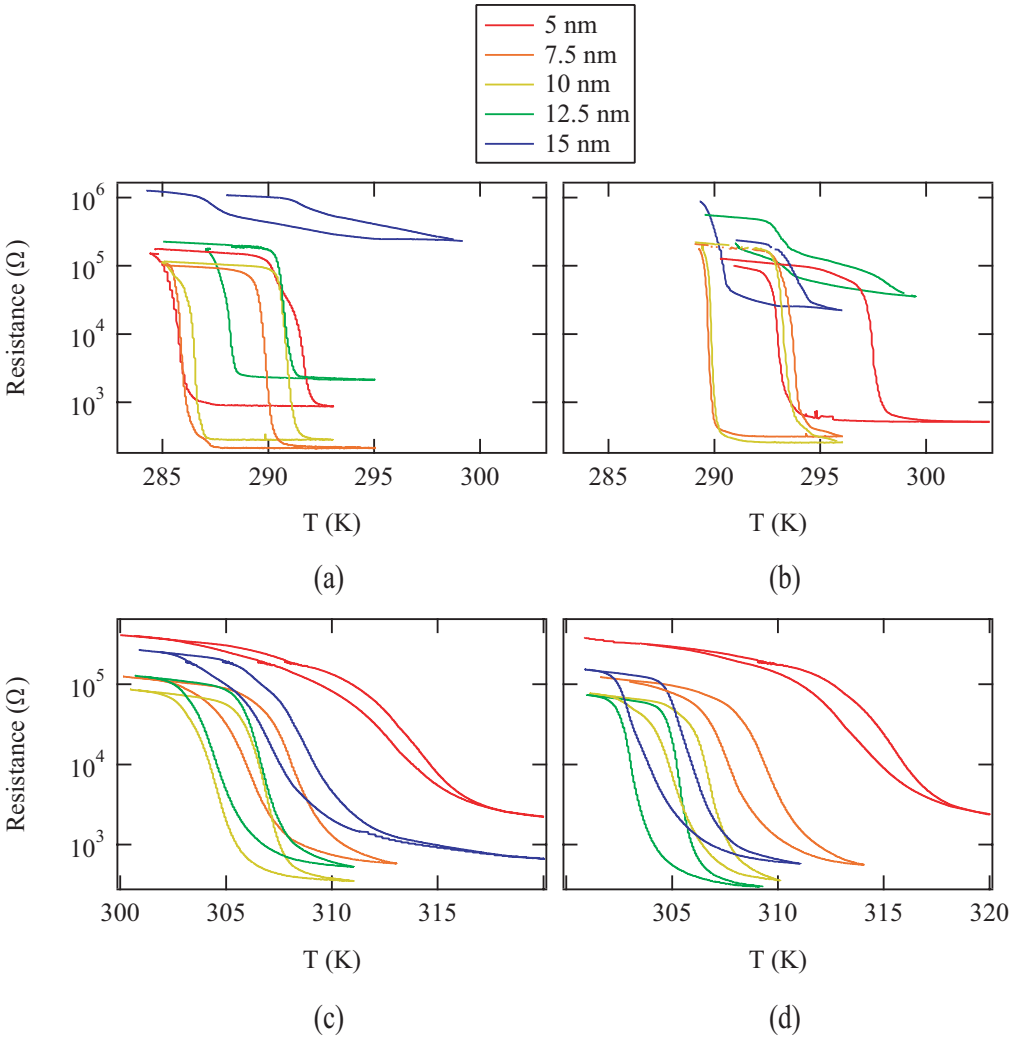

Figure 4.15: Resistance behavior of VO_2 films deposited at T_{sub} = 440 °C/normal (a), T_{sub} = 440 °C/flat (b), T_{sub} = 480 °C/normal (c), T_{sub} = 480 °C/flat (d).

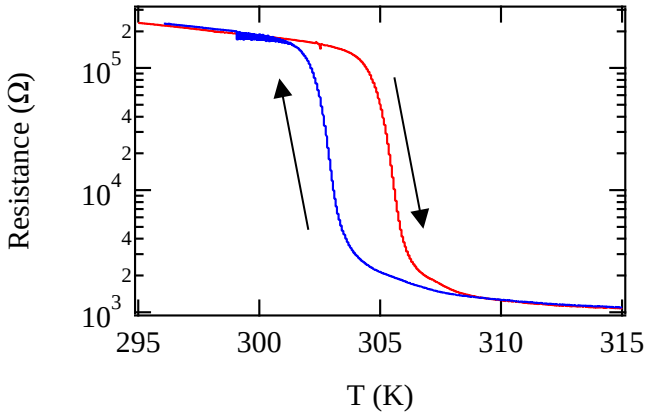

Figure 4.16: Resistance behavior of a VO_2 thin film deposited on Nb:TiO_2 (001) substrate. Deposition condition were: O_2 pressure 4.4 mTorr, thickness 12.5 nm, T_{sub} = 500 °C, clamping: wire.

observed strain relaxation in films under dynamic strain with the domain switching dynamics. This can be done by observing the appearance of metallic domains in the film by conducting-tip AFM that can probe the presence of local metallic regions in an otherwise insulating film. Due to a different substrate thickness and clamping, the deposition parameters in this case may have deviated slightly from other films described in this study. The purpose was to use the same T_{sub} = 480 °C with the thickness of 12.5 nm. However, we chose T_{sub} = 500 °C because wire clamping was used instead of metal plate clamps, and the substrate thickness was 0.5 mm (not 0.2 mm). It should be noted that during the deposition, the substrate surface temperatures were very similar, since the pyrometer measures the temperature of the sample mounting block during deposition. Resistance behavior which was measured with silver paste bonding is shown in Fig. 4.16. The resistance behavior was very similar to films that were grown on insulating substrates at T_{sub} = 480 °C with a thickness of 12.5 nm.

4.4 Results and Discussions

4.4.1 Analysis of the results

The *c*-axis strain in VO_2 thin films was calculated from wavefront analyzer data reflecting the actual shape of the strained film. The time response to dynamic strain was

assumed to follow a double exponential model.

Calculation of strain value

The diagram of a deformed substrate and some of the parameters used for calculation are shown in Fig. 4.17. Sample deformation from the original point, $\varepsilon(x)$ is the surface shift distance from the unstrained equilibrium position as a function of lateral position along the x-axis. The x-axis runs parallel to the length of the substrate, with the distance between support points denoted L. Strain is applied to the sample at the center of the substrate in a 3-point bending geometry, as shown in Fig. 4.2(a). In this case, $\varepsilon(x)$ can be represented as

$$\varepsilon(x) = \frac{Fx^2(3L - 2|x|)}{8Yt^3y}, \tag{4.1}$$

where F is the bending force at the center, t and L are the thickness and the length of the sample substrate, respectively, Y is TiO_2 Young's modulus, and y is the width of the substrate. Displacement at the center of the sample crystal, $\varepsilon(L/2)$, can be calculated from Eq. 4.1 as

$$\frac{\varepsilon(x)}{\varepsilon(L/2)} = \frac{2x^2(3L - 2|x|)}{L^3}. \tag{4.2}$$

The in-plane strain, δ_{ab}, is a function of the distance from the center of the substrate in the radial direction, perpendicular to the x axis. However, the film thickness is

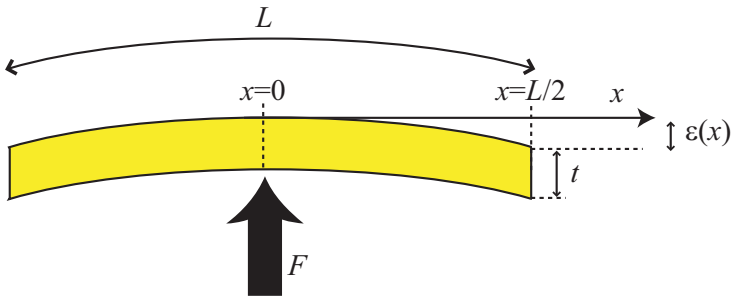

Figure 4.17: Deformed sample substrate and definition of some parameters. F is the bending force, applied at the sample center, t and L are the thickness and the length of the sample substrate, respectively. x-axis is parallel to the length direction with $x = 0$ corresponding to the center of the sample. Bending is measured by $\varepsilon(x)$, which is a function of x.

much smaller than the substrate thickness and it is therefore possible to assume that δ_{ab} always has the same value as the value at the substrate surface. In this case it is possible to express δ_{ab} as

$$\delta_{ab} = \frac{t}{2R(x)} = \frac{t}{2}\left\{\frac{1}{[1+\varepsilon'(x)^2]^{3/2}}\frac{\mathrm{d}^2\varepsilon}{\mathrm{d}x^2}\right\} \sim \frac{t}{2}\frac{\mathrm{d}^2\varepsilon}{\mathrm{d}x^2} = \frac{12t\varepsilon(L/2)}{L^3}\left(\frac{L}{2} - |x|\right), \tag{4.3}$$

where $R(x)$ is the curvature radius, and it is assumed that $\varepsilon(x)$ is very small. In such a case, δ_c can be calculated from δ_{ab} as

$$\delta_c = -0.3892 \times \delta_{ab}, \tag{4.4}$$

where a published Poisson ratio[10] has been inserted. The resistance of the film was measured at the center part with an electrode distance of 0.2 mm, as shown in Fig. 4.11(b) while $L = 8$ mm, which is the distance between the ceramic spacers. It can then be assumed that δ_{ab} and δ_c are constant in the measurement area. Finally, δ_c can be calculated from Eqs. 4.3 and 4.4 as

$$\delta_c = -0.3892\times\delta_{ab} \sim -0.3892\times\frac{12t\varepsilon(L/2)}{L^3}\left(\frac{L}{2} - 0.05\ \mathrm{mm}\right) = -3.6\times10^6\times t\varepsilon(L/2)\ \%/\mathrm{m}^2. \tag{4.5}$$

If t and $\varepsilon(L/2)$ are known, it is possible to calculate δ_c. Here, δ_c can be calculated from wavefront analyzer data.

The wavefront shape function is not exactly the same as the sample deformation function, $\varepsilon(x)$, but the deviation is not significant in the center of the substrate. It is therefore possible to approximate the wavefront shape with a parabolic function in the fitting area (2 mm diameter circle) since $\varepsilon(x)$ near the center part is also approximately parabolic, as shown in Eq. 4.1. The wavefront analyzer software performs real-time Zernike fitting to the raw wavefront data and it is therefore easy to extracting the parabolic components from the 2D wavefront data in real time. By fitting, the wavefront deformation value at the sample center can be obtained, $\varepsilon_{\mathrm{wave}}$ (see Fig. 4.18). Next, it is necessary to calculate $\varepsilon(L/2)$ from $\varepsilon_{\mathrm{wave}}$ by solving the following simultaneous equations

$$\begin{cases} L_{\mathrm{center}} = \varepsilon(x_{\mathrm{edge}}) + L_{\mathrm{edge}} \\ x_{\mathrm{edge}} + L_{\mathrm{edge}}\sin(2\theta) = 1\ \mathrm{mm} \\ L_{\mathrm{center}} + \varepsilon(x_{\mathrm{edge}}) - L_{\mathrm{edge}}\cos(2\theta) = \varepsilon_{\mathrm{wave}} \end{cases}, \tag{4.6}$$

where L_{center} is the camera length, x_{edge} is the distance between the reflecting point corresponding to the wavefront edge part and the center point, L_{edge} is the distance between the reflecting point corresponding to the wavefront edge part and the wavefront

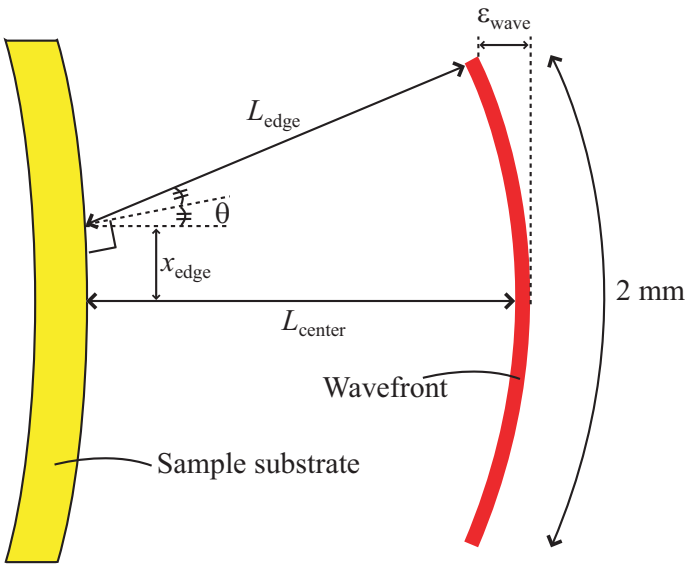

Figure 4.18: Sample substrate and the actual wavefront are shown. The camera length, L_{center}, is 50 mm. At the center part of the substrate, $\varepsilon(x)$ has an approximate parabolic shape. Therefore, only the parabolic component of the shape fitting was used.

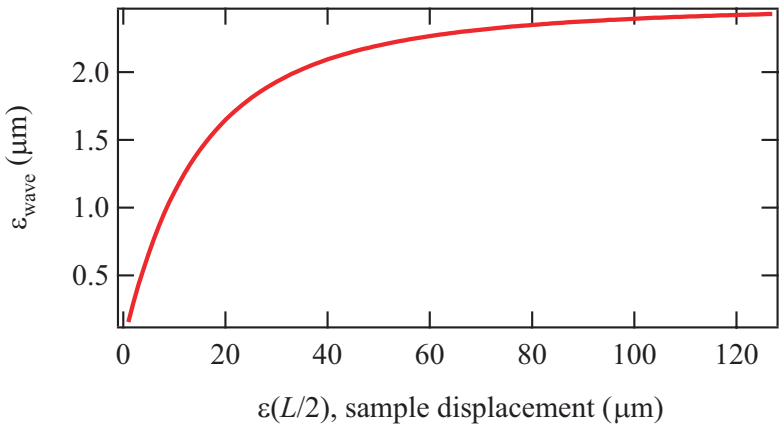

Figure 4.19: The relation between typical displacements at the center of the sample substrate, $\varepsilon(L/2)$, and of the wavefront, $\varepsilon_{\text{wave}}$. The calculation was done assuming $L = 8$ mm, which is the distance of the two fixed ceramic spacers.

edge, and $\theta = \varepsilon'(x_{\text{edge}})$, as shown in Fig. 4.18. Solving Eq. 4.6, gives a relation between $\varepsilon(L/2)$ and $\varepsilon_{\text{wave}}$, as shown in Fig. 4.19, where $L_{\text{center}} = 50$ mm and $L = 8$ mm.

For calculating δ_c, t (thickness) and $\varepsilon(L/2)$ as in Eq. 4.5 need to be known. While the process of getting the value of $\varepsilon(L/2)$ has been explained, obtaining a proper value for t is not quite straightforward. This will be discussed in Section 4.4.2. For dynamic strain, the strain value was estimated based on wavefront data obtained at a bending frequency of 0.05 Hz. This limitation exists because the wavefront analyzer is based on a conventional video-rate camera, which can only output a few tens of images per second. There is also an additional data processing delay due to image transfer and the Zernike wavefront shape fitting.

Double exponential model for VO_2 phase transition

The raw data for dynamic-strain-induced phase transition response is shown in Fig. 4.20. It is obvious that the resistance oscillates with alternating strain input. For analyzing this data, it is necessary to define some parameters as explained below. ΔR and $\Delta\delta_c$ are the peak-to-peak values of the resistance and out-of-plane strain δ_c, respectively. R_{max} is the maximum value of the resistance and $\Delta\phi$ is the phase delay between strain input and resistance output.

The phase delay can be caused by time constants of relaxation. An assumption was

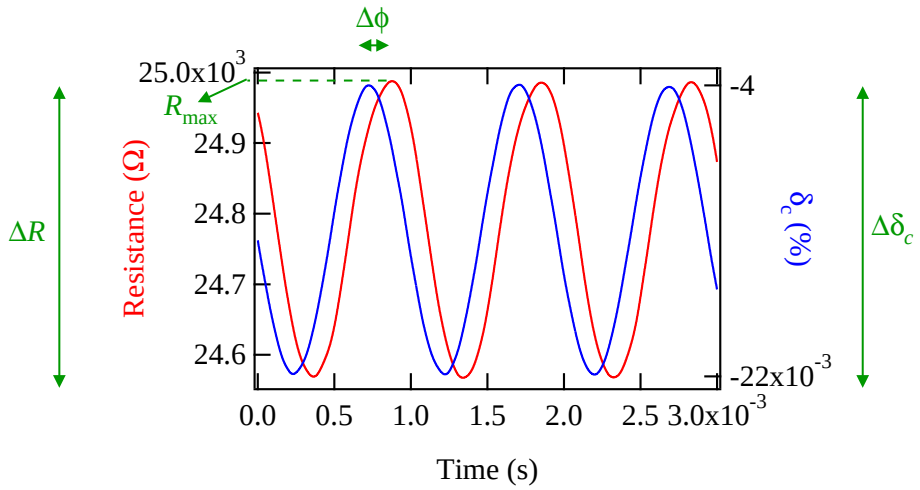

Figure 4.20: Raw oscilloscope data of the actuator voltage (converted to δ_c) and sample resistance at 1 kHz. Phase delay between the two signals can be seen here.

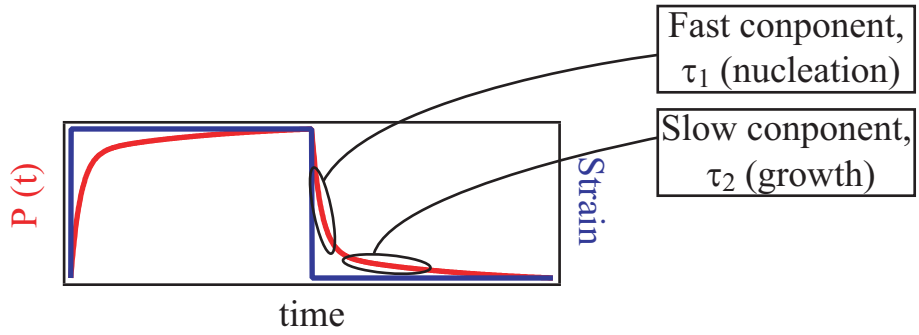

Figure 4.21: The explanation of double exponential model (see Eq. 4.7). Resistance (here written as $P(t)$) response has two time constants, τ_1 and τ_2, assuming the strain input is step-like.

therefore made that the resistance change $\frac{R}{R_{max}}$ in response to a stepwise strain change would follow a double exponential function as

$$\frac{R}{R_{max}} \propto s(t) = \alpha \exp\left(-\frac{t}{\tau_1}\right) + (1-\alpha)\exp\left(-\frac{t}{\tau_2}\right), \tag{4.7}$$

where R is the resistance, t is time, τ_1 and τ_2 are time constants ($\tau_1 < \tau_2$), and α is a scaling factor (see Fig. 4.21). This assumption can be supported by experimental reslults, specifically the time dependence (Fig. 4.22(a)) and the frequency dependence (Fig. 4.22(b)). For the time dependence, the data can be successfully fitted (Fig. 4.22(a)) with Eq. 4.7. For the frequency dependence, it is necessary to calculate the AC response of the system following Eq. 4.7 as below. If input and output functions are harmonic, following $\sin(\omega t)$ and $f(\omega, \tau_1, \tau_2, \alpha)\sin\left\{wt - \Delta\phi(\omega, \tau_1, \tau_2, \alpha)\right\}$ respectively, the relation between them can be written as

$$f(\omega, \tau_1, \tau_2, \alpha)\sin\left\{wt - \Delta\phi(\omega, \tau_1, \tau_2, \alpha)\right\} = \int_0^t \frac{\mathrm{d}s(t-\tau)}{\mathrm{d}\tau}\sin(\omega\tau)\mathrm{d}\tau. \tag{4.8}$$

By solving Eq. 4.8, f and $\Delta\phi$ can be written as

$$f(\omega, \tau_1, \tau_2, \alpha) =$$

$$\sqrt{\frac{\alpha^2}{1+(\omega\tau_1)^2} + \frac{(1-\alpha)^2}{1+(\omega\tau_2)^2} + 2\frac{\alpha(1-\alpha)}{\sqrt{1+(\omega\tau_1)^2}\sqrt{1+(\omega\tau_2)^2}}\cos\left(\tan^{-1}(\omega\tau_1) - \tan^{-1}(\omega\tau_2)\right)}, \tag{4.9}$$

$$\Delta\phi(\omega,\tau_1,\tau_2,\alpha) = \tan^{-1}\left(\frac{\dfrac{\alpha}{1+(\omega\tau_1)^2}\omega\tau_1 + \dfrac{1-\alpha}{1+(\omega\tau_2)^2}\omega\tau_2}{\dfrac{\alpha}{1+(\omega\tau_1)^2} + \dfrac{1-\alpha}{1+(\omega\tau_2)^2}}\right) \quad , \tag{4.10}$$

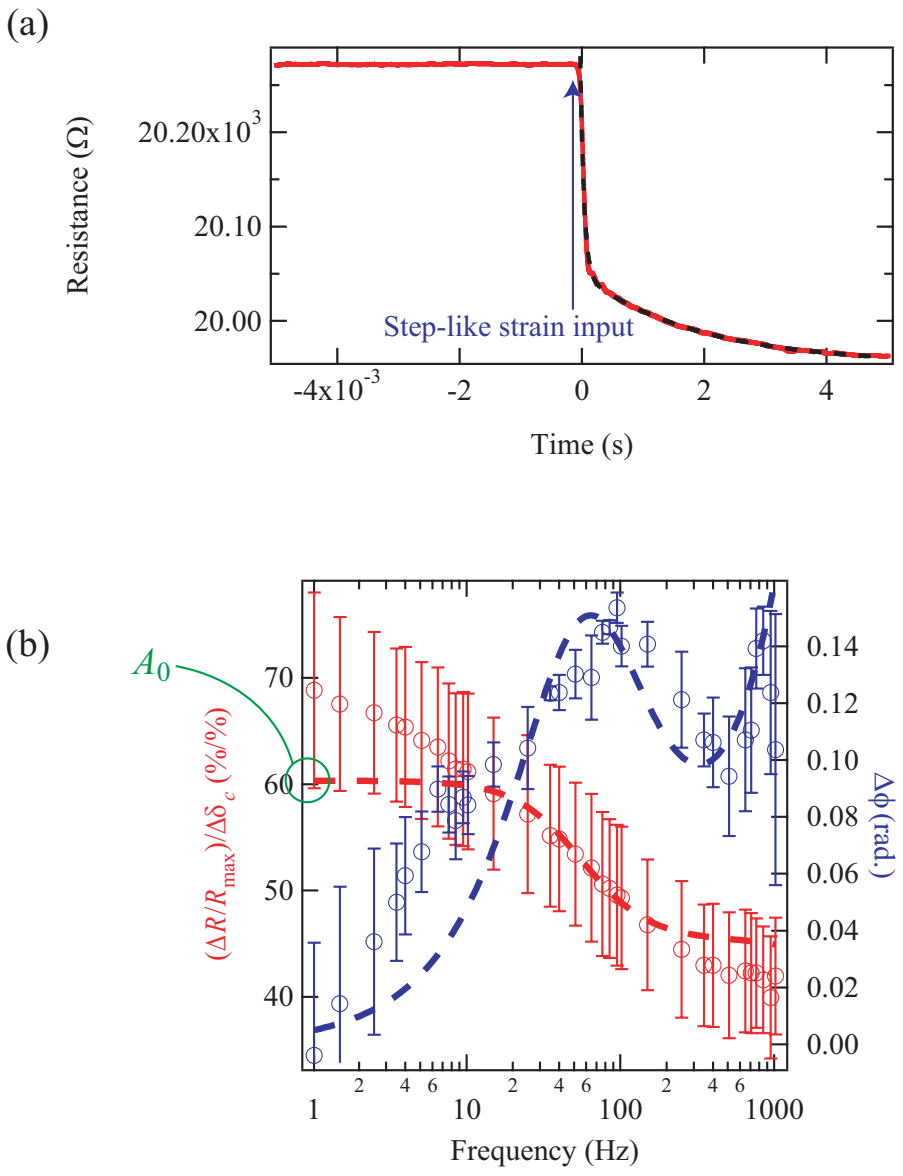

Figure 4.22: Function fitting to the time dependence (a) and the frequency dependence (b) assuming double exponential model. Fitting lines are shown with dotted lines. Fitting calculations are based on Eq. 4.7 (a) and on Eq. 4.9, 4.10, and 4.11 (b).

and it becomes possible to calculate the peak-to-peak resistance change under harmonic excitation as

$$\frac{(\Delta R/R_{\max})}{\Delta\delta_c} = A_0 f(\omega, \tau_1, \tau_2, \alpha), \tag{4.11}$$

where A_0 (%/%) is a dimensionless strain-resistance conversion ratio and ω is the measurement frequency.

It is reasonable to think that τ_1 and τ_2 are the time constants of domain nucleation and domain growth, respectively. Later discussion and data interpretation will concern the derived parameters A_0, which is a strain detection sensitivity, and τ_1, τ_2, which characterize the dynamics of the phase transition, and finally α which is a scaling factor describing the sensitivity of the phase transition to various internal mechanisms, (see Sections 4.4.3 and 4.4.4).

4.4.2 Performance validation of the high-frequency bending stage

It was demonstrated that the high-frequency crystal bending stage functions as expected, but it is still necessary to consider some potential pitfalls. The performance was therefore studied in additional detail.

Slip between Si heater and sample substrate

The sample substrate was attached to the Si heater element with thermally conducting paste. It is not immediately clear how such a sandwich structure would respond to mechanical strain. The sample could be rigidly attached to the Si heater, increasing the effective thickness of the substrate, or sideslip could occur in the in-plane direction. This is an important distinction, because the effective value of substrate thickness, t, is needed to calculate δ_c. There are thus two choices for the selection of t, either to regard the effective thickness as the thickness of the sample and the Si heater (rigid attachment), or as that of the substrate only. For determining which case is appropriate, two samples were prepared. For both samples VO_2 thin films were deposited on TiO_2 (001) substrates with the thickness of 0.2 mm and the standard deposition conditions: O_2 pressure 4.4 mTorr, thickness 10 nm, T_{sub} = 450 °C, and wire clamping. The only difference was the thickness of the Si heater, which was either 0.2 mm or 0.5 mm. At first, attachment of the heater to the substrate was observed under static strain, where the main effect is a shift of T_c, ΔT_c, with strain as shown in Fig. 4.23(a,b). As was shown with Eq. 4.5, the effective strain δ_c depends on thickness. The transition temperature shift is compared

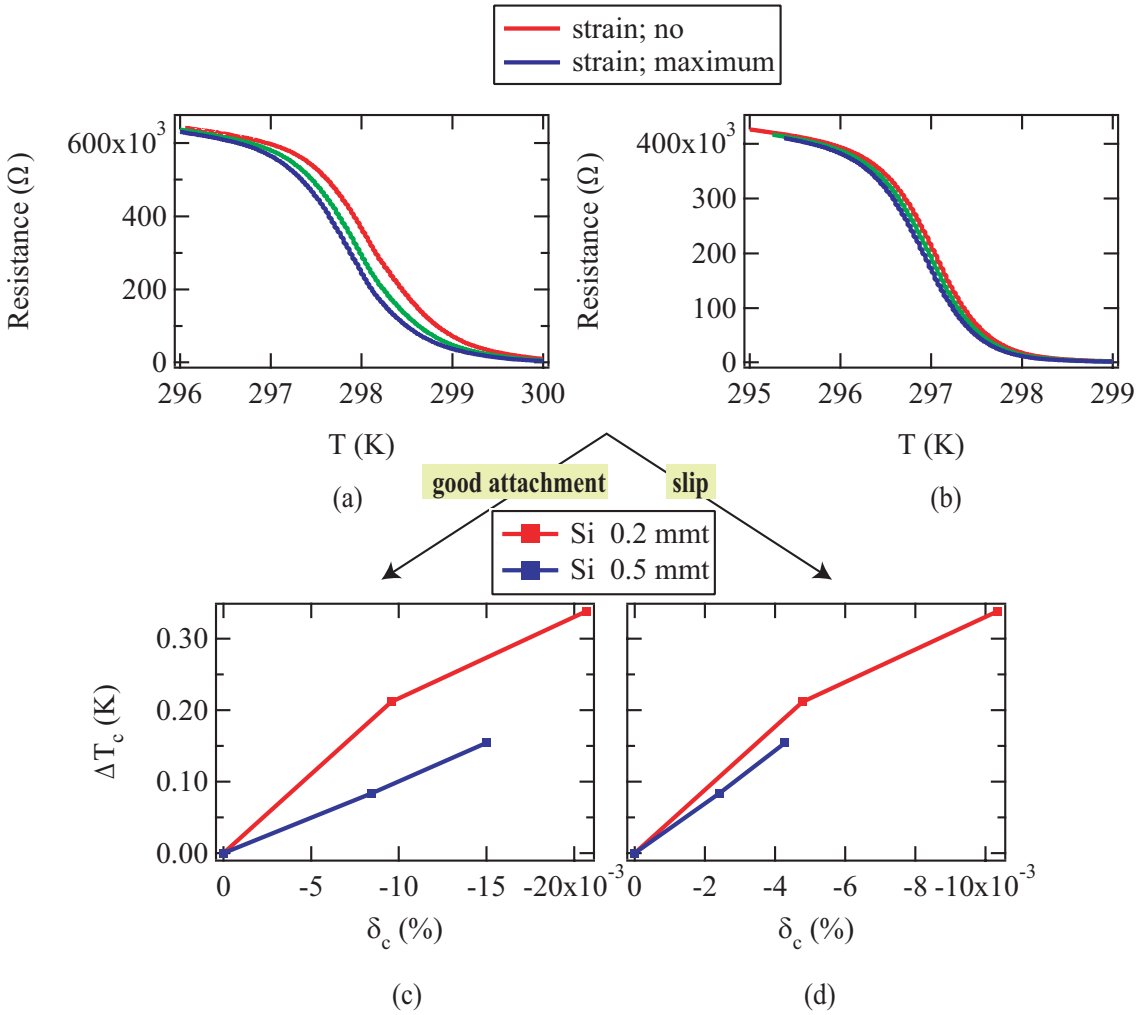

Figure 4.23: (a,b) Resistance of strained VO_2 thin films mounted on Si heaters with a thickness of 0.2 mm (a) or 0.5 mm (b). The transition temperature T_c is shifted toward lower temperature by strain. (c,d) The relation between T_c shift and the calculated δ_c, assuming rigid attachment between the Si heater and the sample substrate (c) or in-plane slip (d) under static strain.

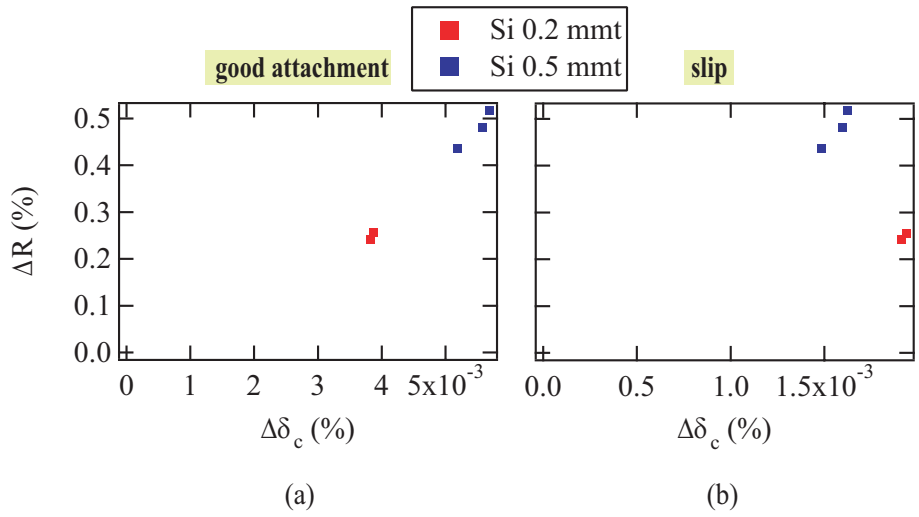

Figure 4.24: VO_2 thin film resistance change vs. δ_c calculated assuming rigid attachment between the Si heater and the sample substrate (a) or the presence of in-plane slip (b) under dynamic strain.

for assumed rigid attachment and in-plane slip in Fig. 4.23(c,d). As these two films should have the same δ_c dependence of ΔT_c, it is reasonable to assume that sideslip in the in-plane direction (Fig. 4.23(d)) does occur under static strain.

The previous comparison applied to static strain. In order to verify operation under dynamic strain, strain-induced resistance change was measured for the same sample sandwiches. The peak-to-peak resistance change and the δ_c calculated form the two assumptions (rigid or slip) are shown in Fig. 4.24. It is clear that under dynamic load, a linear relationship is observed assuming rigid attachment of the sample substrate to the Si heater (Fig. 4.24(a)). It appears that the heat-conducting paste can allow in-plane slip but only very slowly. In high-frequency measurements, rigid attachment can be assumed.

For dynamic load analysis in later sections 4.4.3 and 4.4.4, an effective thickness of t = 0.4 mm is used, which is the total thickness of both the substrate and the Si heater, both having a physical thickness of 0.2 mm.

Strain effect on thin films

The shift of the transition temperature, ΔT_c, was observed under both static and dynamic strain by bending the crystal. The observed temperature shift with strain should

be comparable to the T_c shift that has been observed in VO_2 films under epitaxial strain. For this purpose, the ratio $\frac{\Delta T_c}{\delta_c}$ was compared for both types of experiment. For bending data, $\frac{\Delta T_c}{\delta_c}$ = 32.4 K/%, while the published value for epitaxial strain is $\frac{\Delta T_c}{\delta_c}$ = 52.6 K/%.[1] These values are reasonably close, considering possible microstructure differences between films and it is safe to say that the high-frequency bending stage was successful in applying strain to a thin film sample.

Mechanical loss in high-frequency bending stage under dynamic strain

Any dynamic system is associated with dissipative processes. It is therefore necessary to think about internal friction (mechanical) loss that can generate heat in the sample in a high-frequency bending experiment. As in any forced oscillation system, there should be a characteristic frequency dependence of the amplitude and the phase delay. As a first step, the frequency dependence of the piezo actuator movement range was measured, as shown in Fig. 4.25. Since the wavefront analyzer cannot be used above 1 Hz, a different setup was used. Strain was observed by reflecting the laser beam from the sample surface and observing the spread of the beam as the sample was deformed. In this case, the distance between the sample surface and the screen was about 2.5 m. If there is a large frequency dependence of the piezo actuator movement range with frequency, it would be easily detectable as a shrinkage of the laser spot spread as the frequency is changed. However, no amplitude difference was observed, at least up to 1 kHz, which is the highest frequency used in bending experiments. It was concluded that any frequency dependence of the actuator range can be neglected.

The measurement system includes several amplifiers for driving the piezo actuator and detecting the sample resistance. Amplifiers generally have a frequency-dependent phase delay and this has to be considered in the experiment. For observing the frequency dependence of the mechanical phase delay, a photodiode was placed on the edge of the spread laser beam. Under these conditions, the photodiode is illuminated only when the sample deformation exceeds a certain value under harmonic drive. The photodiode current was measured through an I/V converter on a digital oscilloscope. First, the frequency-dependence of the phase delay of the photodiode, $\Delta\phi_{\text{diode}}$, was separately measured using an LED light source as in Fig. 4.26(a). Then, for measuring the phase delay from the piezo drive voltage to sample strain, the photodiode current was measured in the offset geometry as described earlier. The measurement setup

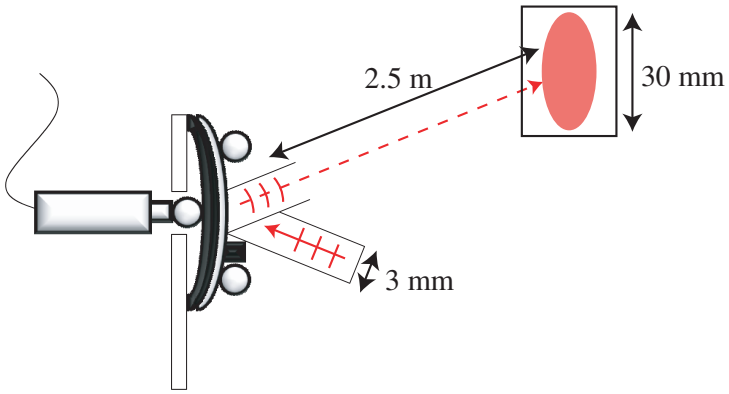

Figure 4.25: The measurement setup for measuring the frequency dependence of the dynamic strain amplitude. The width of the laser spot, 2.5 m from the sample surface expanding from 3 mm to 30 mm when the sample crystal was deformed.

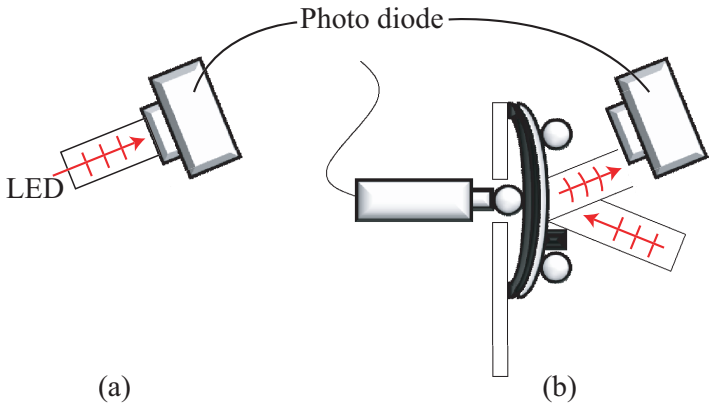

Figure 4.26: Measurement setup for determining the frequency dependence of the dynamic strain phase delay. (a) AC light input from a LED was measured with a photo diode. (b) AC strain input with piezo actuator was measured with a He-Ne laser and the same photodiode as in (a).

is illustrated in Fig. 4.26(b). this measurement gave the phase delay from the piezo voltage to the I/V converter output voltage, $\Delta\phi_{\text{sample}}$. The difference, $\Delta\phi_{\text{sample}} - \Delta\phi_{\text{diode}}$ is the intrinsic phase delay from the piezo voltage to the strain, attributed to all the electronic components, and the value varied from ~ 0.09 radian at 1 Hz to ~ 0.11 radian at 1 kHz. This phase offset was considered in analyzing the VO_2 deformation results in Sections 4.4.3 and 4.4.4.

Si heater effect on dynamic-strain-induced phase transition

By bending the crystal, it is possible for the attachment between the sample substrate and the Si heater to improve as pressure is applied. This can also affect the temperature of the sample due to an improved heat contact under pressure. This would be observed as an additional resistance drop in the VO_2 film. Because the temperature PID control was done with the temperature-sensing thermistor attached on the surface of the thin film sample, static strain experiment should not be affected by this effect, but dynamic strain measurements could be affected because the PID control cannot follow fast temperature change. For measuring the Si heater effect, sample resistance change was observed under step-like strain input with two ways of temperature control. In one case, the usual Si heater was used, while in another measurement an external heat gun was used, as shown in Fig. 4.27. In the latter case, the resistance (or temperature) of the sample would not be affected by heat transfer changes between the sample and the Si heater under pressure. As shown in Fig. 4.27, the stepwise strain response curves overlap exactly, showing that heat transfer from the Si heater does not change significantly under load.

It is possible for a VO_2 film to be heated by cyclic phase transitions, i.e. effective internal friction in the film due to cyclic loading. If so, the only role of the dynamic stress would be to provide thermal energy. If this assumption were true, it would be impossible to explain the resistance behavior in Fig. 4.28. This data was measured under a step-like strain input of the actuator release. If temperature would cause the phase transition, this resistance change would come from a temperature drop. Dynamic stress cannot remove energy from the sample, so the assumption that losses related to the structural phase transition brings heat into the film can be ignored.

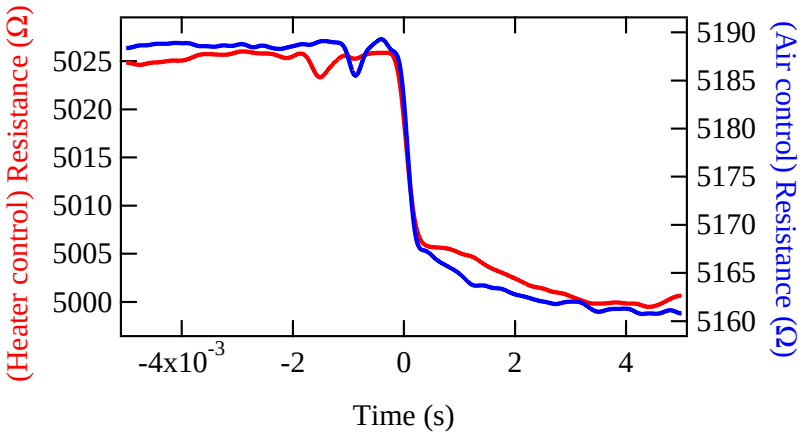

Figure 4.27: Resistance change with step-like strain input by controlling temperature with a Si heater (left axis, red line) or with an external heat gun (right axis, blue line).

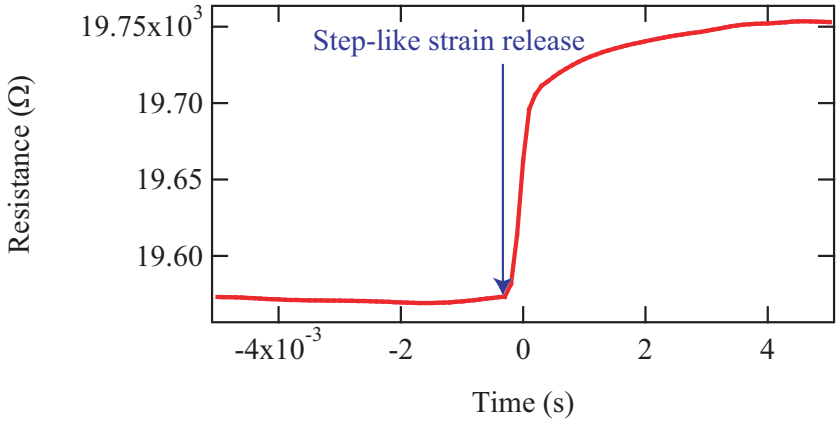

Figure 4.28: Resistance change with stepwise strain release. If a related temperature change would cause the phase transition, this resistance change would have to come from a temperature drop.

4.4.3 Sample dependence of strain-related properties

Various samples with possibly different grain structures were studied in this work. Some of the data was shown in Figs. 4.12 and 4.15. The main interest from the point of view of using VO_2 as a strain sensor is to look at the variation of the dimensionless strain-resistance conversion ratio A_0 (%/%) (see Eq. 4.11). The results for some typical VO_2 thin films at each transition point are shown in Fig. 4.29. A large difference in strain response can be seen in different films. Though there is some difference of grain diameters, *c*-axis lattice parameters, and T_c, sensitive probes of domain size distribution in the film and thus the strain-resistance conversion ratio A_0, are TCR, $\frac{\Delta R_{tem}}{\Delta T}\frac{1}{R}$ close to T_c and the hysteresis width, ΔT_{hys}

$$A_0 = C_1 \exp\left(-\frac{k\Delta T_{hys}}{k_B T_c}\right) T_c \left.\frac{\Delta R_{tem}}{\Delta T}\frac{1}{R}\right|_{T=T_c}, \tag{4.12}$$

where k is a parameter that relates ΔT_{hys} to the height of the energy barrier separating the metallic and insulating crystallographic phases and C_1 is an amplification factor that scales the effect of strain relative to temperature on the resistance of the film. This can be seen by considering that based on Eqs. 4.11 and 4.12, strain-related resistance

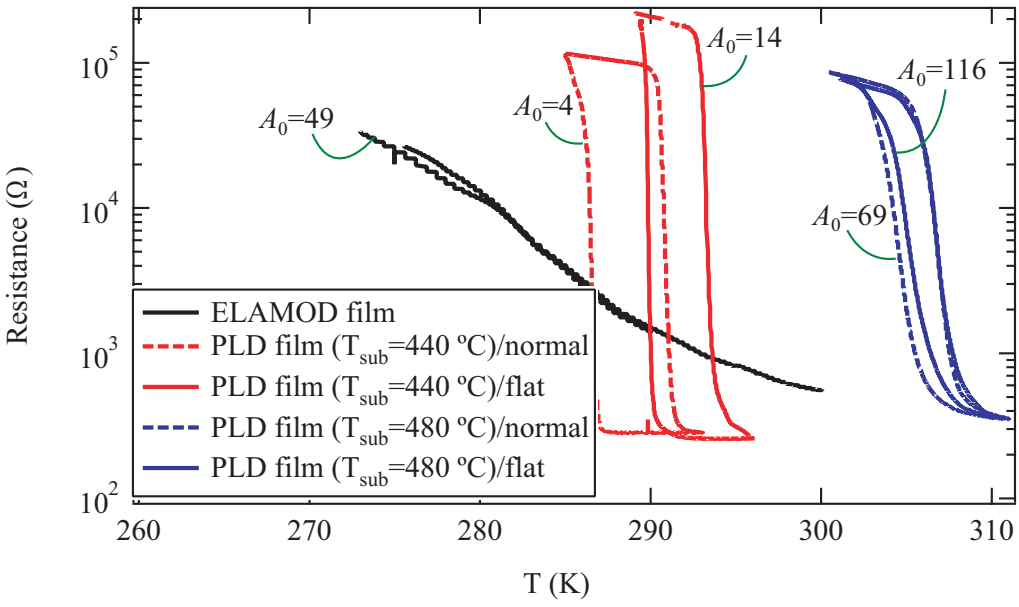

Figure 4.29: Resistance of various VO_2 films deposited under different conditions (shown in Fig. 4.12) and for each film, the corresponding value of A_0 (see Eq. 4.11) is shown.

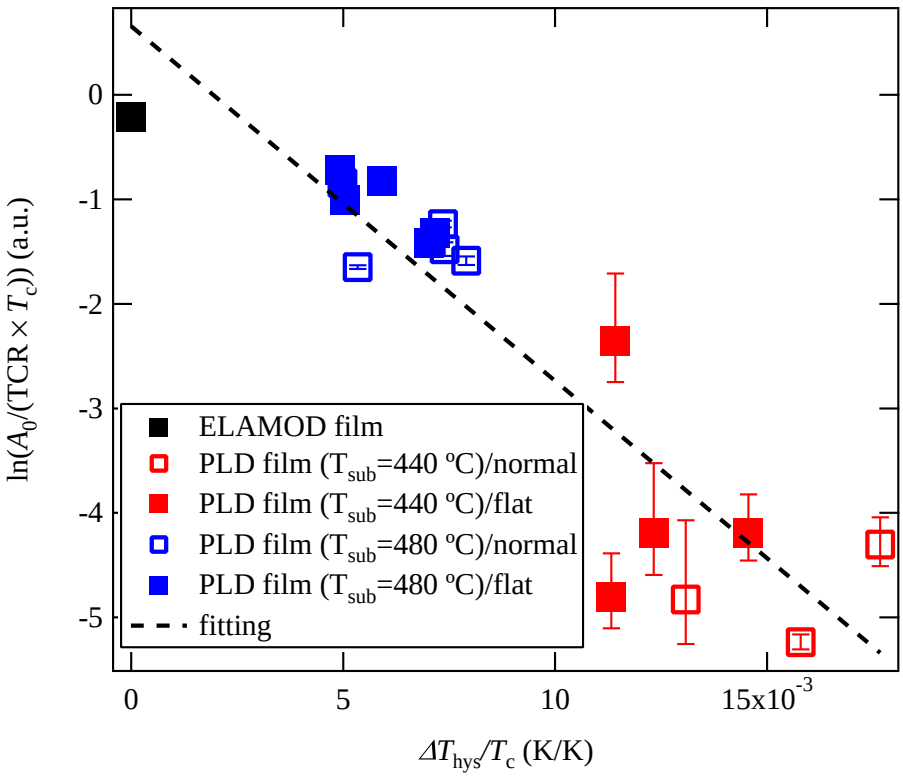

Figure 4.30: Relation between A_0 and sample transition behavior. The fitting line is based on Eq. 4.12, and resulted in k = 0.030 eV/K (=340k_B), and C_1 = 1.9.

change can be estimated as

$$\frac{\Delta R}{\Delta \delta_c} = nC_1 \frac{\Delta R_{\text{tem}}}{\Delta T/T_c}, \tag{4.13}$$

where n=1 if $\Delta T_{\text{hys}} = \omega = 0$. What the mechanism in Eq. 4.12 is can be thought of as follows. A_0 can be expressed as $N_{\text{PT}} \times P_{\text{PT}}|_{T=T_c}$, where N_{PT} is the ratio of domain switching at the transition point (TCR becomes broad because domains or grains can have different T_c), and P_{PT} is each domain's or grain's probability of switching. Therefore, N_{PT} and P_{PT} can be translated into TCR, $\frac{\Delta R_{\text{tem}}}{\Delta T}\frac{1}{R}$ close to T_c and $\exp\left(-\frac{k\Delta T_{\text{hys}}}{k_B T_c}\right)$ relating to the hysteresis width, respectively. Based on Eq. 4.12, it is possible to estimate parameters C_1 and k by fitting the data in Fig. 4.30, where results from 18 samples have been plotted together. In this case, a linear fit resulted in k = 0.030 eV/K (=340k_B), and C_1 = 1.9. Close to the transition temperature, a VO_2 film contains both metallic and insulating domains. A large hysteresis is an indication that the two phases are

separated by an energy barrier. The height of this barrier cannot be determined by a simple Arrhenius analysis of resistivity because the temperature is fixed at T_c. The relative stability of the two phases can, however, be changed by lattice strain at a fixed temperature and measured by a change of film resistance. In this case, the results show that the activation energy height scales with the hysteresis width, $E_a = 0.03\Delta T_{hys}$ eV (for VO_2, $E_a \sim 0 - 1.5$ eV). Although both temperature and strain have similar effects on the electronic phase of VO_2, i.e. an increase of temperature is equivalent to compressive strain, the pre-factor C_1 value of 1.9 appears to show that as a driving force for the phase transition in VO_2, lattice parameter change dominates over a purely electronic reconstruction.

4.4.4 Temperature dependence of domain dynamics

The temperature dependence of domain dynamics was studied by looking at the temperature dependence of A_0, τ_1, τ_2, and α. The sample measured was a VO_2 thin film grown at $T_{sub} = 480$ °C on a normal substrate. The film thickness was 12.5 nm. Resistance data for this film was shown in Fig. 4.15(c). The strain-resistance conversion ratio, A_0 was measured at several resistances around the transition point as in Fig. 4.31. As shown in the Figure, A_0 reaches a maximum close to the transition point. This indicates that the temperature-induced phase transition point is very close to (or the same as) the strain-induced phase transition point.

The temperature dependence of the time scale of domain switching can be discussed in terms of τ_1, τ_2, and α. These three parameters can be obtained in two ways, either from the time dependence data, as in Fig. 4.22(a) or indirectly from the frequency dependence as in Fig. 4.22(b). The results are shown in Fig. 4.32. It should be noted that a stepwise piezo voltage does not mean that strain follows a perfect step function for various extrinsic mechanical reasons. Due to that, data from the frequency dependence is more reliable. However, nearly the same values for the three parameters were derived from the time- and frequency-domain analyses. This indicate that the analysis method is robust and reflects the true intrinsic material properties. Fig. 4.32 will be discussed in details in the following.

Although it is clear that at least two relaxation time constants are needed to fit the data in Fig. 4.22(b), interpretation of these two relaxation times is not automatically clear. The assumption is that τ_1 and τ_2 are constants corresponding to domain nucleation (fast) and domain growth (slow), respectively. But is this interpretation reasonable? For verifying this assumption, the VO_2 thin film surface was observed with

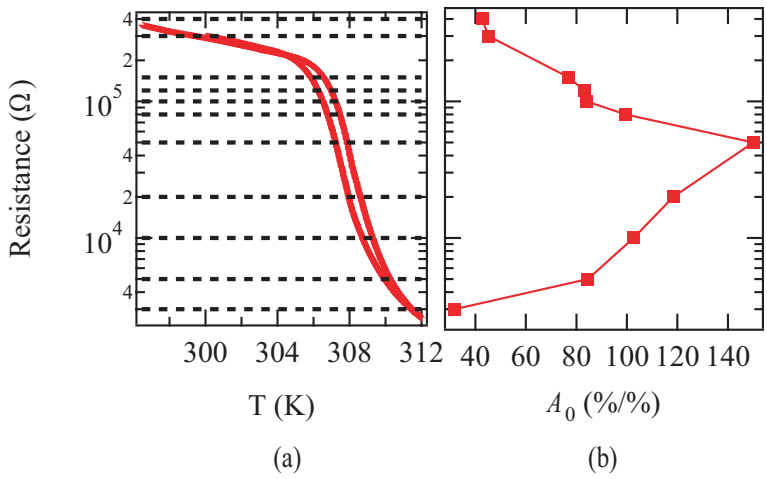

Figure 4.31: (a) Resistance vs. temperature data of a VO_2 thin film grown at T_{sub} =440 °C with a thickness of 12.5 nm. (b) Measured resistance dependence of the A_0 value. Each resistance is shown in (a) as a dotted line.

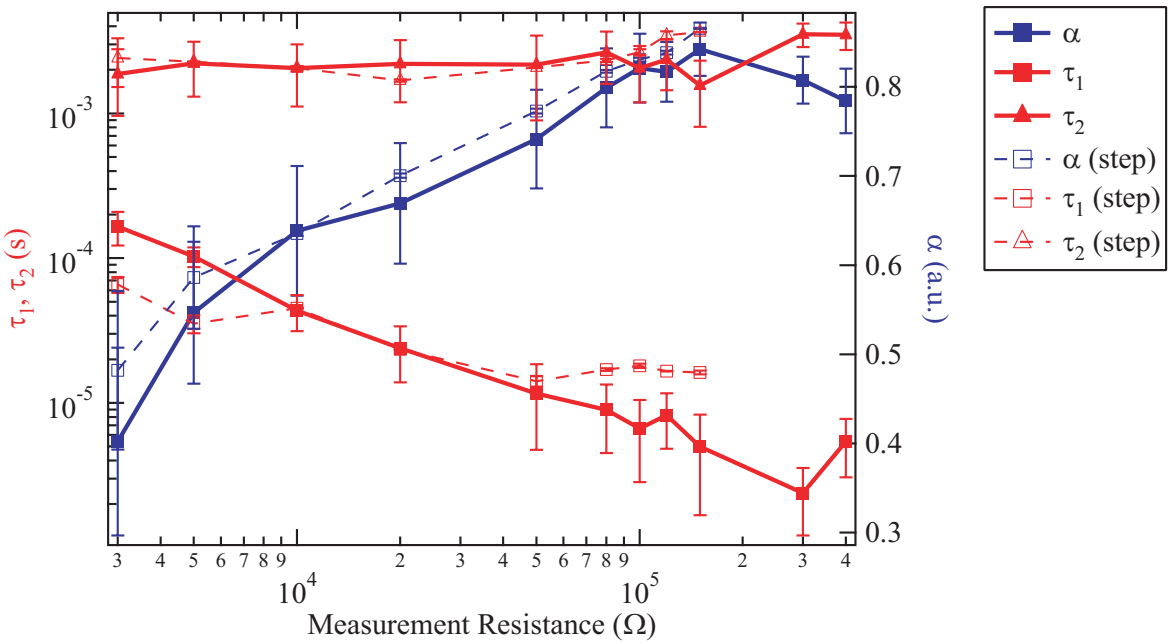

Figure 4.32: Measurement resistance (temperature) dependence of α, τ_1, and τ_2 values. Dotted line data set is calculated from the time dependence in Fig. 4.22(a). Solid line data set is from the frequency dependence in Fig. 4.22(b). Each resistance is shown in Fig. 4.31(a) as a dotted line.

conducting tip AFM, as shown in Fig. 4.33. This measurement gives information about the local nanometer scale distribution of coexisting metallic and insulating domains. In this case, the sample was a VO_2 thin film deposited on a conducting Nb:TiO_2 (001) substrate. The deposition conditions were nearly the same as those used in Fig. 4.32. The insulating domains (blue) dominate the system at low temperature while metallic domains (red) dominate at high temperature. The area for each domain type can be calculated by standard image particle analysis. The domain ratios obtained from the AFM data can be used to derive temperature-dependent domain growth and domain switching contributions to the resistance transition in a thin film sample. The results are shown in Table 4.1. However, the analysis is limited to temperatures below 306.2 K (Fig. 4.33(e)) because at higher temperatures, individual metallic domains are joined

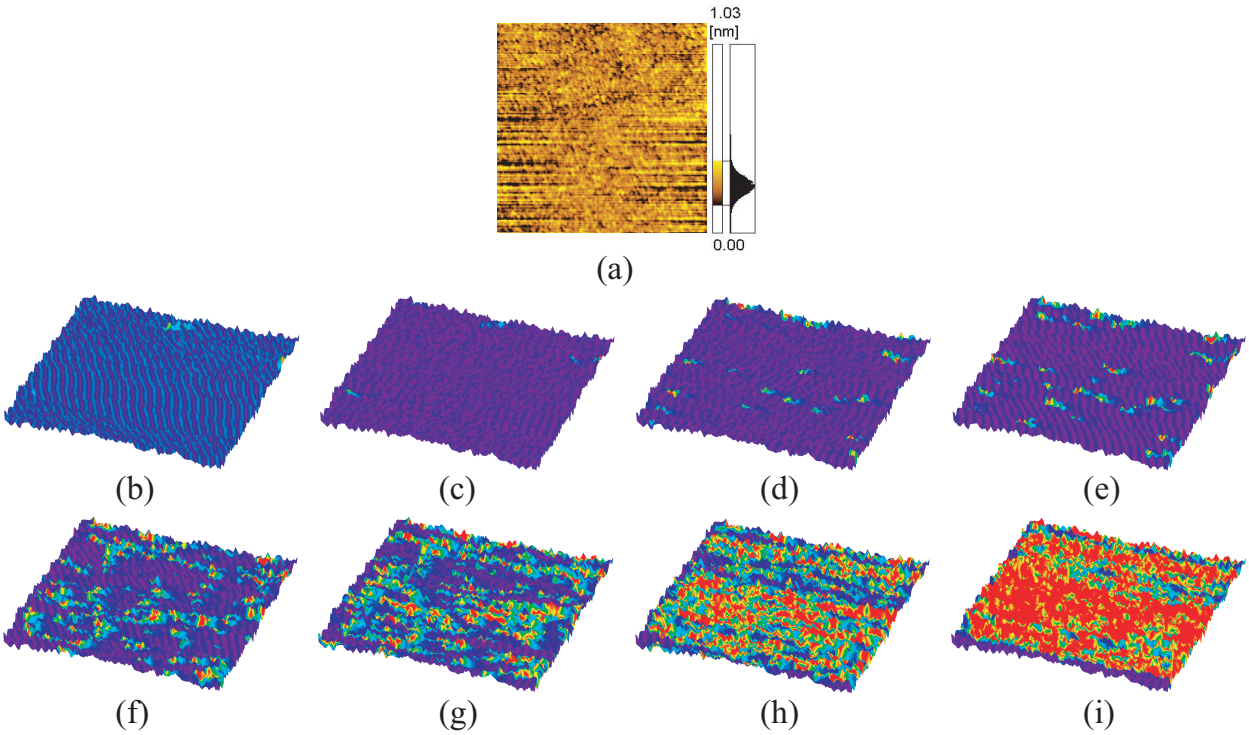

Figure 4.33: Data set of conducting tip AFM current density images (1×1 μm^2). (a) VO_2 thin film surface topography for a sample deposited on Nb:TiO_2 (001) substrate measured with conductive AFM. (b-i) VO_2 thin film current maps at the temperature of 303.5 K (b), 304.8 K (c), 305.9 K (d), 306.2 K (e), 306.4 K (f), 306.6 K (g), 306.8 K (h), and 307.0 K (i). The images were taken while cooling from 307.0 K to 303.5 K. Metallic regions are shown in red while insulating parts are blue.

Table 4.1: Areas of domain growth and switching between (b) and (c), (c) and (d), (d) and (e) in Fig. 4.33. Calculated switching ratios are also shown. These values can be associated with α (see Eq. 4.7).

	(b)⇔(c)	(c)⇔(d)	(d)⇔(e) in Fig. 4.33
Domain growth, S_{growth} (μm^2)	0.0013	0.0078	0.019
Domain switching, S_{switch} (μm^2)	0.0034	0.029	0.02
Switching ratio, $S_{\text{switch}}/\left(S_{\text{growth}} + S_{\text{switch}}\right)$	0.72	0.79	0.51

Domain size (μm²)	*N*
-0.0002	4
0.0002-0.0003	3
0.0003-0.0004	1
0.0004-0.0005	0
0.0005-0.0006	7
0.0006-0.0007	2
0.0007-0.0008	3
0.0008-0.0009	0
0.0009-	53

(a)

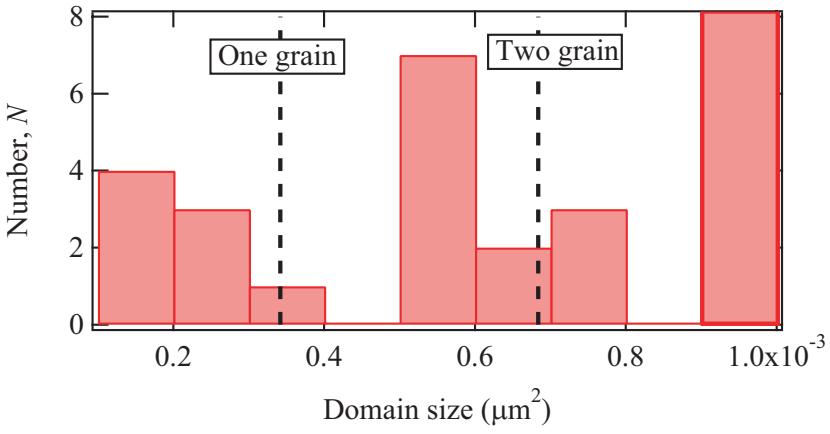

(b)

Figure 4.34: Histograms of domain size distribution as a table (a) and graph (b), showing metallic domain sizes for the VO_2 thin film for which AFM data is shown in Fig. 4.33(b-e). The average grain size is 0.000342 μm^2 (shown in (b)). Domain sizes form peaks at integer multiples of grain size.

and it is difficult to determine growth and nucleation independently. Assuming that the calculated switching ratios can be associated with α (see Eq. 4.7), and considering that α is $\sim$ 0.7-0.8 at low temperatures and $\sim$ 0.5 at high temperature (Fig. 4.32), it is obvious that the data obtained from dynamic measurements corresponds quite well to the numbers derived from the conductive AFM data (Table 4.1). This shows that the assumption that τ_1 and τ_2 correspond to domain nucleation and domain growth is reasonable.

The AFM data in Fig. 4.33 shows that the grain boundaries in the film appear to restrict the domain size growth. The grain sizes in Fig. 4.33(a) and metallic domain sizes in Figs. 4.33(b-e) were calculated. The resulting histograms are shown in Fig. 4.34. The metallic domain sizes seem to be integer multiples of the grain size. This shows that the domain size is limited by the grain boundaries.

From Fig. 4.32, it can be concluded that the time constant of domain growth (τ_2) is nearly constant ($\sim$ 2-3 ms) over the whole measurement temperature range. This indicates that domain growth is mainly affected by thermal energy, $k_B T$, which is almost constant within the data set, since measurements only have a meaning close to the transition temperature. On the other hand, the time constant of domain nucleation (τ_1) is increasing with measurement temperature. It follows that the system is nucleation limited at lower temperature, and both nucleation and growth limited at higher temperature. Then, why is τ_1 larger at higher temperature? It is possible that domain nucleation is mainly affected by the energy barrier between metallic and insulating phases, unlike the domain growth mechanism. If so, the data in Fig. 4.32 indicates that the height of the energy barrier is larger at higher temperature. This result is supported by Vikhnin et al.,[17] who calculated the height of the energy barrier in VO_2, shown in Fig. 4.35. They calculated it with respect to charge transfer order parameter, q for the tetragonal symmetry (i.e. q is bigger in the metallic phase), and therefore they concluded that the energy barrier is higher at higher temperature.

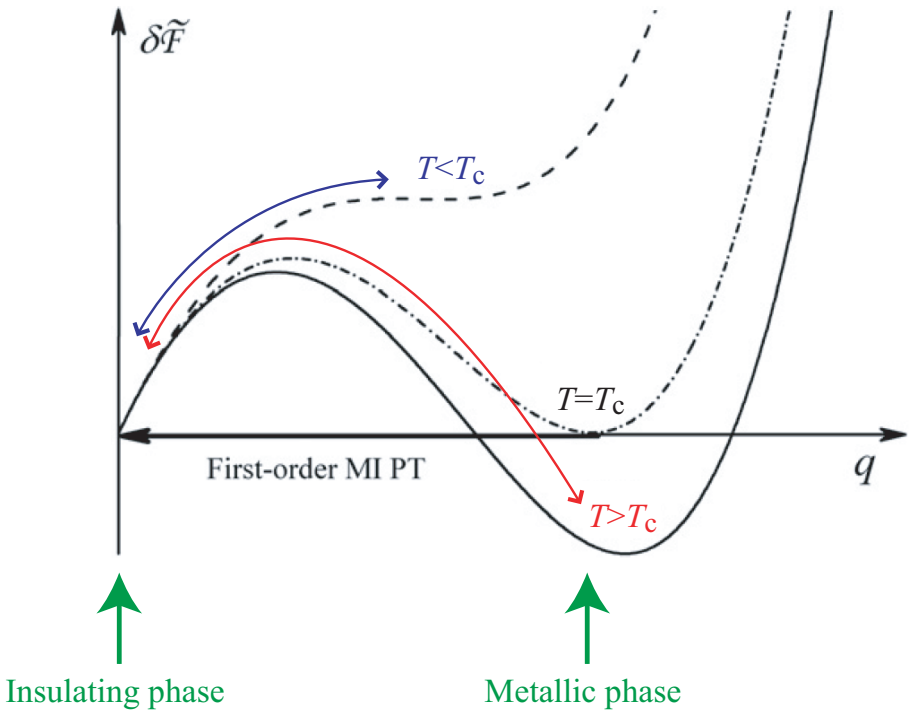

Figure 4.35: Free energy profiles for three temperature values calculated by Vikhnin et al.[17] Higher and lower temperature states than the transition point result in nonsymmetric profiles. The energy gap is higher at $T > T_c$ than at $T < T_c$.

4.5 Conclusion

A high-frequency crystal bending stage was constructed and used to measure the strain response in VO_2 thin films. The instrument worked as planned, and it was possible to observe a dynamic-strain-induced phase transition. The maximum value of amplification from strain to resistance, A_0 was 157 in the best VO_2 film, while it is 4 in usual metal strain gauges. This shows that VO_2 is a potentially useful material for strain sensing. The activation energy, $k\Delta T_{\mathrm{hys}}$, for the dynamic-strain-induced metal-to-insulator transition was measured, giving $k = 0.030$ eV/K. Close to T_c, the effect of strain on resistance is larger than a pure thermal change by a factor of nearly 2 ($C_1 = 1.9$). The temperature dependence of amplification, A_0 indicates that it is the largest at around the transition point. The data includes two time constants, corresponding to a domain nucleation process ($\tau_1 \sim 10^{-5}$ s) and a domain growth process ($\tau_1 \sim 10^{-3}$ s). It was found that τ_1 is increasing with temperature because the energy barrier height separating the metallic and insulating phases becomes larger at higher temperatures, while τ_2 is constant and is mainly given by thermal energy.

References

[1]Y. Muraoka, Y. Ueda, and Z. Hiroi, J. Phys. Chem. Solids **63**, 965 (2002).

[2]S. L. Bud'ko and J. Guimpel, O. Nakamura, M. B. Maple, and I. K. Schuller, Phys. Rev. B **46**, 1257 (1992).

[3]W. Chang, J. M. Pond, S. W. Kirchoefer, and J. A. Bellotti, Appl. Phys. Lett. **87**, 242904 (2005).

[4]A. Herklotz, A. D. Rata, L. Schultz, and K. Dörr, Phys. Rev. B **79**, 092409 (2009).

[5]M. K. Lee, T. K. Nath, C. B. Eom, M. C. Smoak, and F. Tsui, Appl. Phys. Lett. **77**, 3547 (2000).

[6]L. Pellegrino, M. Biasotti, E. Bellingeri, C. Bernini, A. S. Siri, and D. Marré, Adv. Mat. **21**, 23 (2009).

[7]J. Wei, Z. Wang, W. Chen, and D. H. Cobden, Nature Nanotechnology **4**, 420 (2009).

[8]C. E. Campos, J. S. Brooks, P. J. M. van Bentum, J. A. A. J. Perenboom, S. J. Klepper, P. S. Sandhu, S. Valfells, Y. Tanaka, T. Kinoshita, N. Kinoshita, M. Tokumoto, and H. Anzai, Phys. Rev. B **52**, R7014 (1995).

[9]S. Arumugam, K. Mydeen, N. Manivannan, M. Kumaresa Vanji, D. Prabhakaran, A. T. Boothroyd, R. K. Sharma, and P. Mandal, Phys. Rev. B **73**, 212412 (2006).

[10]K. Nagashima, T. Yanagida, H. Tanaka, and T. Kawai, Phys. Rev. B **74**, 172106 (2006).

[11]N. Sepúlveda, A. Rúa, R. Cabrera, and F. Fernández, Appl. Phys. Lett. **92**, 191913 (2008).

[12]P. A. Bakut, V. E. Kirakosyants, C. J. Solomon, J. C. Dainty, and V. A. Loginov, Optics Communications **109**, 10 (1994).

[13]Y. Yamamoto, K. Nakajima, T. Ohsawa, Y. Matsumoto, and H. Koinuma, JJAP **44**, L511 (2005).

[14]C. H. Griffiths, and H. K. Eastwood, J. Appl. Phys. **45**, 2201 (1974).

[15]V. A. Klimov, I. O. Timofeeva, S. D. Khanin, E. B. Shadrin, A. V. Ilinskii, and F. Silva-Andrade, Tech. Phys. **47**, 9 (2002).

[16]V. S. Vikhnin, S. Lysenko, A. Rua, F. Fernandez, and H. Liu, Phys. Lett. A **343**, 446 (2005).

[17]V. S. Vikhnin, S. Lysenko, A. Rua, F. Fernandez, and H. Liu, Optical Materials **29**, 1385 (2007).

Chapter 5

Magnetostrictive field sensor

5.1 Introduction

Various types of magnetic field sensors are widely used in many fields of life. One recent trend has been to develop highly sensitive magnetic field sensors that can operate at close to room temperature but offer similar sensitivity as a SQUID sensor can provide at low temperature. Potential areas of use would be in the fields of non-destructive testing and medical mapping of magnetocardiograms and possibly magnetoencephalograms. One possibility is to combine magnetoelastic elements, i.e. materials that change shape or dimensions in a magnetic field, with materials that can provide a charge or resistance change upon change of size. An example is a macroscopic composite of a magnetostrictive TERFENOL-D ($Tb_{1-x}Dy_xFe_{2-y}$) alloy and a piezoelectric single crystals, such as $Pb(Zr_{1-x},Ti_x)O_3$.[1–4] They focused attention on the fact that piezoelectric/magnetostrictive composites have better magnetoelectric (ME) properties[5–7] than single crystals.[8,9] Finally, they have made sensors detecting even pico-Tesla magnetic field at room temperature.[4]

In the published composite field sensors, the attachment between the magnetostrictive and piezoelectric materials has been done by simple epoxy glue. The aim in this work was to explore the possibility of fabricating an epitaxial sensor based on two improvements. Strain can be much more efficiently mediated in an epitaxial heterostructure than in a polymer-based sandwich. Secondly, instead of using a linear piezoelectric effect, it may be possible to use the highly nonlinear behavior of a phase transition and thus improve on the sensitivity of detecting strain.

Based on these ideas, and the work done on strain effects in VO_2, the feasibility of combining a magnetostrictive oxide, Fe_3O_4, with VO_2 was studied. The hope was that

the strain-induced phase transition in VO_2 thin film, discussed in Chapter 4, would offer a larger resistive response than a piezoelectric crystal. In order to test this idea, VO_2 thin films grown on Fe_3O_4 (111) substrate were used. The thin film fabrication details are presented in Section 5.3. For measuring the sensor response in an alternating magnetic field, a rotating magnetic field stage was constructed. This instrument was used to observe the resistance change in a Fe_3O_4 / VO_2 heterostructure while permanent magnets were spinning around a sample.

5.2 Magnet rotation stage

The design of the rotating magnetic field measurement system is shown in Fig. 5.1. An aluminum frame was used to hold a stepping motor and two permanent Nd-alloy magnets ($87 \times 42 \times 6.6$ mm^3). The magnets are much larger than the sample area and can thus provide a homogeneous magnetic field in the center of the device. The strength of the magnetic field is tunable by changing the distance between the two magnets in the range from 6 to 58 mm. Even at the largest magnet spacing, the small stepping motor (PK543AN, driver: CSD5807N-P, Oriental Motor Co., Ltd.) could rotate the stage at up to 3 Hz. For smaller spacings, much higher rotation rates were possible. The sample, in this case a thin film grown on a substrate, was attached to a doped Si substrate with thermally conducting glue. The Si heater, together with a thermistor sensor, were used for temperature control of the sample. Rotating the magnets alters the direction of the magnetic field, but it can also cause an air flow around the sample, making accurate temperature control impossible. To avoid this problem, a straw cover was placed around the sample.

The concept of how strain can be induced by a magnetic field is shown in Fig. 5.2. If a magnetic field is applied to a magnetostrictive substrate, the shape of the crystal changes, in both in-plane and out-of-plane directions. A film grown on the substrate would be strained accordingly. An in-plane change of the substrate lattice parameter is directly transferred to the film. This deformation translates also into an out-of-plane strain in the film. Whether the strain is compressive or tensile depends on the magnetostrictive material, crystal orientation, and the external field orientation. Considering the crystal orientations used in this work, it was possible to apply a VO_2 c-axis strain, δ_c of up to about 0.002 %.

The magnetic field value at the sample position was measured by replacing a sample holder with a single-loop coil. As the area of the coil was known (S = 160 mm^2) and

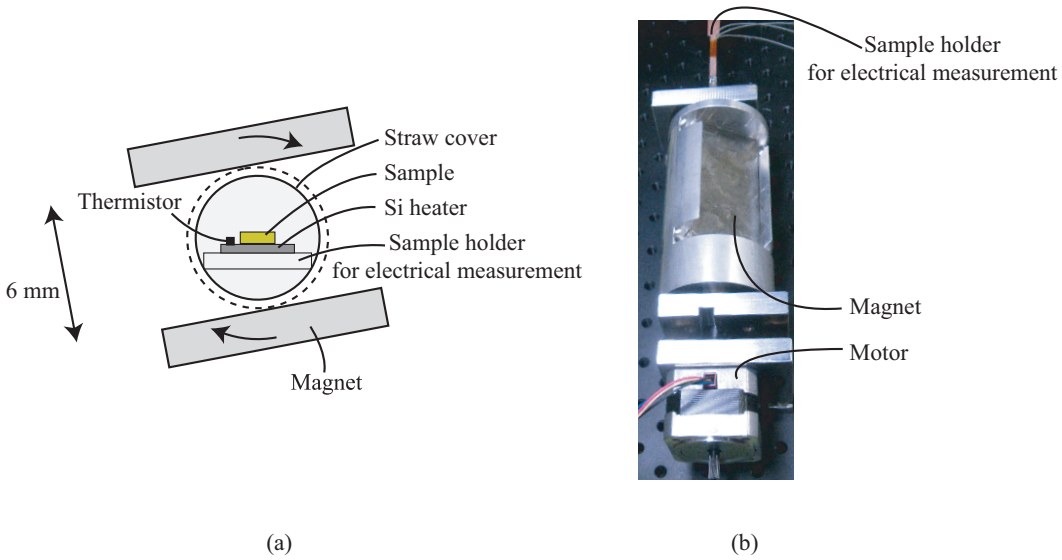

Figure 5.1: A sketch (a) and photo (b) of the magnetic field rotation stage.

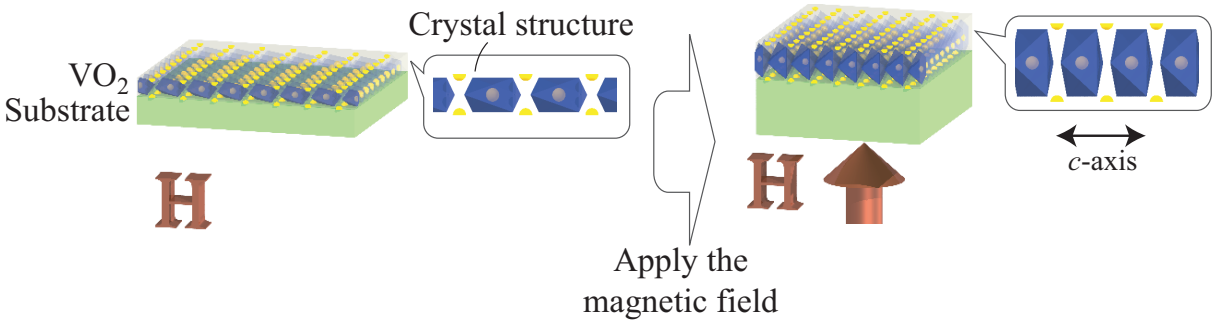

Figure 5.2: The effect of an external magnetic field on the strain of a film grown on a magnetostrictive substrate. VO_2 *c*-axis is presented in this figure, but pay attention to the fact that this direction includes ambiguity.

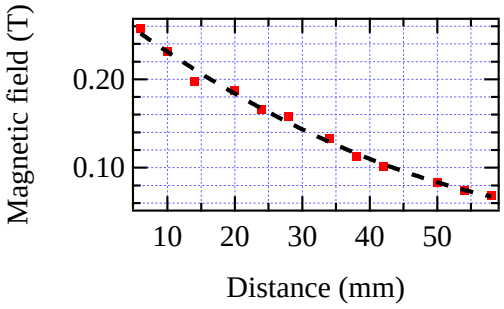

Figure 5.3: The magnetic field dependence on the magnet distance. The magnetic field range is $\sim 0.07 - 0.26$ T.

the magnetic field was sufficiently homogeneous (based on finite element method field profile simulations), it was possible to calculate the magnetic field value, B using Faraday's law of induction

$$V = -\frac{\mathrm{d}(BS)}{\mathrm{d}t}, \tag{5.1}$$

where V is the magnitude of the electromotive force in volts. The applied B function was harmonic in the range of 3 to 8 Hz. The experimental result is shown in Fig. 5.3, where the measured field strength is plotted as a function of the distance between the two magnets with the dotted line being just a guide for the eye. From this experiment, it was found that the field can be varied between $\sim 0.07 - 0.26$ T. These values were also calibrated against a commercial Hall field sensor. Since the maximum field strength was sufficient to saturate the magnetization of the Fe_3O_4 substrate, there was no need to construct a flux return armature around the magnets, making it easier to change the magnet spacing.

The sample holder is shown in Fig. 5.4. Transport properties of the film were measured during rotation by attaching flexible wire probes to the sample surface by ultrasonic wire bonding. The sample holder has a role of controlling the sample temperature. For this purpose, a silicon heater was mounted under the sample crystal and a thermistor was attached to the heater for temperature feedback. PID temperature control was done by an external computer running a LabVIEW program. A single connector was used to attach all the measurement and temperature control electronics to the sample holder.

The sample resistance response was monitored on a digital oscilloscope. The resistance change of a VO_2 film can be quite small during magnet rotation, but still large

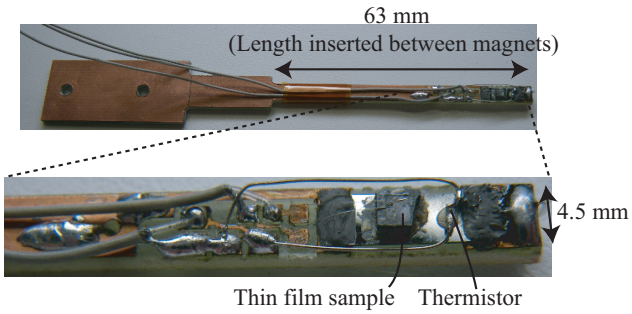

Figure 5.4: The sample holder used for electrical measurement in the magnet rotation stage.

enough to detect without resorting to lock-in detection. Typical relative resistance change in measurements was less than 0.2 %. It was therefore necessary to construct a suitable electronic setup, similar to the high-frequency bending stage in Fig. 4.6(a). Again, an I/V converter was used to convert a current change into a voltage signal that could be observed on the oscilloscope (see Fig. 4.6(b)).

The calculation method for estimating the actual sample deformation will be discussed in Section 5.4.1.

5.3 Fabrication of VO_2 thin films on a Fe_3O_4 substrate

The VO_2 thin films were fabricated on a Fe_3O_4 (111) substrate obtained from Surface Preparation Laboratory. At first, the magnetization behavior of the substrate crystal in an external magnetic field was measured. The magnetization curve is shown in Fig. 5.5. Since the quality of commercial Fe_3O_4 substrate crystals may vary, it was necessary to measure the actual curve instead of relying on published data. It was found that the magnetization behavior was close to the single crystal data reported in the literature.[10,11] It is clear that the 250 mT maximum field of the rotation stage is large enough to saturate the substrate magnetization.

As Fe_3O_4 is conductive, it seemed at first that it would be necessary to isolate the VO_2 film from the substrate. An attempt was therefore made to buffer the substrate with a non-doped TiO_2 film. However, it was found that the leak levels in nm-order TiO_2 films were too high to provide adequate insulation, whereas thick TiO_2 films would have reduced strain coupling between the substrate and the VO_2 film. These experiments showed that it is possible to measure the VO_2 resistance change at the transition point

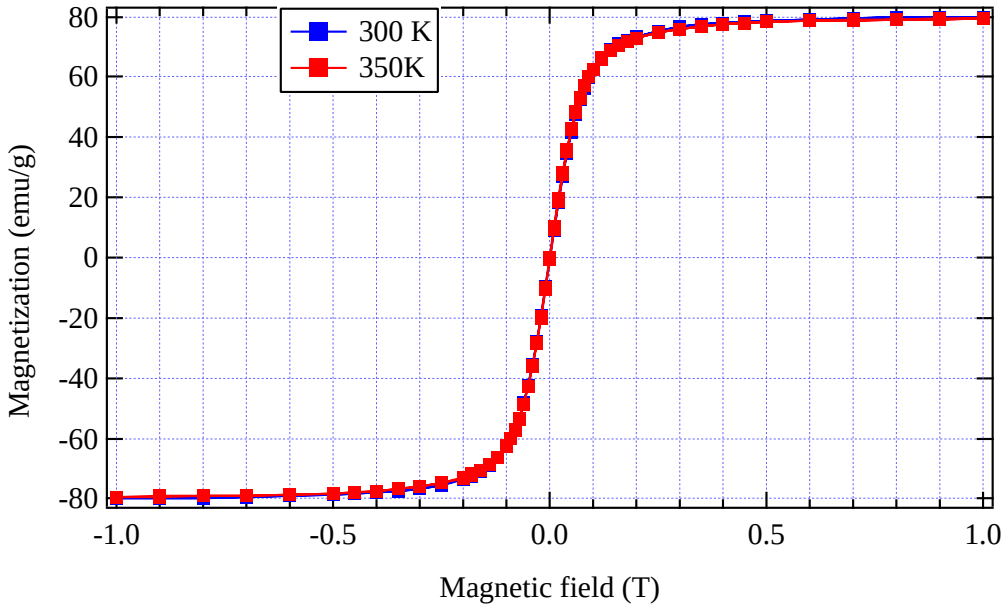

Figure 5.5: Magnetization vs. magnetic field of a Fe_3O_4 substrate.

in an out-of-plane geometry, similar to the conducting-tip AFM studies. In such a measurement, resistance is measured in a 2-point geometry between the film surface and the conducting substrate. VO_2 films could therefore be grown directly on the surface of the conductive Fe_3O_4 substrate.

The deposition conditions were the following. A single Fe_3O_4 (111) substrate ($2.5 \times 2.5 \times 0.65$ mm^3) was used. For deposition, the laser fluence was 560 mJ/cm^2 at an ablation spot size of 0.06 cm^2. The laser pulse rate was 1 Hz, giving a growth rate of ~0.005 nm/pulse. It was found that the V_2O_3 target surface is unstable in UHV conditions. The target surface was therefore prepared by performing a pre-ablation of 10000 pulse at 10 Hz before deposition. Film growth optimizations, illustrated in Fig. 4.10, resulted in a choice of 4.4 mTorr O_2 pressure for deposition. The growth temperature, T_{sub} was 450 °C. Film thicknesses studied were 100 nm and 200 nm. As iron is also unstable in oxygen, it was necessary to consider the possibility of structural change in the substrate surface. To check this, annealed substrates, without a deposited film, was also prepared. Annealing temperature and oxygen pressure were the same as those used for VO_2 growth, i.e. 4.4 mTorr and 450 °C for an annealing time of 20000 s. AFM and XRD data of these four samples: a commercial substrate, an annealed substrate, and 100 nm and 200 nm VO_2 films are shown in Fig. 5.6 and

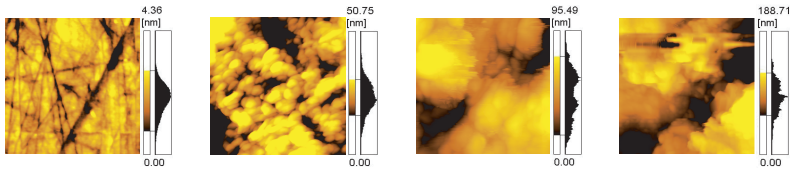

(a) (b) (c) (d)

Figure 5.6: AFM images (1×1 μm^2) of a Fe_3O_4 (111) substrate obtained from Surface Preparation Laboratory (a,b) and VO_2 thin films deposited on those substrates (c,d). (a) is the as-received surface and (b) is an annealed surface. the VO_2 film thickness was 100 nm in (c) and 200 nm in (d). For VO_2 films, the O_2 pressure was 4.4 mTorr, thickness: 100 or 200 nm, clamping: wire, T_{sub} = 450 °C.

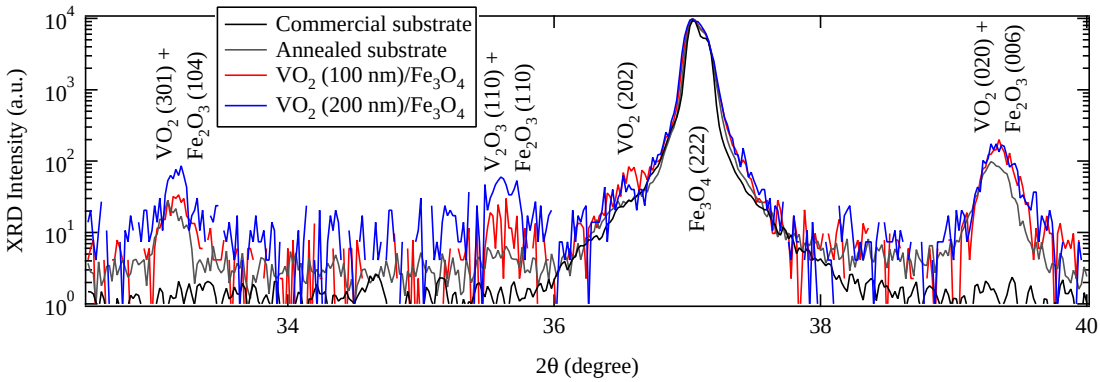

Figure 5.7: XRD data of a Fe_3O_4 (111) substrate and a VO_2 thin film deposited on a Fe_3O_4 substrate.

Fig. 5.7, respectively. Unfortunately, the substrate surface suffered from oxidation during annealing, changing the surface morphology. Despite this setback, it was possible to observe a VO_2 phase transition at around 340 K as shown in Fig. 5.8. In the XRD data of Fig. 5.7, some of the VO_2 peaks overlap with the hematite Fe_2O_3 phase that can be formed at the substrate surface during heating. Due to the low substrate surface quality, the texture in the film was not perfect. Instead, a polycrystalline film was obtained, with (020), (202), and (301) being seen in the XRD pattern.

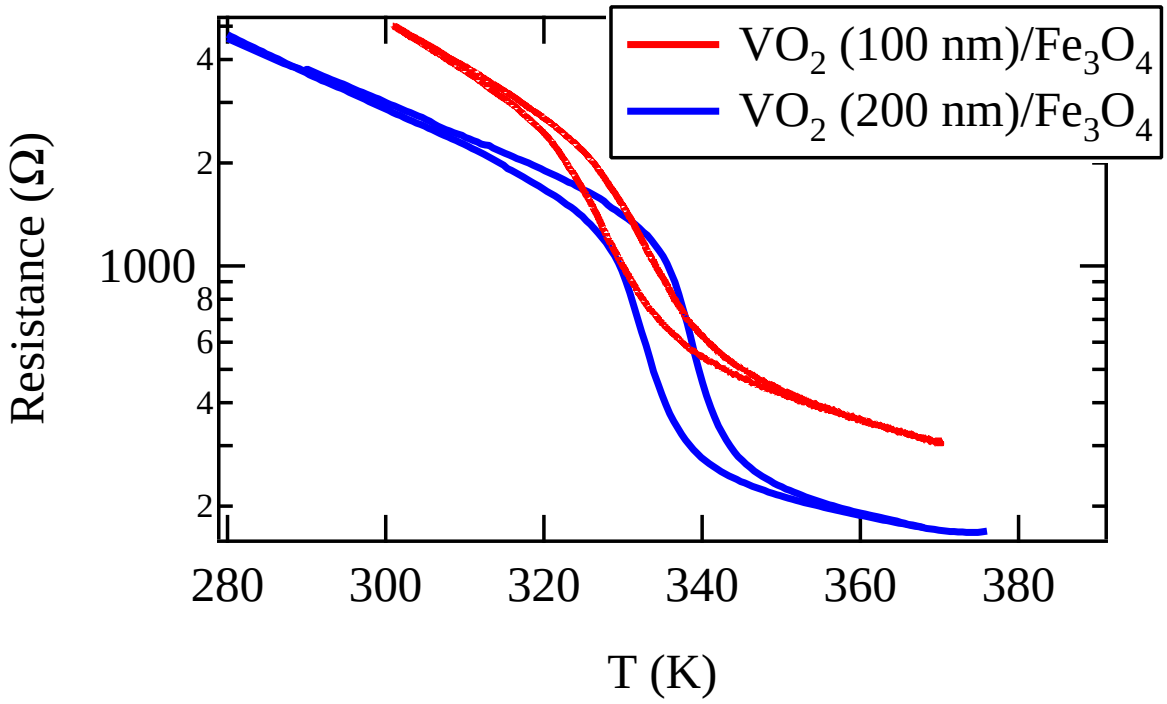

Figure 5.8: Resistance behavior of VO_2 films deposited on Fe_3O_4 (111). Films show a metal-insulator transition at around T_c of bulk VO_2.

5.4 Results and Discussions

5.4.1 Analysis of the results

Magnetostriction in Fe_3O_4 is not isotropic.[12] Due to this, strain in a VO_2 film grown on the Fe_3O_4 (111) surface varies with the direction of the magnetic field in the plane of the substrate surface. The direction of in-plane sample rotation is shown as the rotation direction (degrees) in Fig. 5.9. The reference azimuth (0 degree orientation) is defined as being normal to the $(01\bar{1})$ direction of the Fe_3O_4 substrate. The polar rotation angle of the permanent magnets is defined as the magnetic field rotation angle around the rotation axis, and the at zero point the magnetic field is normal to the substrate surface.

By using these definitions and literature data, it is possible to calculate the saturated longitudinal magnetostriction value and the corresponding VO_2 c-axis strain, δ_c as a function of the magnet rotation angle for every possible in-plane orientation of the rotation axis. The result is shown in Fig. 5.10. For further experiments, the rotation axis direction was set at 20 degrees, as that orientation was expected to give the largest strain contrast between different magnet rotation angles, as seen by the strong red and green regions in Fig. 5.10. However, a careful choice of the in-plane orientation of the sample is not particularly critical. As the simulations in Fig. 5.10(a-c) show, the functional shape of δ_c is always close to an absolute sine curve, $|\sin(\omega t)|$. However, the grain orientation texture in the film is important, as shown for simulations of three possible

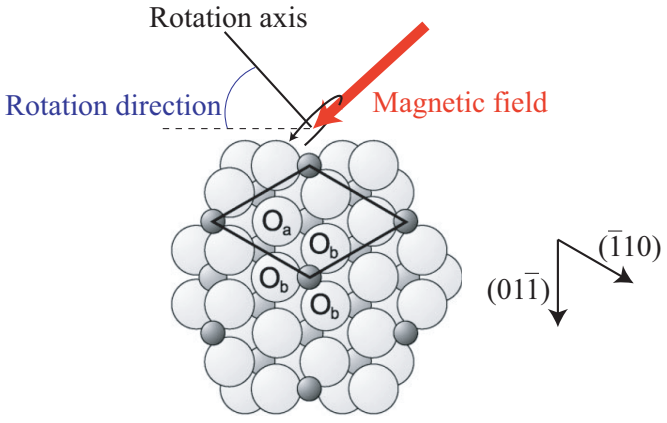

Figure 5.9: Fe_3O_4 (111) surface[13] and the definition of the azimuthal orientation of the magnet rotation axis. Magnetic field rotates around the sample in the magnet rotation stage.

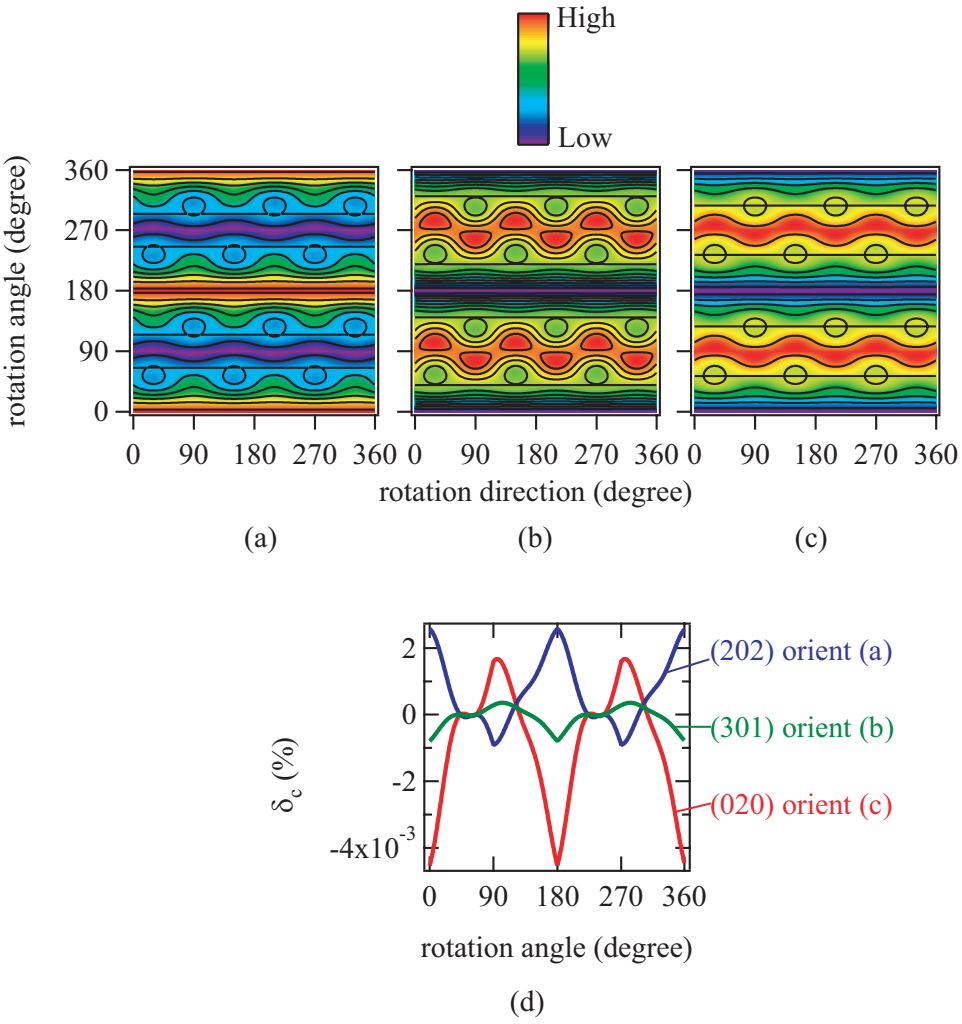

Figure 5.10: (a,b) Image plots expressing VO_2 *c*-axis strain (δ_c) vs. rotation angle and in-plane rotation axis orientation assuming that the VO_2 film is (202) oriented (a), (301) oriented (b), or (020) oriented (c) on a Fe_3O_4 (111) substrate. (d) Three lines extracted from rotation direction plots at an azimuth of 20 degrees in (a,b). δ_c was calculated from saturated longitudinal magnetostriction values.

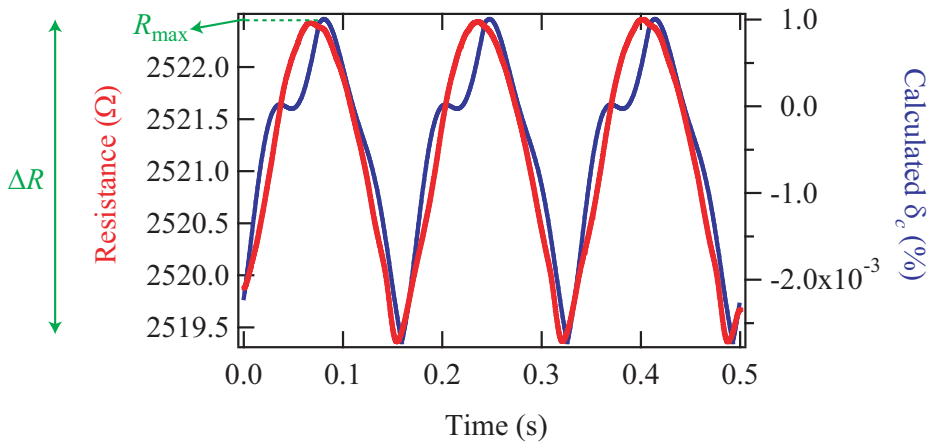

Figure 5.11: Raw oscilloscope data of the sample resistance and calculated δ_c at 3 Hz magnet rotation frequency assuming that VO_2 is (020) oriented.

film orientations shown in Fig. 5.10(d). If the VO_2 c-axis is normal to the substrate, the function becomes close to $-|\sin(\omega t)|$, and if VO_2 is polycrystalline, δ_c gets averaged out. Raw oscilloscope data of the sample resistance behavior followed $|\sin(\omega t)|$ as can be seen in Fig. 5.11, which indicates that VO_2 is not a random polycrystal film, but does have significant texture despite the degraded substrate surface layer. Combined with the XRD data, it can be assumed that VO_2 on Fe_3O_4 (111) substrate is either (202), (301) or (020) oriented. Previous studies have shown that the magnetostriction value in Fe_3O_4 is almost linear to the magnetic field until 0.4 T in all directions.[14] This fact shows that the δ_c function is the same as calculated ideally in the range of the magnet rotating stage. The blue line in Fig. 5.11 shows the calculated δ_c value assuming VO_2 is (020) oriented and that magnetostriction in the applied field (0.26 T in this case) is a linear function of the field. R_{max} is the maximum value of the resistance and ΔR is the peak-to-peak value of the resistance.

5.4.2 Quasi-static AC magnetic field in PPMS

For verifying the data obtained from the spinning magnet setup, measurements of a VO_2 film resistance response to a variable magnetic field was also measured in a PPMS. However, since the field strength in the PPMS requires changing the magnet current, it is only possible to vary the field under quasi-static conditions. Since the frequency is very small, temperature drift of the sample becomes a problem and a resistance drift

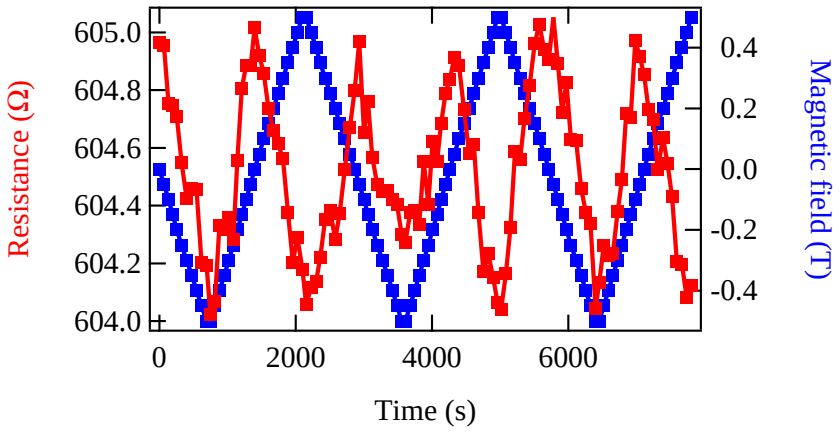

Figure 5.12: VO_2 film (200 nm) resistance change in a quasi-static alternating magnetic field measured in a PPMS.

due to slow temperature variation has to be subtracted from the data.

The measured resistance change in a variable magnetic field in a PPMS is shown in Fig. 5.12. The sample was a 200 nm-thick VO_2 thin film. Since magnetostriction, and thus the VO_2 strain is a function of $|B|$, where B is the magnetic field, the resistance response frequency should have mainly a 2ω component when B varies at a frequency ω. Experimental data successfully follows this expectation.

5.4.3 AC magnetic field in magnet rotating stage

VO_2 resistance response to an alternating magnetic field was measured with the magnet rotation stage at 3 Hz. The sample was a 100 nm thickness VO_2 film. An annealed substrate without a VO_2 film was also measured for reference.

Before measurement, it is necessary to determine the in-plane crystal direction of the substrate for measuring samples at a known in-plane azimuth. Pole figures in Fig. 5.13 were measured by 4-axis XRD for this purpose. The assumption in the measurement is that the X-ray incident vector (ϕ = 0) is parallel to Fe_3O_4 $(1\bar{1}0)$ at the starting point. Data indicate that $(1\bar{1}0)$ direction assumed at first was off from the real direction by 10 and 20 degrees in the VO_2 film sample and the reference crystal, respectively. Using this data, both samples were oriented along the 20 degree azimuth angle on the sample holder for the rotating field experiments.

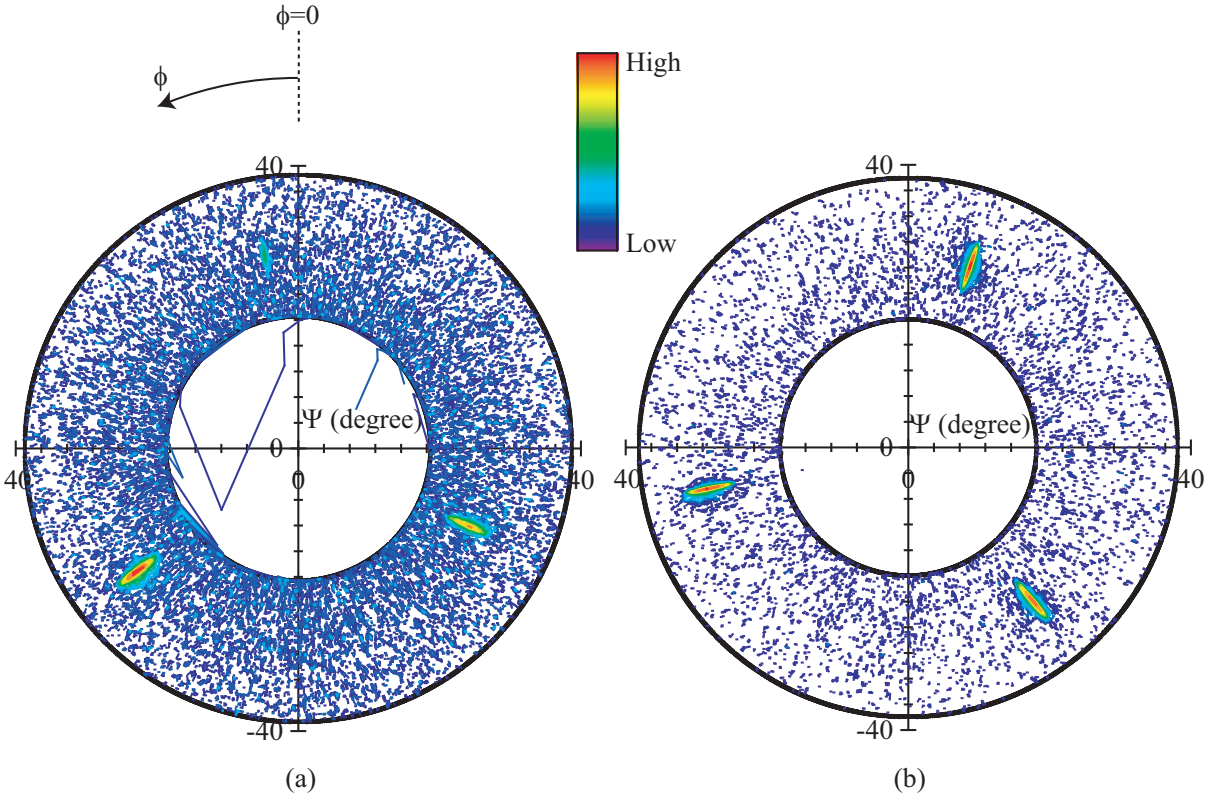

Figure 5.13: Pole figures of the Fe_3O_4 [311] diffraction peak, measured with a 4-axis XRD. (a) 100 nm VO_2 film and (b) commercial substrate. Measurement assumes that the *phi* = 0 direction is close to the Fe_3O_4 $(1\bar{1}0)$ crystal direction.

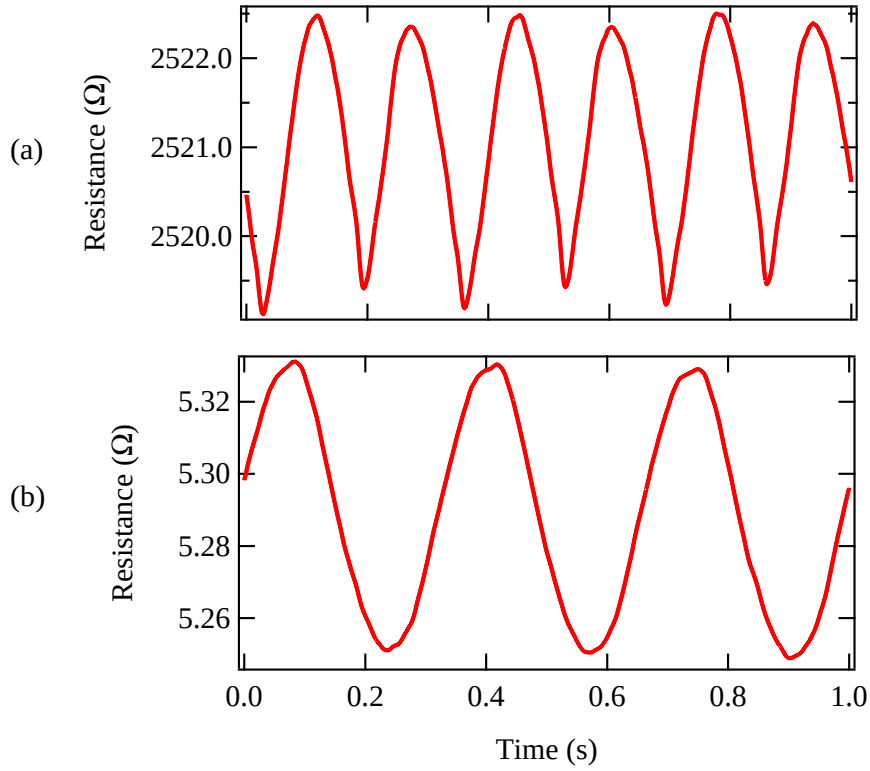

Figure 5.14: Resistance change at 3 Hz magnet rotation rate for a VO_2 film (100 nm) on Fe_3O_4 (111) substrate (a) and the response of an annealed substrate reference sample (b). Applied magnetic field strength was 0.26 T (6 mm distance between the two magnets).

Resistance changes in a 100 nm VO_2 film on Fe_3O_4 (111), measured at 3 Hz magnet rotation is shown in Fig. 5.14. For reference a measured response for a Fe_3O_4 substrate is also shown. From the point of view of magnetostriction, there is no difference between $\mathbf{B}$ and $-\mathbf{B}$, where $\mathbf{B}$ is the magnetic field vector. This indicates that VO_2 resistance change is expected to have only a 2ω component while parasitic electromagnetic induction in the sample holder wiring follows ω, where $\omega = 3$ Hz is the frequency of magnet rotation. As can be seen in Fig. 5.14, the resistance of a VO_2 thin film sample exhibits mainly a 2ω component with a very slight ω background. In contrast, the annealed substrate only shows a pure ω component. These data prove that the resistance change in the VO_2 thin film is actually caused by strain in VO_2 through a magnetostriction effect.

Temperature dependence of the resistance response was measured in Fig. 5.15. The

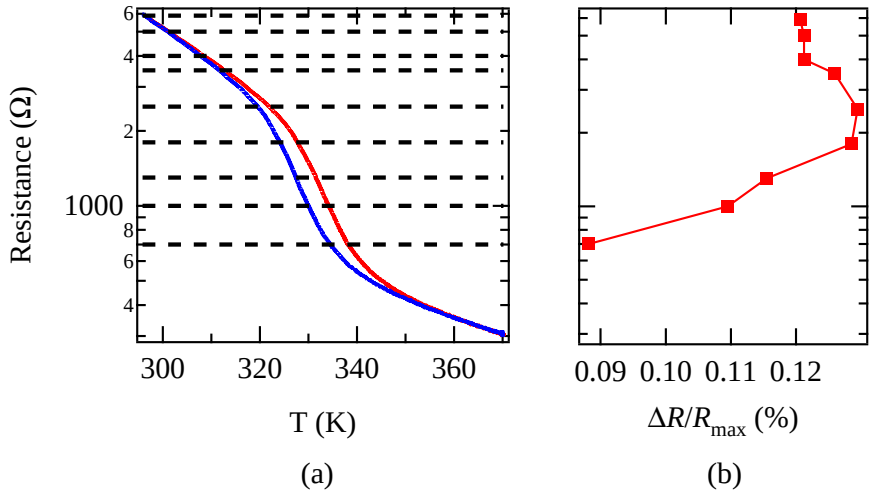

Figure 5.15: (a) Resistance vs. temperature data of a VO_2 thin film (100 nm). (b) Measured resistance dependence of the resistance change ratio, $\frac{\Delta R}{R_{\max}}$. Each resistance is shown in (a) as a dotted line.

resistance change ratio, $\frac{\Delta R}{R_{\max}}$ reached a maximum at 2.5 kΩ, which is close to transition point. This data is equivalent to the results obtained from experiments performed with the crystal bending stage (Fig. 4.31).

Magnetic field dependence of the resistance change ratio, $\frac{\Delta R}{R_{\max}}$ was also measured as in Fig. 5.16. Linear fitting is shown with a dotted line. This data indicates that $\frac{\Delta R}{R_{\max}}$ is almost linear to magnetic field. The VO_2 thin film deposited on Fe_3O_4 thus worked as a magnetic field sensor.

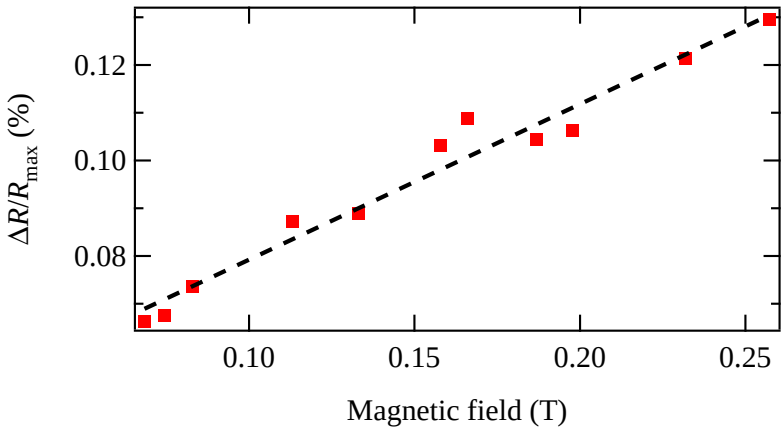

Figure 5.16: The resistance change ratio, $\frac{\Delta R}{R_{max}}$ as a function of the applied magnetic field. The magnetic field was controlled by changing the distance between two magnets.

5.5 Conclusion

A rotating magnetic field stage was constructed and used to measure the resistance response of a magnetic field sensor that is based on strain coupling between a strain-sensitive VO_2 thin film and a magnetostrictive Fe_3O_4 (111) substrate. The instrument worked as planned, and it was possible to observe a magnetic field induced phase transition due to strain coupling between the film and the substrate. The results obtained with spinning magnets were verified in quasi-static PPMS experiments and compared with strain data obtained from crystal bending experiments.

The VO_2 resistance change was at a maximum at around the VO_2 transition temperature, and reached a resistance modulation of 0.13 %. The response was linear to magnetic field within experimental errors, which shows that the VO_2 thin film deposited on Fe_3O_4 worked as a magnetic field sensor.

References

[1]S. Dong, J. Li, and D. Viehland, APL **83**, 2265 (2003).

[2]S. Dong, J. Li, and D. Viehland, APL **85**, 2307 (2004).

[3]S. Dong, J. Zhai, F. Bai, J. Li, and D. Viehland, APL **87**, 062502 (2005).

[4]J. Zhai, Z. Xing, S. Dong, J. Li, and D. Viehland, APL **88**, 062510 (2006).

[5]G. Srinivasan, E. T. Rasmussen, B. J. Levin, and R. Hayes, PRB **65**, 134402 (2002).

[6]K. Mori, and M. Wuttig, APL **81**, 100 (2002).

[7]C. Nan, G. Liu, and Y. Lin, APL **83**, 4366 (2003).

[8]H. Wiegelmann, A. A. Stepanov, I. M. Vitebsky, A. G. M. Jansen, and P. Wyder, PRB **49**, 10039 (1994).

[9]S. Di Matteo, and A. G. M. Jansen, PRB **66**, 100402(R) (2002).

[10]Ö. Özdemir, Geophys. J. Int. **141**, 351 (2000).

[11]http://www.irm.umn.edu/hg2m/hg2m_c/hg2m_c.html.

[12]L. R. Bickford, Jr., J. Pappis, and J. L. Stull, Physical Review **99**, 1210 (1955).

[13]M. Litter, and W. Weiss, Surface Science **432**, 81 (1999).

[14]C. W. Heaps, Physical Review **24**, 60 (1924).

Chapter 6

Studies of light-induced phase transition in VO_2 thin films

6.1 Scanning tunneling spectroscopy

This work was done in collaboration with Dr. Terada in Prof. Shigekawa laboratory at Tsukuba University. The aim was to observe a light-induced phase transition in VO_2 thin films by scanning tunneling spectroscopy (STS). For this purpose, VO_2 thin film samples were prepared.

As discussed in previous chapters, close to the transition temperature, the phase balance can be altered either by temperature or by strain. It was also pointed out in the introduction, that in addition to a structural phase transition, VO_2 also has a simultaneous Peierls-like electronic transition related to dimerization of V-V bonds. This electronic transition can be driven by rapidly changing the density of carriers in the material. One intriguing question is, if the structural phase transition can be induced by triggering an electronic transition by photocarrier injection.

STS is a measurement technique that extends scanning tunneling microscopy (STM). STM is most often used to measure real-space surface morphologies of conducting surfaces, The STM technique is based on the effect of quantum tunneling between an atom on a sharp tip and a surface. When the conducting tip is brought near the surface and a bias is applied between the tip and the sample, V_s (sample bias) can allow a tunneling current to flow. Because of this, STM can only be used to measure at least moderately conductive samples. The tunneling current I can be calculated as

$$I \propto \frac{V_s}{d} \exp\left(-\frac{4\pi}{h}\sqrt{2m\phi}d\right), \tag{6.1}$$

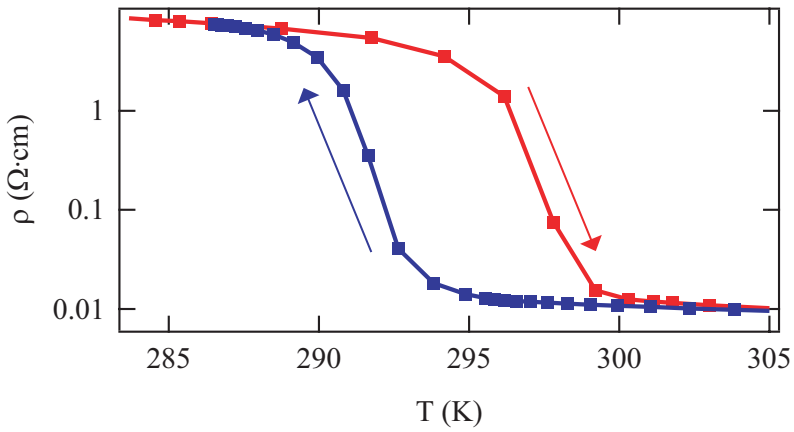

Figure 6.1: Resistance behavior of VO_2 thin film samples used for STS measurement. Deposition condition were O_2 pressure: 4.4 mTorr, thickness: 30 nm, T_{sub} = 450 °C, clamping: wire, substrate: TiO_2 (001) with 0.2 mm thickness and normal surface.

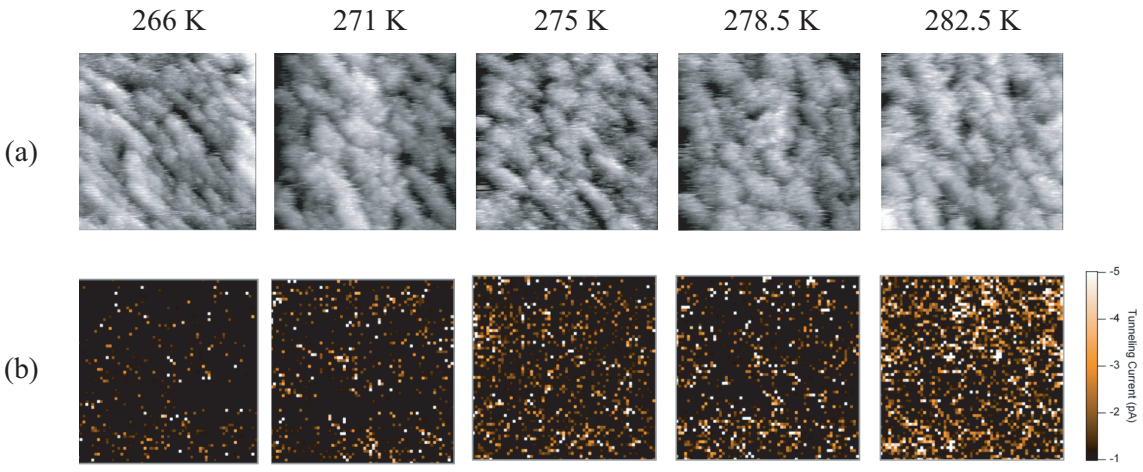

Figure 6.2: Topography measured by STM (a) and current maps measured by STS (b) of VO_2 surface (100×100 nm^2) at different temperatures. For STM (a), $V_s = -1.2$ V and $I = 0.1$ nA, and for STS (b), $V_s = -0.3$ V.

where h is Planck's constant, m is the mass of the electron, ϕ is the work function, and d is the distance between the tip and the sample. From Eq. 6.1, it is known that a 0.1 nm difference of d affects the tunneling current by an order of magnitude. This feature gives STM exceptional spatial and height resolution. It is also important to note that for electrons to transfer between the tip and the sample, a suitable energy level has to exist in the surface layer of the sample. When I is measured while V_s is being scanned, the tunneling probability changes according to the local density of states in the sample, assuming that the tip is a simple metal. However, this thesis shows only STS data at one V_s value, i.e. only tunneling current. This data is sufficient for distinguishing between conducting and insulating domains in a VO_2 film.

The VO_2 thin films used in these experiments were relatively thick at 30 nm. Most of the strain effect measurements were normally done with thinner films of about 10 nm thickness. All films were grown on TiO_2 (001) substrates and showed a clear metal-insulator transition. Since the film thickness was large, the grain structure is also different, leading to a relatively broad hysteresis curve, as shown in Fig. 6.1. As discussed in the introduction, the bulk hysteresis width is considerably narrower. Since the STM/STS measurements are local, it may be expected that the hysteresis behavior of a single domain or grain in the film would be similar to the behavior of a high-quality bulk crystal and show small hysteresis. Different grains, however, may switch at slightly different temperatures, perhaps reflecting a local grain-scale distribution of strain in the film. As shown in Fig. 6.2, the appearance of metallic domains upon heating was indeed observed. It is curious that the observed metallic domains appear to be laterally much smaller than the apparent surface grains shown in the corresponding topography images.

An attempt was made to detect a light-induced phase transition in the film near T_c, by measuring conducyivity maps before and after light illumination, as shown in Fig. 6.3(a). The sample was irradiated with 1.5 eV light, which can induce photocarriers in the film since the photon energy exceeds the bandgap of insulating VO_2 (0.7 eV). The light source was a femto-second laser (100 mW). As shown in Fig. 6.3, the volume of metallic domains in the film did indeed increase after light irradiation. However, the measurements have not progressed to measuring an actual time dependence. It is therefore not certain what the dynamics of the transition is. It is also hard to separate carrier injection effects from simple heating, since the metallic phase occurs above the transition temperature. It is known that the timescale of a purely electronic transition, as shown by THz absorption measurements, is a fs order process, while thermalization

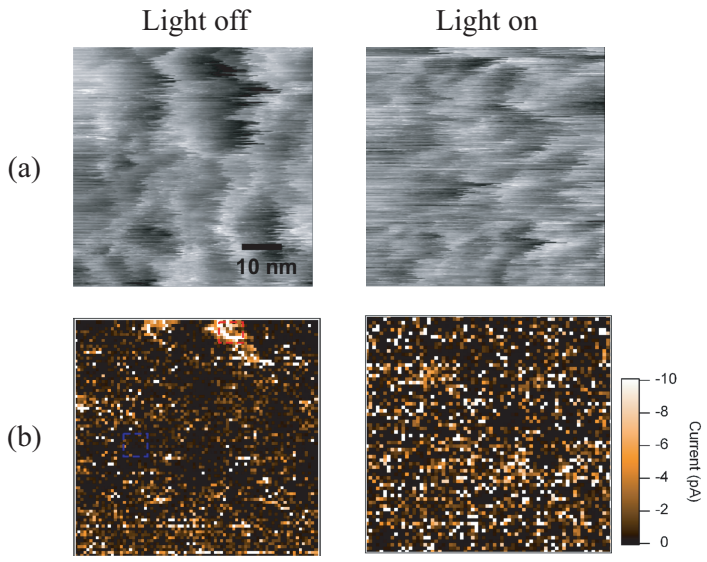

Figure 6.3: Topography measured by STM (a) and current maps measured by STS (b) for a VO_2 surface (60×60 nm^2) before light irradiation (left) and after (right). For STM (a), $V_s = -1.2$ V and $I = 0.1$ nA, and for STS (b), $V_s = -0.3$ V.

of the lattice is a μs order process. In order to observe a pure light-induced phase transition, the future plan is to measure the time dependence of current flow.

6.2 Photoemission spectroscopy

Another approach to measure light-induced effects in VO_2 is to use time-resolved photoemission spectroscopy (PES). This was done in collaboration with Mr. Yamamoto in Prof. Shin's laboratory at ISSP. The purpose was to observe a change in the photoemission spectrum of a VO_2 sample after the film was excited with a short light pulse. PES can observe the density of states below the Fermi energy, E_F. Monochromatic light with an energy of $h\nu$ (h is Planck's constant, and ν is light frequency) illuminates the sample. If sufficient energy is transferred to an electron in the solid and the electron is sufficiently close to the surface, the electron can escape from the surface. The kinetic energy of the electron, E_k, can be measured, and is given by

$$E_k = h\nu - E_B - \phi, \tag{6.2}$$

where E_B is the binding energy in the solid and ϕ is the work function of the surface. By analyzing E_k, the distribution of the electron density under E_F can be obtained.

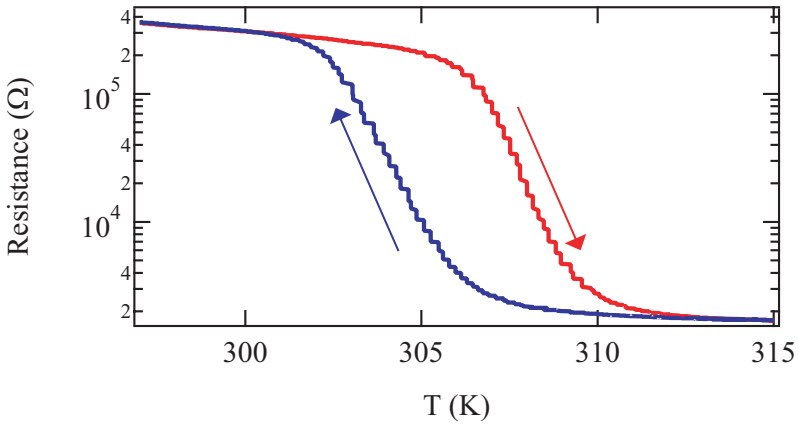

Figure 6.4: Resistance behavior of VO_2 thin film sample used for PES measurement. Deposition conditions were O_2 pressure: 4.4 mTorr, thickness: 10 nm, T_{sub} = 450 °C, clamping: wire, substrate: TiO_2 (001), 0.2 mm thickness and normal surface.

For a monochromatic probe light, high-energy (60 eV) light was used for observing the inner shell LDOS. Thanks to a pulsed nature of both the pump and probe light sources, it was possible to obtain a time-dependent density of states spectrum in a pump-probe measurement setup, where the time delay between the pump laser pulse and the photoemission probe laser were systematically varied.

The VO_2 thin film used in these measurements was 10 nm thick and grown on a TiO_2 (001) substrate. The resistance change at the phase transition point was observed as shown in Fig. 6.4. This film successfully showed an evolution of the coherent part at E_F with increasing temperature as shown in Fig. 6.5. This indicates that resistivity dropped at higher temperature, as expected based on the transport measurements.

Light-induced phase transition was measured in the VO_2 thin film near T_c by changing the time delay between the pump and probe pulses. The spectrum obtained in a configuration where the pump pulse was fired 100 ps after the probe probe pulse is shown in brown in Fig. 6.6. In this case, no photocarriers are expected to contribute to the density of states close to the Fermi level. After irradiating the film with a 3.1 eV (high enough to exceed the VO_2 band gap, 0.7 eV) laser, electron density near T_c slightly increased, as shown by the red line in Fig. 6.6. However, the resolution is close to the noise margin and the data therefore has to be treated as preliminary. The future plan is to measure a cleaner sample, and hopefully to obtain a better separation of the two spectra within the 0.5 eV binding energy range below the Fermi level.

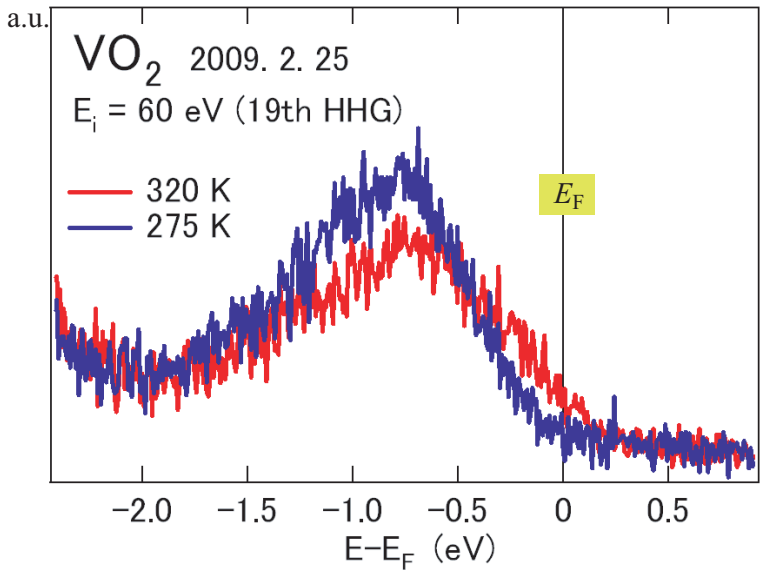

Figure 6.5: PES of VO_2 thin film samples measured at different temperatures across T_c. The high-temperature metallic phase shows an increase of electron density near E_F.

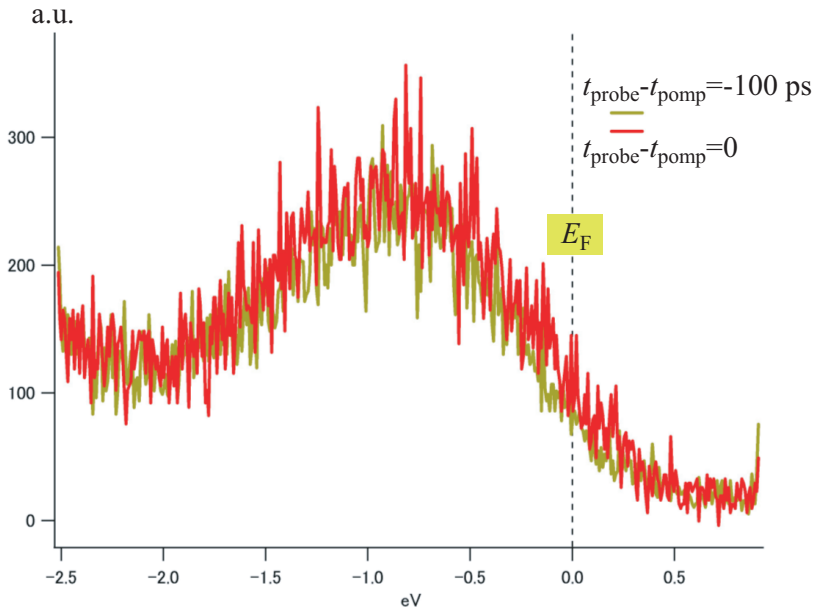

Figure 6.6: PES of VO_2 thin film sample before light irradiation (brown line) and after (red line). t_{probe} and t_{pump} are the irradiating time of probe laser and pump laser.

6.3 Soft x-ray interferometry

This work was done in collaboration with Mr. Terakawa in Prof. Suemoto's laboratory at ISSP. The aim was to observe the photo-induced domain growth process on nanometer scale in VO_2 thin films by soft x-ray interferometry. The experiment is done by generating carriers in the film locally with a high-speed laser pulse and measuring the time-dependent surface shape change by spatially-resolved x-ray interferometry For this purpose, VO_2 thin film samples were prepared.

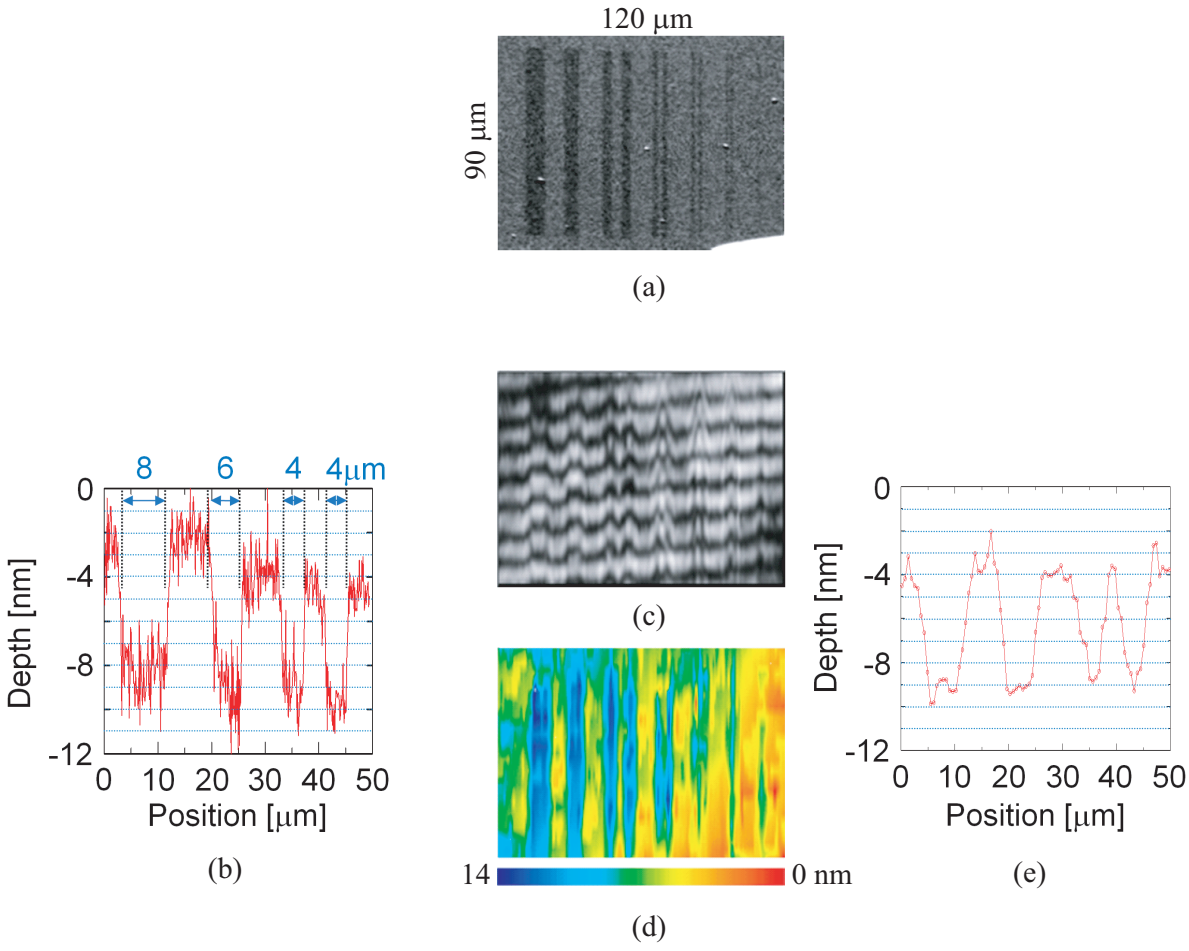

Figure 6.7: (a) SEM image of a Pt test pattern film manufactured by Focused Ion Beam. (b) Cross-section AFM image of the test pattern. Soft x-ray interferometry shows fringe shifts in an interferogram (c), and a reintegrated image (d). spatial resolution is obtained from a cross-section profile (e) of the test pattern.

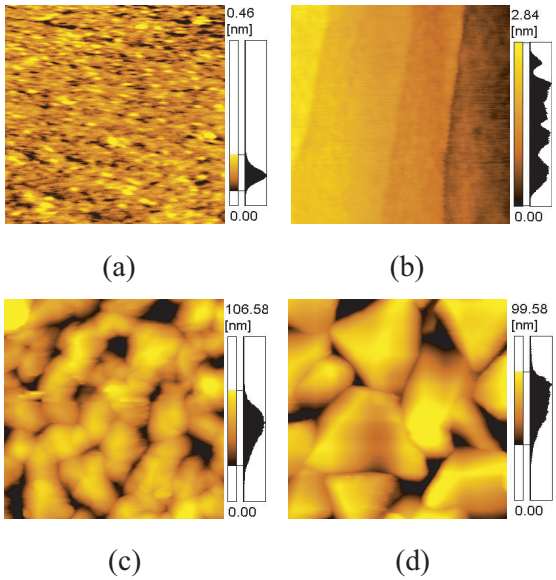

Figure 6.8: AFM images of a 0.5×0.5 μm^2 (a,b) and 1×1 μm^2 (c,d) area of a commercial Al_2O_3 (0001) substrate (a) and an annealed substrate (b). Surface of a 1400 nm-thick VO_2 film measured in the sample center (c), and edge (d).

This measurement method uses soft x-rays (13.9 nm, 89 eV, 7 ps) for high-resolution interferometry and a Ti:Sapphire laser (800 nm, 1.5 eV, 70 fs) as a pump light source. When soft x-rays reflect from an ideally flat surface incident to a double Lloyd's mirror with $\delta \sim 0.1$ mrad. between two mirrors, the beam pattern at an x-ray CCD camera shows interference fringes. However, if there is a bump on the sample surface, these fringes would shift, with the magnitude of the shift proportional to the difference of the optical path $d = \frac{2h}{\sin\theta}$, where h is height of the bump and θ is the grazing angle. The sample topography can be obtained by analyzing the local fringe shifts. For example, a shift distance by one fringe spacing corresponds to a 17.1 nm bump if the grazing angle is 24 degrees. A test pattern consisting of a Pt film, patterned by Focused Ion Beam was used for calibration (Fig. 6.7(a)). The test pattern consisted of a periodic array of bumps, as shown in a SEM image in Fig. 6.7(a). The bump heights were measured by AFM. An AFM cross-sections is shown in Fig. 6.7(b). A soft x-ray interferometry result is shown in (c) where fringe shifts corresponding to the Pt lines in the test pattern can be clearly seen. An integrated image (d), and a cross-section profile (e) correspond to the SEM and AFM data of the test pattern. The vertical and horizontal spacial resolutions derived from this measurement were 6 nm and 1.8 μm, respectively.

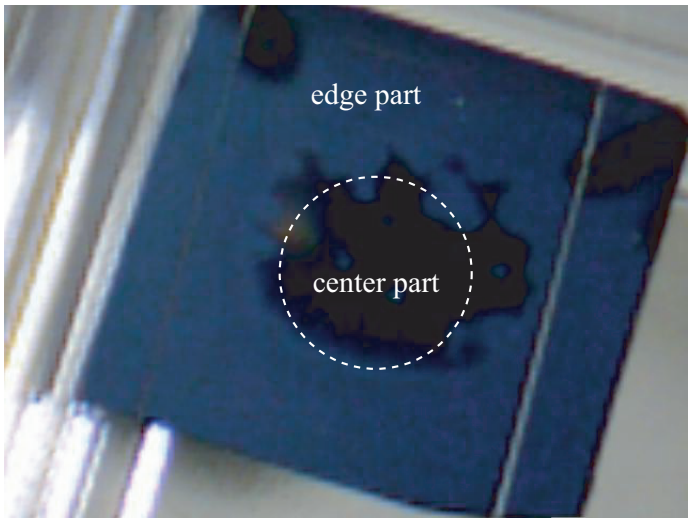

Figure 6.9: Optical camera image of a 1400 nm-thick VO_2 film deposited on an Al_2O_3 (0001) substrate. The center and edge parts are clearly different.

The reason why this method can be used to detect a light-induced phase transition in VO_2 is that a light-induced electronic phase phase transition will also cause a structural transition, which will result in a film thickness change in the photo-induced phase transition area. As for numeric details, VO_2 on Al_2O_3 is oriented in the (010) direction, which means that under perfect conditions, a lattice parameter change of 0.578 % would be expected.

As the surface of a commercial 0.4 mm-thick Al_2O_3 (0001) substrate is much more rough (Fig. 6.8(a)) than an annealed one (Fig. 6.8(b)), VO_2 thin films were deposited on annealed substrates. Annealing was done in air for 1 h at 1400 °C. For interferometry measurements with a 6 nm height resolution and a 0.578 % maximum height change, a very thick film was needed. Based on these considerations, a 1400 nm thick VO_2 thin film was fabricated by firing 350000 pulses at 1 Hz. The growth of the film thus lasted for about four days. The substrate was clamped with wires and held at 510 °C at an oxygen pressure of 4.5 mTorr while ablating. The deposition conditions were slightly different from the TiO_2 case. A photographic image of a thick VO_2 film is shown in Fig. 6.9. A color distribution can be seen in the film. The center part of the film looks black, while a gray region is visible on the edges.

AFM images and XRD data of the center part and the edge part are shown in Fig. 6.8(c,d) and Fig. 6.10. XRD shows epitaxial growth at the center part. VO_2 metal-to-insulator transition was also observed at the center part as shown in Fig. 6.11 (blue line).

For comparison, resistivity data for various other samples with different thicknesses but grown under similar growth conditions are also shown. Based on the diffraction and transport measurements, it should be possible to observe a light-induced phase transition in the center part of the film by soft x-ray interferometry. The largest problem is the surface roughness of the film, which is comparable to the expected surface shift. As can be seen in the AFM images in Fig. 6.8(c), the surface roughness is ~ 100 nm whereas the vertical resolution of the interferometry measurement is 6 nm. A large surface roughness would make the observed interference fringes weaker and any fringe shifts more difficult to observe. For flattening the surface after deposition, mechanical chemical polishing was attempted. The polishing work done by Maruto Instrument

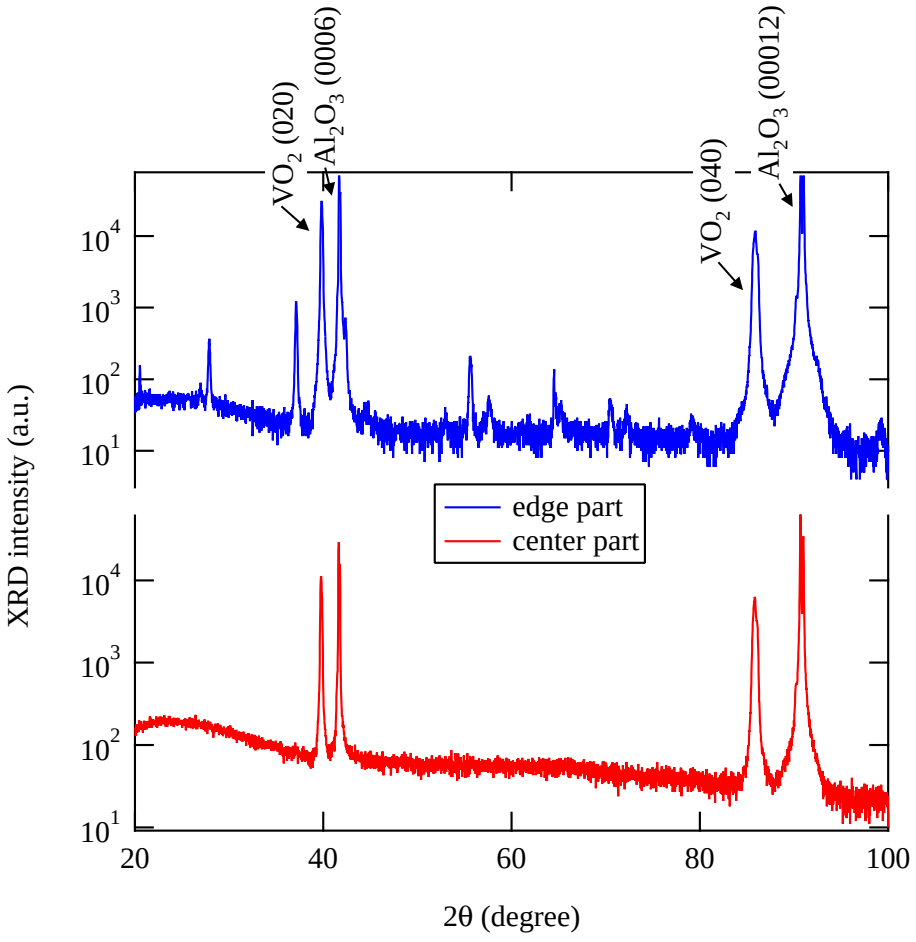

Figure 6.10: XRD data of a 1400 nm thick VO_2 film deposited on an Al_2O_3 (0001) substrate, measured at the edge part (blue) and the center part (red).

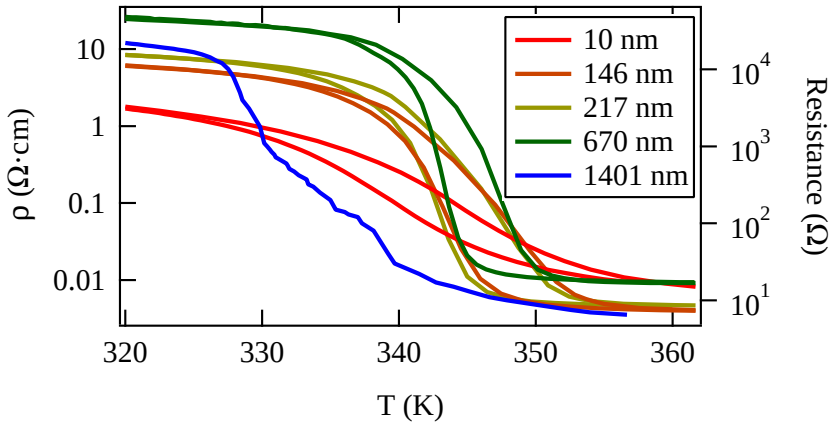

Figure 6.11: Metal-insulator transition measured in the center part of a 1400 nm thick VO_2 film (blue line, right axis) and comparison data for films with different thicknesses grown under the the same deposition conditions (left axis).

Co., Ltd. could reduce the VO_2 film surface roughness to < 5 nm while reducing the film thickness by $\sim$ 200 nm. Based on these numbers, the expected surface height change for a perfect phase transition would be $(1400 - 200)$ nm $\times$ 0.578 % = 6.9 nm, larger than the roughness value.

Interference fringes of a thinner test VO_2 film were observed as shown in Fig. 6.12(a). This data shows that the reflectivity from the VO_2 surface at a grazing angle of 20° is sufficient for this measurement. A polished VO_2 film was also observed, as shown in Fig. 6.12(b). The grazing angle was 17.2°. It is clear that the interference fringes of this film are not as straight as for the thinner film. It would thus be difficult to see the fringes shift under a pump pulse.

Time-resolved pump-probe measurement have so far not succeeded in observing a light-induced phase transition. This is partly due to local roughness in the film, which makes it difficult to determine the exact point where the pump beam hits the sample surface and the exact shift of the fringes that would be expected to occur during a photo-induced phase transition.

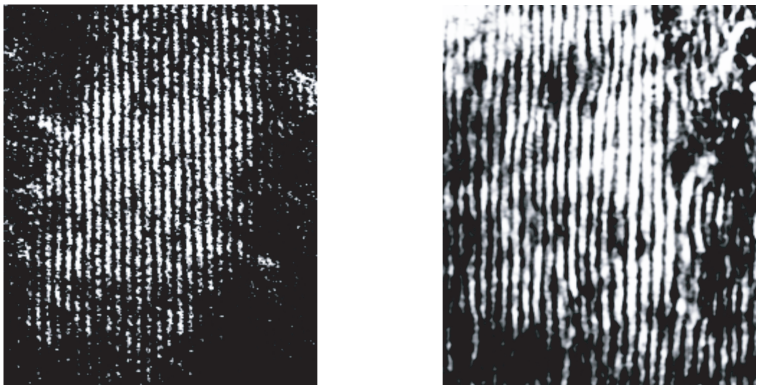

(a) (b)

Figure 6.12: Interference fringes of a test film with a thickness of 200 nm and a surface roughness of < 2 nm (a), and a polished film with a thickness of 1200 nm and a surface roughness of < 5 nm (b).

Chapter 7

Conclusion

In this study, a high-frequency bending stage and a magnetic field rotation stage were constructed and successfully used for observing properties of strained oxide films and studying strain relaxation and strain-driven phase transitions. The bending stage was used for observing VO_2 phase transitions induced by dynamic strain itself while the field rotator was used for observing strain coupling between a VO_2 film and magnetostrictive substrate (Fe_3O_4) in a time-dependent magnetic field. The purpose was to observe a purely structural effect on a phase transition while that of the collaborators was to observe purely electronic excitation effects on the same phase transition. The interesting points are, for example, the difference of time constants, phase transition mechanisms, etc. However, detecting the the light-induced excited states is experimentaly extremely challenging and have so far not been observed in the films grown in this work.

A dynamic-strain-induced phase transition in VO_2 thin films was measured and successfully observed with the high-frequency bending stage. Amplification from strain to resistance, A_0 was measured as 157 while it is 4 with usual metal strain gauges. The value A_0 shows it is related to temperature-induced phase transition behavior. The activation energy, $k\Delta T_{\mathrm{hys}}$ for the dynamic-strain-induced metal-to-insulator transition was measured, giving $k = 0.030$ eV/K. Close to T_c, the effect of strain on resistance is larger than a pure thermal change by a factor of nearly 2 ($C_1 = 1.9$). The data includes two time constants, corresponding to a domain nucleation process ($\tau_1 \sim 10^{-5}$ s) and a domain growth process ($\tau_2 \sim 10^{-3}$ s). It was found that τ_1 is increasing with temperature because the energy barrier height separating two phases becomes larger while τ_2 is constant and is mainly given by thermal energy.

Resistance change caused by a magnetic field in a VO_2-based magnetoelastic field

sensor was observed. The function of the field sensor relies on strain coupling between a strain-sensitive VO_2 thin film and a magnetostrictive Fe_3O_4 (111) substrate. The operation was validated in a PPMS and characterized in a rotating magnetic field device. The VO_2 resistance change reached a resistance modulation of 0.13 %, and it was confirmed that the sensor worked as planned.

In both cases, dynamic-strain-induced VO_2 phase transition was observed, either by applying dynamic strain directly or by strain coupling. In both cases, the most sensitive point for VO_2 resistance change was at around the phase transition point. That is the expected behavior for a phase transition material like VO_2. It indicates that dynamic strain can be thought to be just another external excitation, like light, magnetic field, electric field, etc.

Several issues also remain. For a combined magnetic field sensor, deposition conditions and sensor structure still needs to be optimized. The VO_2/Fe_3O_4 films fabricated in this study could not detect pico-Tesla fields. Next, strain-induced phase transition in other materials is also interesting, and can probably be measured with the high-frequency bending stage. For example, T_c change in superconductivity, ferromagnetic or ferroelectric transitions, etc. are all sensitive to lattice strain. These are mostly discussed in terms of epitaxial strain. Epitaxial strain experiments, however, take a long time to perform, have lots of ambiguity due to microstructure changes and limited by the available film/substrate material combinations. The bending stage developed in this work gives an anisotropic strain effect in the film (tensile in one direction and fixed in the other). This feature can be useful for probing (dynamic-)strain effects in a material that has in-plane anisotropy such as charge-ordered states or stripe states in transition metal oxide materials. Moreover, the merit of this stage is that it is in some cases possible to reach higher pressures than with a diamond anvil cell by choosing a suitable film and a flexible substrate. This measurement can possibly be used to observe new high-pressure physics or to do an accelerated test of strain effect on oxide electronic devices. The stage is now operating in air, which limits the possible temperature range to $\sim 270 - 350$ K. For the purpose of extending the applicability of the crystal bending technique to materials other than VO_2, the stage should be placed in vacuum and combined with a liquid He cooling system, such as a cryocooler, dipping stage or perhaps the PPMS. Finally, I hope that with the help of collaborating groups, it will be possible to observe a light-induced phase transition in VO_2 thin films.

Acknowledgments

This work was done at the Institute for Solid State Physics of University of Tokyo from April 2008 to January 2010. This work was supported by NEDO project 07E51002a.

I have many people to thank for helping to make my experience enriching. I would like to express my gratitude to them here.

First, I would like to express my profound gratitude to Professor Mikk Lippmaa for helpful advice. I was taught from him not only the basic knowledge for oxide thin films, but also how to construct new instruments, carry forward great experiments, use computer skills, write a paper and a thesis, and so on. I would like also to express my gratitude for his spending much time and passion for developing my ability.

I would like to express my great gratitude to Dr. Tsuyoshi Ohnishi for helping to use many instruments, PLD especially. PLD he constructed have worked greatly and he advised me to use it successfully.

I would like to express my great gratitude to Dr. Ryota Takahashi for giving useful advice for experiments, and for writing a Japanese paper. His accurate advice for Japanese sentence greatly helped me to let people understand what I wanted to say.

I thank Dr. Mikko Matvejeff for giving many experimental advice, which were very helpful. Moreover, Talking with him helped me to grow my English ability.

Mr. Kazunori Nishio not only gave me advice for many experiments, but also advised me for living a comfortable laboratory life. Ms. Reina Ohtsuka and I encouraged each other and discussed many things, which made me have limitless motivation in laboratory.

I thank Professor Tetsuo Tuchiya, Dr. Tomohiko Nakajima, and Ms. Masami Nishikawa for providing the VO_2 thin films deposited by ELAMOD. This extra film other than PLD let us understand strain properties of various VO_2 films.

I thank Professor Zenji Hiroi and Dr. Yoshihiko Okamoto for providing the V_2O_3 target and giving the materials for free.

I would like to show my gratitude to Professor Yukio Hasegawa, Dr. Toyoaki Eguchi, and Dr. Masayuki Hamada for letting me to use AFM and valuable advice. I would like to express my gratitude to Hidenori Takagi laboratory members for letting us to use conductive AFM tips. Moreover, I am sorry for breaking three tips though it is expensive.

I would like to express my gratitude to Professor Yuji Matsumoto and Professor Ichiro Takeuchi, who were NEDO project members. Professor Yuji Matsumoto gave me great advice for fabricating flat TiO_2 surface. Professor Ichiro Takeuchi also gave me great advice for fabricating a composite magnetic field sensor.

I would like to express my gratitude to Dr. Seiji Muranuki in the workshop and for helping to make great instruments and giving kind advice though I asked questions over and over again.

I would like to thank to secretaries Junko Kawamura, Yukiko Hanada, Yukiko Tan, and Makiko Matsuzaki for office work and giving beautiful smile. That was priceless encouragement for me.

Finally, I would like to express my gratitude to my family for their endless supports in life.